

Heterogeneous catalysts for CO₂ hydrogenation to formic acid/formate: from nanoscale to single atom

Ruiyan Sun,^a Yuhe Liao,^{a,c} Shao-Tao Bai,^a Mingyuan Zheng,^b Cheng Zhou,^a Tao Zhang,^{*b} and Bert F. Sels^{*a}

^aCentre for Sustainable Catalysis and Engineering, Faculty of Bioscience Engineering, KU Leuven, Celestijnenlaan 200f, 3001, Heverlee, Belgium. E-mail: bert.sels@kuleuven.be

^bState Key Laboratory of Catalysis, Dalian Institute of Chemical Physics, Chinese Academy of Sciences, Dalian 116023, China. E-mail: taozhang@dicp.ac.cn

^cGuangzhou Institute of Energy Conversion, Chinese Academy of Sciences, Guangzhou 510640, China.

Abstract

Propelled by the vision of carbon-neutral energy systems, heterogeneous hydrogenation of CO₂ to formic acid/formate, a liquid hydrogen carrier, has been intensively studied as a promising approach to realize renewable and decarbonized energy supply. In the present review, the state-of-the-art of heterogeneous catalysts for this process is comprehensively summarized. First, a brief description of the challenges associated with thermodynamics is provided. Major advancements on constructing efficient heterogeneous catalysts then constitute the main body of this review, mainly involving nanostructured and single atom catalysts based on noble metals. Special attention is paid to the relevant structure-activity correlations and mechanistic insights, which provide strong bases for rational catalyst design. Key factors related to catalytic activity are highlighted including metal dispersion, electron density, basic functionalities, and concerted catalysis of metal and basic sites. A summary and outlook is presented in the end. We believe that this review will inspire more novel research from the catalysis community to advance the design of innovative catalytic materials towards the ultimate sustainable energy sector with a closed carbon loop.

Broader context

Devising new technologies to drive the evolution from current CO₂-emission-intensive energy modes to renewable energy landscapes featuring a circular carbon economy is the major challenge facing the sustainable development of human society. Under this background, the utilization of captured CO₂ as a renewable carbon feedstock for the manufacture of chemicals and fuels is receiving considerable attention. Formic acid, which can be readily synthesized from CO₂ and H₂, offers a potential solution to address this energy transition challenge due to its role as a carbon-neutral energy carrier to store renewable energy in the form of H₂. Central to the CO₂-involved H₂ storage system lies in the development of efficient and durable heterogeneous catalysts. Accordingly, the catalytic conversion of CO₂ to formic acid has been intensively explored in the realm of heterogeneous catalysis. In particular, benefiting from the new frontier of single atom catalysis, the scope of heterogeneous catalyst candidates has been further broadened in recent years. This review presents a critical overview of the design of heterogeneous metal catalysts for CO₂ reduction to formic acid/formate from traditional nanoscale to novel single atom scale. Diverse single-atom engineering and nanostructuring strategies have been exploited to unlock high-performance catalysts by regulating the size, electronic properties, and coordination environments of active metal species. We also point out the remaining challenges in the pursuit of practically viable CO₂-based H₂ storage process, that is, deepening the knowledge of structure-property-activity relationships to enable the precise construction of active sites with superior activity and stability.

1. Introduction

In nature, the release and capture of carbon dioxide (CO₂) is subtly regulated via the natural processes of photosynthesis and respiration, which have contributed to a stable atmospheric level of CO₂ at around 250 ppm over thousands of years.¹ Nevertheless, since the industrial revolution, the steady status has been disturbed by the increasing emissions of anthropogenic CO₂ from the continuous exploitation of fossil resources. This has led to a remarkable rise in CO₂ levels up to approximately 415 ppm nowadays.² The associated consequences such as global warming, sea-level rise, and extreme climate have aroused substantial awareness of taking effective measures to mitigate excessive CO₂ emissions.

Aiming to achieve a “decarbonized” energy sector, renewable energy sources such as biomass, wind, geothermal, and solar energies are being increasingly applied to substitute and/or supplement fossil fuels across the world. However, considering the limited share of renewables in global energy consumption, e.g. amounting to around 11 % in 2018,³ the International Energy Agency projects that massive amounts of CO₂ up to 35 billion metric tons will be released into the atmosphere globally in 2020.⁴ The emitted and accumulated CO₂ over time in the atmosphere is far beyond the buffer capacities of natural CO₂ recycle. In this regard, carbon capture and utilization (CCU) appear an effective technical solution to address the overloaded CO₂ in air.⁵⁻⁷ Central to the CCU process is the catalytic upgrading (i.e., utilization) of CO₂ to value-added chemicals and fuels,⁸ mimicking the natural fixation of CO₂ into fossil resources. Specifically, the utilization of CO₂ as a carbon source together with the renewable H₂ from water splitting provides a potential pathway to integrate renewable energy into the established chemical value chain (Figure 1).^{9,10} Various synthetic approaches have been developed to convert CO₂ into a broad range of chemicals including polycarbonate, formic acid/formate, methanol, methane, and hydrocarbons, etc. at laboratory or industry scale.¹¹⁻¹⁶ Among them, formic acid/formate, a versatile C1 molecule, has received a surge of renewed attentions during the last decade, due to its emerging role as a green energy carrier for a sustainable future.^{17, 18} The high density of formic acid (1.22 g/mL) endows it with a considerable volumetric H₂ capacity of 53 g H₂/L, thus exhibiting large potential as a liquid H₂ carrier,¹⁹ in particular for hydrogen fuel cell vehicles. In addition, formate/formic acid is considered as a crucial intermediate for the synthesis of valuable oxygen-containing compounds (e.g., alcohols, esters, acids) in the field of syngas catalysis.^{20, 21} In particular for the synthesis of higher alcohols, the adsorbed CO is proposed to combine with the hydroxyl groups on catalyst surface giving rise to formate species as the precursor to alcohols.²² As depicted in Figure 1, an attractive carbon-neutral energy scenario can be envisioned based on the reversible conversion of CO₂ to formic acid. Analogous to CO₂ reduction to formic acid, the dehydrogenation of formic acid can be facilitated by using the similar or even same catalytically active sites,²³⁻²⁸ further improving the economic feasibility of this carbon-neutral energy system. Nevertheless, life-cycle assessment (LCA) studies have disclosed that the energy demands for CO₂ supply, H₂ production, and hydrogenation can cause positive or even higher global warming impacts for CO₂ reduction to FA in certain scenarios,²⁹⁻³¹ in comparison to the fossil-based FA production. Therefore, a realistic carbon-neutral energy system also necessitates CO₂ supply, H₂ production, and (de)hydrogenation preferentially powered by renewable energy (e.g., wind, solar) with minimized carbon footprints. Even though only limited environmental benefits can be achieved currently, CO₂ hydrogenation to FA as a sustainable and feasible H₂ storage system is of significant importance in the context of circular H₂ economy.³² Furthermore, catalytic reduction of CO₂ to formic acid/formate involves the formation of C–H bond by

breaking a C=O bond, providing a good model reaction to investigate the initial activation steps of CO₂ by H₂.

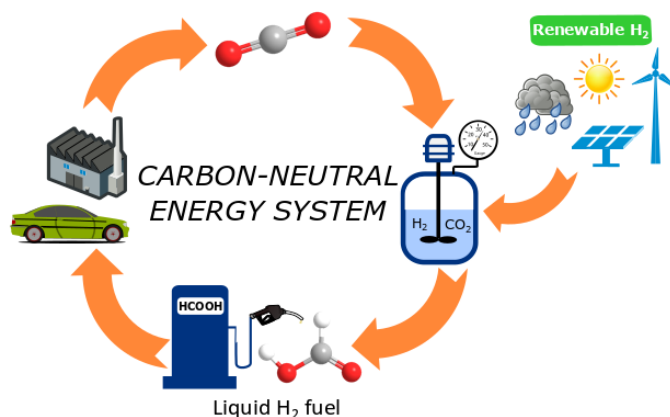


Figure 1. Schematic illustration of the prospective carbon-neutral energy scenario based on formic acid.

Unfortunately, CO₂ is known as a kinetically and thermodynamically stable molecule, as indicated by a high bond energy of 806 kJ/mol. This leads to a grand challenge encountered in CO₂ valorization, namely, intrinsically low-reactivity of CO₂ toward chemical transformations. Catalysis plays a crucial role in overcoming the high kinetic barriers to enable efficient reduction of CO₂ to formic acid/formate. Intensive research has resulted in considerable success in catalyst developments, both homogeneous and heterogeneous catalysts.³³⁻³⁶ A multitude of molecular metal complexes, comprising various metal centers and ligands with well-defined structures, have demonstrated outstanding activities for the homogeneous CO₂ reduction to formic acid/formate,^{26, 33, 37-39} exemplified by a Ru-PNP pincer complex showing a record turnover frequency (TOF) of up to 1100000 h⁻¹.⁴⁰ Nozaki and coworkers reported another highly active molecular Ir-PNP pincer complex with a turnover number (TON) as high as 3500000.⁴¹ The pyridine moiety of the Ir-PNP pincer complex was proposed to facilitate the key steps of H₂ activation and proton/hydride transfer over Ir centers via a dearomatization-aromatization mechanism.⁴² In spite of such unparalleled performance, the problematic separation and recycling of metal complexes as well as the adopted expensive and air-sensitive ligands pose huge hurdles for the practical application of molecular complexes. The easy-handling and recyclability of heterogeneous catalysts, especially advantageous to continuous operation in practice, have motivated extensive research efforts to realize the catalytic synthesis of formic acid/formate heterogeneously. A series of classical supported-metal catalysts containing nanoparticles and sub-nanometric clusters have been reported as efficient heterogeneous catalysts for formic acid/formate production.^{35, 43, 44} Nevertheless, heterogeneous catalysts usually exhibit inferior catalytic performance to their homogeneous counterparts due to the poor atom utilization efficiency. For a typical nanocatalyst, a large fraction of active sites are embed in a bulk phase, therefore unable to contribute to the catalytic performance directly. Distinct from the uniform coordination structure in homogeneous systems, heterogeneous catalysis is characterized by its heterogeneity of nanostructured active sites in terms of size, shape, and local microenvironment interacting with the active sites.^{45, 46} These diverse active sites would lead to a reduced activity/selectivity toward formic acid/formate along with the formation of side products, e.g. the competing reduction of CO₂ to CH₄ and CO. Therefore, there exists long-standing

pursuit of an “idealized catalyst” bearing the advantages of both homogeneous catalyst (high activity/selectivity) and heterogeneous catalyst (easy separation). In this context, a new concept of heterogeneous catalyst was recently proposed: single-atom catalysts (SACs) with atomically dispersed metal atoms on solid matrixes feature maximum atom utilization, relatively uniform structure, and unique electronic configurations.⁴⁷⁻⁴⁹ Downsizing nanostructured active sites to single atom not only makes all active atoms accessible to reactants and also reduces the cost of metal component. These characters make SACs seemingly very promising to serve as the “idealized catalyst” to efficiently catalyze heterogeneous CO₂ reduction to formic acid/formate. Exploring and developing SACs for efficient CO₂ upgrading have become one of the most active fields in heterogeneous catalysis. Recently, a number of studies have showed the excellent activity and good recyclability of SACs in CO₂-related catalytic conversions,⁵⁰⁻⁵⁴ in particular for CO₂ hydrogenation to formic acid/formate. In addition to the well-developed thermochemical CO₂ reduction, electro- and photocatalytic CO₂ reduction represent another two promising approaches to synthesize formic acid, which are currently active topics of intensive research. The latter two technologies are more sustainable with less environmental footprints than thermocatalytic CO₂ reduction, since they are driven by clean and renewable energy without extra energy input and H₂ demand. However, both of them are still in early-stage research with very low technology readiness levels. The high cost of renewable electricity, low current density, poor conversion efficiency and productivity are the major bottlenecks hindering the large scale implementation of electro- and photocatalytic CO₂ reduction to formic acid. The reader may refer to recent review articles for more details of electro- and photocatalytic approaches,⁵⁵⁻⁶² which are beyond the scope of the present Review.

Heterogeneous CO₂ reduction to formic acid/formate has been comprehensively summarized in several reviews from different perspectives,^{35, 44, 63-66} covering aspects of catalytic materials, reaction parameters, process engineering, and mechanistic insights. In recent years, the rapid development of single atom catalysis has given rise to an increasing number of SACs featuring high activity for CO₂ reduction to formic acid/formate. Accordingly, it is of great significance to discuss and summarize the recent advances of heterogeneous catalysts from traditional nanoscale to novel single atom. In this review, we will concentrate on the latest achievements on two main classes of heterogeneous catalysts, i.e., nanostructured metal catalysts and SACs for CO₂/bicarbonate hydrogenation to formic acid/formate (Figure 2). The discussion part will focus on the catalytic performance of various nanoparticles and single atoms with an attempt to extract the basic structure-activity relationships associated with geometric and electronic effects. The comparison of SACs and nanocatalysts and the activation of H₂/CO₂ over different catalysts are also discussed. These fundamentals are expected to shed light on tailoring new generation heterogeneous catalytic materials for CO₂ conversion with high efficiency and stability.

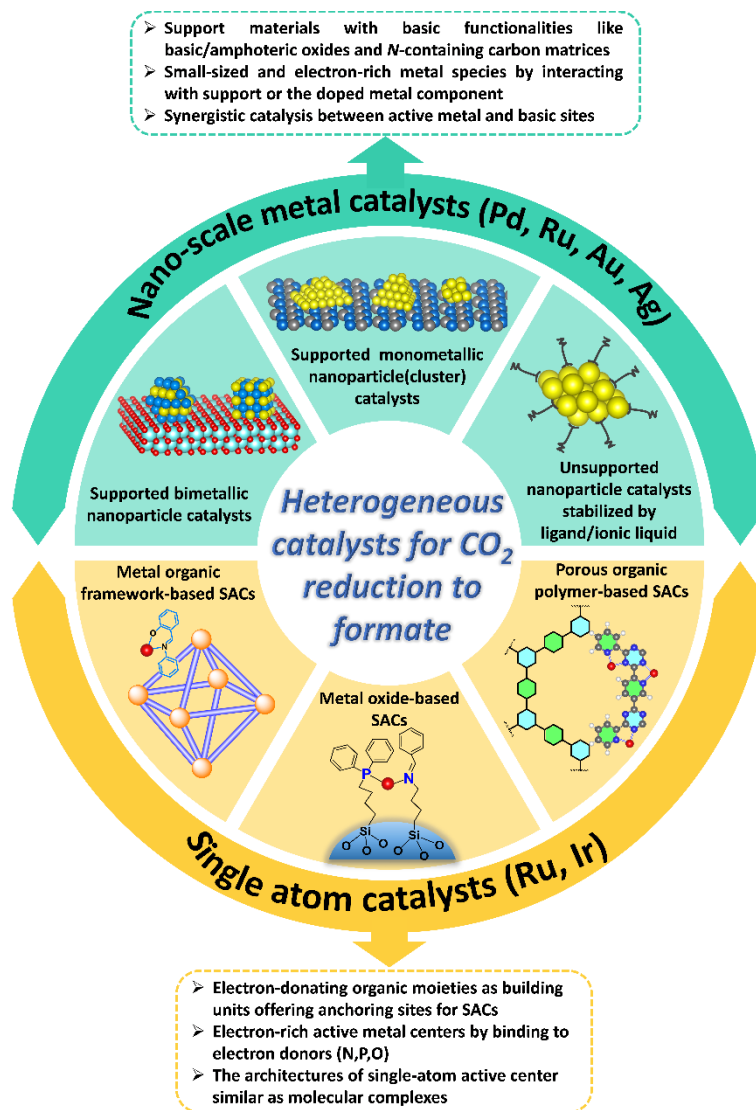


Figure 2. Overview of the heterogeneous catalysts developed for CO₂ reduction to formic acid/formate and the typical features of SACs and nanoscale metal catalysts.

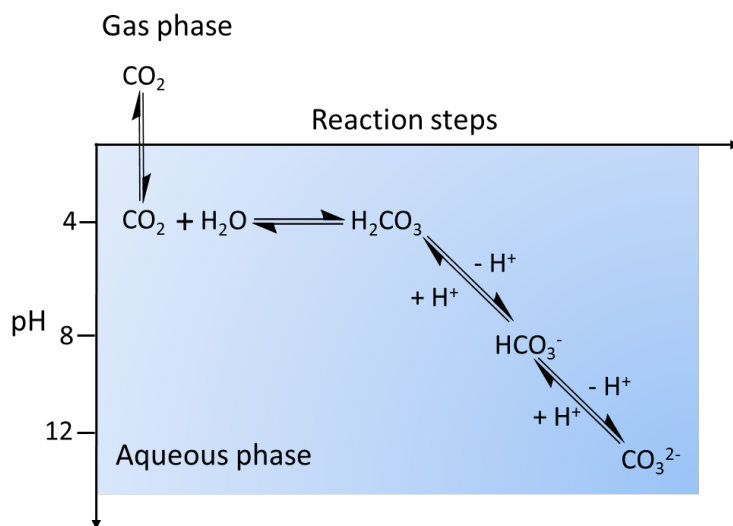
2. Thermodynamic aspects

The major challenge associated with the catalytic production of formic acid from CO₂ lies in the unfavorable thermodynamics (equation 1, Table 1),⁶⁷ originating from the unfavorable entropic contribution of transforming gaseous substrates (CO₂ and H₂) into liquid product (formic acid). Two strategies have been commonly exploited to mitigate the thermodynamic limitation: the addition of base additives (i.e., amines, hydroxides and (bi)carbonates), and choosing an appropriate reaction medium (i.e., water, alcohols, DMSO, ionic liquids). For example, if CO₂ hydrogenation is conducted in aqueous solution, the formation of formic acid becomes thermodynamically favored with a negative Gibbs energy (equation 2, $\Delta_r G^{\ominus}_{298\text{K}} = -4$ kJ/mol, Table 1) thanks to solvation effects, which can reduce the entropy difference between CO₂/H₂ and formic acid.⁶⁸ Apart from solvation effects, the utilization of alcoholic

solvent offers another benefit by esterification with formic acid to form alkyl formate (equation 3, Table 1), thereby shifting the reaction equilibrium toward alkyl formate. For reactions implemented in the presence of base additives, the formed formic acid will be further deprotonated by base to yield formate or formic acid/amine adduct with a highly negative enthalpy of -84.3 kJ/mol (equation 4, Table 1),⁶⁷ which can compensate the entropic factor and drive the overall reaction towards formate.

Table 1. Reaction thermodynamics for CO₂ reduction to formate/formic acid in the presence of different additives and solvents.

Entry	Reaction	$\Delta_r G^\ominus_{298K}$ (kJ/mol)	$\Delta_r H^\ominus_{298K}$ (kJ/mol)	$\Delta_r S^\ominus_{298K}$ (kJ/mol*K)
1	$\text{CO}_2(\text{g}) + \text{H}_2(\text{g}) \rightleftharpoons \text{HCOOH}(\text{l})$	32.9	-31.2	-0.215
2	$\text{CO}_2(\text{aq}) + \text{H}_2(\text{g}) + \text{H}_2\text{O} \rightleftharpoons \text{HCOO}^-(\text{aq}) + \text{H}_3\text{O}^+$	-4	-	-
3	$\text{CO}_2(\text{g}) + \text{H}_2(\text{g}) + \text{CH}_3\text{OH}(\text{l}) \rightleftharpoons \text{HCOOCH}_3(\text{l}) + \text{H}_2\text{O}(\text{l})$	-	-39.9	-
4	$\text{CO}_2(\text{g}) + \text{H}_2(\text{g}) + \text{NH}_3(\text{aq}) \rightleftharpoons \text{HCOO}^-(\text{aq}) + \text{NH}_4^+(\text{aq})$	-9.5	-84.3	-0.25



Scheme 1. Reaction equilibria associated with the dissolution of CO₂ in water

From a practical viewpoint, organic amine bases such as ethanolamine are preferred over inorganic bases, as they are widely used for the industrial CO₂ scrubbing process,⁶⁹ which could enable the integration of CO₂ capture and conversion in one step and medium. Besides, the employment of inorganic bases together with water as solvent would lead to the formation of multiple intermediates derived from CO₂ such as carbonic acid, carbonate, and bicarbonate (Scheme 1). The concentration of each species is governed by the complex equilibria among them, sensitive to reaction conditions such as pH,

temperature, water content, CO₂ pressure, and the properties of base. All of these species might be involved in catalytic CO₂ reduction, and the specific contributions of each component are difficult to determine experimentally. Likewise, the combined utilization of organic amine bases with water will give rise to a complex amine-water-CO₂ system comprising bicarbonate, carbonate, and carbamate. The speciation analysis of these components in various amine-CO₂ systems has been recently summarized in a review by Hu et al.⁷⁰ Moreover, it should be noted that CO₂ and its derived species exhibit different reactivity towards being reduced to formate. For instance, a TON of 6414 was obtained over a Pd nanocatalyst (Pd/C₃N₄) by using KHCO₃ as the carbon source and base in 3 h, whereas the TON was sharply decreased to 866 upon using CO₂ as the carbon source in the absence of KHCO₃.⁷¹ On the contrary, in the case of an Au nanocatalyst (Au/SiO₂-Schiff) reported by Liu et al.,⁷² formate was generated with a high TON of 14470 by using CO₂ in methanol/H₂O/NEt₃ without bicarbonate in 12 h, which is nearly 58 times higher than that obtained with KHCO₃ as the carbon source. These results clearly suggested that different reaction mechanisms were followed over the same catalyst, depending on the dominated form of CO₂ present in the reaction medium. A detailed discussion on the role of base in altering reaction pathway will be presented in a following mechanistic section (section 5.1).

3. Nanostructured metal catalysts

Historically, the first application of heterogeneous catalyst for the synthesis of formic acid/formate from CO₂ reduction dates back to the reduction of KHCO₃ using Pd black as the catalyst by Bredig and Carter in 1914.⁷³ Later on, Farlow et al. reported the direct hydrogenation of CO₂ to formate by a skeletal Raney Ni catalyst using amine as base in ethanol.⁷⁴ These early reported skeletal/bulk metal catalysts, featuring big metallic particles from hundreds of nanometers to micrometers, usually presented very low activities and fast deactivation due to their poor metal dispersion and easy aggregation. However, for a long time after these pioneering works, no major progress in heterogeneous reduction of CO₂ to formic acid/formate was achieved until the synthesis and application of nanocatalysis. Catalytic performances are greatly improved over nanostructured metal catalysts, which are characterized by a high surface to volume ratio with more active atoms exposed to CO₂ and H₂ as well as the unusual electronic structures at the nanoscale. Numerous nanostructured metal catalysts have been constructed based on noble metals including Ru, Pd, Au, and Ag, giving monometallic or bimetallic formulations through the rational combination of these metal components. Particle sizes of nanocatalysts are mostly in the range from sub-nanometers (clusters) to nanometers (nanoparticles). The active metal ensembles are generally dispersed on functionalized supports with basic properties giving classical supported-metal catalysts, or directly applied as colloidal catalysts in liquid phase, as illustrated in Figure 2. Catalytic performances of nanostructured metal catalysts are dependent on the metal component, support material, additive, and reaction conditions, as summarized in Table 2.

Table 2. Nanostructured metal catalysts for CO₂ hydrogenation to formic acid/formate

Entry	Catalyst	p_{H_2}/p_{CO_2} (bar/bar) ^a	Temp. (°C)	Solvent (v/v)	Additive	Time (h)	TON	TOF (h ⁻¹) ⁱ	Selectivity (%) ^j	ref.
1	Pd/AC	1/0	25	H ₂ O	NaHCO ₃	–	–	48 ^c	100	75
2	Pd/Mo ₂ C	10/10	100	H ₂ O	NaHCO ₃	24	72	–	–	77
3	Pd/BCN	25/25	40	H ₂ O	–	16	–	1.2	–	78
4	Pd/g-C ₃ N ₄	27/13	150	H ₂ O	NEt ₃	24	106	–	100	79
5	Pd/g-C ₃ N ₄	25/25	40	H ₂ O	–	16	–	1.1	–	80
6	Pd/ECN-1 h	25/25	40	H ₂ O	–	16	–	2.4	–	78
7	Pd/NMC	60/0	60	H ₂ O	KHCO ₃	3	1964	–	–	85
8	Pd/u-CN ₁₀₀	35/35	110	ethanol	NEt ₃	2	–	98.9	–	86
9	Pd/g-C ₃ N ₄	60/0	80	H ₂ O	KHCO ₃	1	5051	–	100	71
10	Pd/AC	50/30	40	[Bmim][OAc]	–	24	594	–	–	87
11	Pd/chitin	20/20	60	H ₂ O	Na ₂ CO ₃	1	–	257	–	88
12	Pd/r-GO	40/0	100	H ₂ O	KHCO ₃	32	7088	–	–	90
13	Pd/AC	55.2/0	20	H ₂ O	NH ₄ HCO ₃	2	1672 ^c	–	–	76
14	Pd/Al ₂ O ₃	27.5/0	20	H ₂ O	NH ₄ HCO ₃	1	278 ^c	–	–	76
15	Pd/CaCO ₃	27.5/0	20	H ₂ O	NH ₄ HCO ₃	1	20 ^c	–	–	76
16	Pd/BaSO ₄	27.5/0	20	H ₂ O	NH ₄ HCO ₃	1	212 ^c	–	–	76
17	Pd/ZnO	20/0	100	H ₂ O	NaHCO ₃	1	–	68 ^c	100	94
18	Pd/CeO ₂	20/0	100	H ₂ O	NaHCO ₃	1	–	366 ^c	100	94
19	Pd/TiO ₂	20/0	40	H ₂ O	NaHCO ₃	1	–	909 ^c	100	94
20	Pd/ZrO ₂ -M	20/0	100	H ₂ O	NaHCO ₃	1	–	1301 ^c	–	93
21	Pd/ZrO ₂ -T	20/0	100	H ₂ O	NaHCO ₃	1	–	2817 ^c	–	93
22	Pd/ZrO ₂ -M&T	20/0	100	H ₂ O	NaHCO ₃	1	–	1291 ^c	–	93
23	Pd nanoparticle suspension	50/80	80	methanol	NEt ₃	3	470	–	–	98
24	Pd-Al ₂ O ₃ @ICRM(3)	40/0	r.t.	1,4-dioxane/D ₂ O (3/2)	NaHCO ₃	8	580	–	–	99
25	Pd@ICRM(2)	40/40	40	1,4-dioxane/D ₂ O (3/2)	NEt ₃	20	250	–	–	99
26	Ru/γ-Al ₂ O ₃	50/83.5 ^b	80	ethanol	NEt ₃	1	139	–	100	100
27	Ru/HT	30/30	60	methanol/H ₂ O (5/1)	–	24	11389	–	–	103
28	Metallic Ru particles	50/80	80	methanol/H ₂ O (7.5/1)	NEt ₃	3	6351	–	–	104
29	EnCap Ru	72/72 ^b	70	ionic liquid ^d	–	4	–	11900 ^h	–	105
30	Ru ₃ (CO) ₁₂	40/30	70	DMSO/H ₂ O (5/1)	BMMI-OAc	168	17000	102.4	–	106

31	Ru-DBU/Al ₂ O ₃	60/60	80	ethanol	NEt ₃ / KH ₂ PO ₄	1	–	197	–	110
32	Ru-PPh ₃ /Al ₂ O ₃	60/60	80	ethanol/H ₂ O(4/1)	NEt ₃ / KH ₂ PO ₄ / PPh ₃	1	–	751	–	111
33	Au/TiO ₂ (AUROLite)	90/90 ^b	40	–	NEt ₃	888	18040	28	>99	116
34	Au/Al ₂ O ₃ (AUROLite)	20/20	70	ethanol	NEt ₃	20	215	–	–	117
35	Au/TiO ₂ (AUROLite)	20/20	70	ethanol	NEt ₃	20	111	–	–	117
36	Au/ZrO ₂ -9 ^e	80/80 ^b	120	methanol	–	3	–	102	>99	118
37	Au/SiO ₂ -Schiff	50/30	90	methanol/H ₂ O (4/1)	NEt ₃	12	14470	–	–	72
38	Au/SiO ₂ -NH ₂	50/30	90	methanol/H ₂ O (4/1)	NEt ₃	12	1026	–	–	72
39	Au ₃₆ (TBBT) ₂₄	22.5/7.5	120	H ₂ O	–	12	935 ^f	–	>80	120
40	Pd@Ag/TiO ₂	10/10	100	H ₂ O	NaHCO ₃	24	14839 ^c	–	>99	122
41	ZIF-8@PdAg@ZIF-8	10/10	100	H ₂ O	NaHCO ₃	24	1191	–	–	123
42	PdAg-PEI@HMOS	10/10	100	H ₂ O	NaOH	22	2754	125	–	124
43	PdAg/amine-RF10	10/10	100	H ₂ O	NaHCO ₃	24	867	–	–	126
44	PdAg/SBA-15-amine-5 ^g	10/10	100	H ₂ O	NaHCO ₃	24	874	–	>99	127
45	PdAg/amine-MSC	10/10	100	H ₂ O	NaHCO ₃	24	839	–	>99	125
46	Pd _{0.8} Co _{0.2} @MSN	10/10	100	H ₂ O	KHCO ₃	–	–	1824 ^c	–	128
47	PdNi/CNT-GR	25/25	40	H ₂ O	–	15	6.4	–	>99	129
48	Pd-Cu/ZnO/Al ₂ O ₃ ^e	50/10	150	methanol	–	10 min	–	38.15 ^c	–	131
49	PdMn _{0.6} @S-1	20/20	80	H ₂ O	NaOH	–	–	2151	–	130
50	colloidal RuFe	20/10	60	DMSO/ H ₂ O (78/1)	BMI-OAc	17	400 ^c	23.52 ^c	–	132

a Initial pressure at room temperature unless otherwise specified

b Pressure at reaction temperature

c TOF/TON based on the exposed metal atoms determined from metal dispersion

d Trihexyl (tetradecyl) phosphonium chloride

e Methyl formate was produced as the major product

f A rough estimation based on CO₂ conversion and formic acid selectivity

g Amine-5 denotes phenylamine in Scheme 3.

h TOF under supercritical condition

i Average TOF within the corresponding reaction time

j These reported high formate selectivities assumed no detection of other by-products in liquid and gas phase.

3.1 Pd-based nanocatalysts

Thus far, heterogeneous catalysts containing Pd nanoparticles or clusters have been extensively studied in catalyzing both bicarbonate and CO₂ reduction to formic acid/formate. Because of the excellent ability of Pd to adsorb and dissociate H₂, Pd-based nanocatalysts usually show superior activity to other transition metals, especially for bicarbonate reduction. For instance, González et al. reported that activated carbon-supported Pd catalyst (Pd/AC) was able to catalyze the hydrogenation of NaHCO₃ to sodium formate with a TOF of 48 h⁻¹ even at atmospheric H₂ pressure and room temperature (Table 2, entry 1).⁷⁵ For comparison, they also synthesized a series of AC-supported Ni, Ru, Co, and Re catalysts, which were inferior to Pd/AC in terms of TOF under the same reaction conditions. For the catalytic reduction of NH₄HCO₃ into formate at room temperature, Pd/AC also presented high activity with a TON of 782 in 1 h,⁷⁶ whereas negligible TONs (≤ 3) were obtained for other supported metal catalysts including Ru/AC, Pt/AC, Rh/AC and Ni/AC. Mitchell and co-workers reported a Mo₂C-supported Pd nanocatalyst (Pd/Mo₂C), affording higher TON than Mo₂C-supported Ru catalyst (72 vs 11) in 24 h at 100 °C in the presence of NaHCO₃ (Table 2, entry 2).⁷⁷ In addition, Pd nanoparticles dispersed on bulk carbon nitride (Pd/BCN) were recently proved to be effective in catalyzing the hydrogenation of CO₂ to yield free-form formic acid in the absence of base in water. A relatively low TOF of 1.2 h⁻¹ was obtained over Pd/BCN (Table 2, entry 3),⁷⁸ but this still surpassed the activities of Au/BCN and Ru/BCN with TOFs below 1 h⁻¹. These results demonstrated the intrinsically high activity of Pd nanoparticle toward bicarbonate/CO₂ hydrogenation regardless of the employed support and base. Pd particle size and the nature of support have been identified as two key factors to affect the activation of H₂ and adsorption of CO₂, which in turn determine the catalytic performances of Pd nanocatalysts. Here, we would like to put an emphasis on the promoting effects of various supports in dispersing and stabilizing Pd species as well as adsorbing and activating CO₂/bicarbonate.

3.1.1 Nitrogen-doped carbon supports

Nitrogen-doped carbon materials have received enormous interests due to their abundant nitrogen-containing functional groups such as amines, Schiff base, pyridinic-N, pyrrolic-N, and graphitic-N, which can serve as basic sites to capture and activate CO₂. Formic acid is probably produced at the interface of these basic functional groups with Pd nanoparticles via concerted catalysis. In 2014, Lee and co-workers were the first to apply mesoporous graphitic carbon nitride (g-C₃N₄) as support for Pd-catalyzed CO₂ reduction into formate in the presence of NEt₃ (Figure 2).⁷⁹ A TON of 106 was achieved at 150 °C and 40 bar total pressure over Pd/g-C₃N₄ in 24 h (Table 2, entry 4), which was 2-fold more active than commercial Pd/C catalyst. The high activity was ascribed to the basic sites of g-C₃N₄ to capture and concentrate CO₂ around Pd centers.

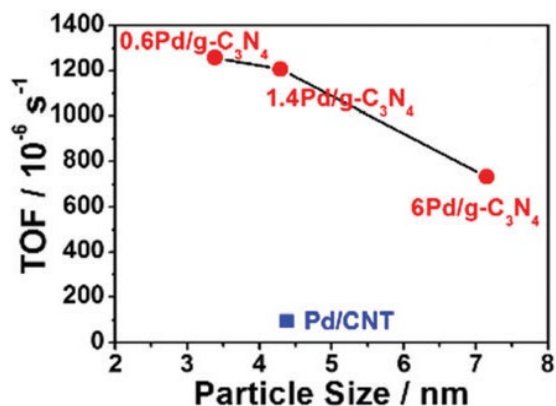


Figure 3. Effect of Pd particle size on catalytic activities of Pd/g-C₃N₄ for CO₂ reduction to formic acid. Reproduced with permission from ref. 80. Copyright 2016, Royal Society of Chemistry.

Following this work, Park et al. exploited Pd/g-C₃N₄ catalyst for CO₂ reduction to free formic acid in the absence of base, affording a TOF of 1.1 h⁻¹ (Table 2, entry 5).⁸⁰ In contrast, N-free carbon nanotube-supported Pd catalysts, possessing similar Pd particle size as Pd/g-C₃N₄ (4.38 vs. 4.29 nm), led to very poor activity with a TOF of 0.09 h⁻¹. CO₂-temperature programmed desorption (CO₂-TPD) profiles disclosed the much higher CO₂ adsorption capacity of g-C₃N₄ than carbon nanotube (CNT), which was proposed to account for its superior catalytic activities. A correlation was also found between catalytic activity and Pd particle size. As shown in Figure 3, with the particle size of Pd decreasing from 7.2 to 3.4 nm, a roughly two-fold increase of TOF was observed over Pd/g-C₃N₄. The superior catalytic activity achieved over small-sized Pd sites was ascribed to the increased number of interfacial sites between Pd nanoparticle and g-C₃N₄, which were proposed to serve as the true active sites for the formation of formic acid. The authors suggested that H₂ and CO₂ were firstly activated on Pd and g-C₃N₄, respectively, and then the activated H₂ and CO₂ species subsequently migrated to the interface of Pd/g-C₃N₄ to yield formic acid.

Related studies focusing on the basic properties of g-C₃N₄ revealed that CO₂ was mainly bonded to the primary and secondary amine groups arising from the edge defects on g-C₃N₄ probably in the form of carbamate.⁸¹⁻⁸³ To further improve the catalytic performances of Pd/g-C₃N₄, three methods with different post-treatment procedures, namely, thermal exfoliation of BCN (ECN), hard templating to form mesoporosity (MCN), and C-enrichment by copolymerization with 2,4,6-triaminopyridine, were applied to tune the basic properties of g-C₃N₄, targeting a high fraction of edge defects (Scheme 2).⁷⁸ A rapid thermal exfoliation (1 h) was found to be more efficient than other approaches in producing edge defects, resulting in the highest amount of basic sites. Therefore, the resultant Pd/ECN-1 h catalyst gave an enhanced TOF from 1.2 to 2.4 h⁻¹ compared to the pristine Pd/BCN catalyst (Table 2, entries 3 and 6). A positive correlation of the concentration of basic sites with the metal time yield of formic acid was established (Figure 4), indicating the important role of basic sites in promoting the formation of formic acid. By optimizing Pd loading, the best performance was reached at a medium Pd content of 1.47 wt% generating a large number of small-sized Pd particles (mean particle size = 5 nm). As a result, a higher fraction of Pd sites (H₂ splitting) in close proximity to the edge defects (basic sites) were formed. This finding further verified the above-mentioned critical role of interface sites between Pd and g-C₃N₄ in facilitating CO₂ reduction. In addition, a single-atom Pd catalyst supported on BCN was also examined for activity comparison with Pd nanoparticles. Under identical conditions, single-atom Pd catalyst only showed half activity of Pd nanoparticles. This was not surprising given that single-atom Pd usually situates in the six-fold cavity within the carbon nitride matrix,⁸⁴ which renders Pd sites relatively far from the edge defects. As such, the number of catalytically active interfacial sites of single Pd atom and basic edge defect was reduced, thus leading to poor activity.

Scheme 2. Synthetic methods with different post-treatment procedures to tune the basicity of g-C₃N₄. Reproduced with permission from ref. 78. Copyright 2018, Wiley-VCH.

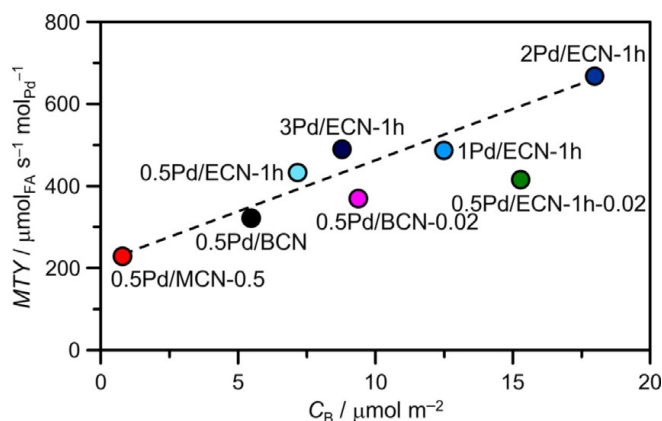
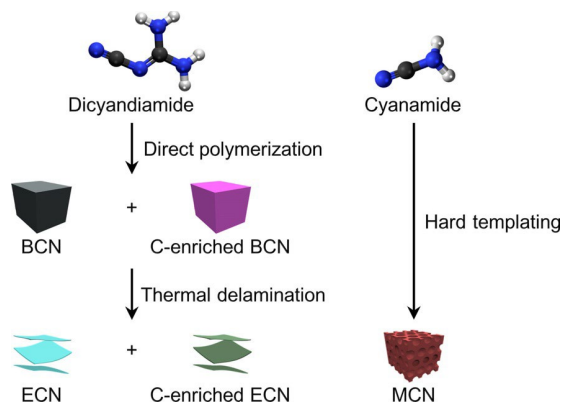


Figure 4. Correlation between the metal time yield of formate and the concentration of basic sites on C₃N₄-supported Pd catalysts. Reproduced with permission from ref. 78. Copyright 2018, Wiley-VCH.

In addition to providing basic sites, these N functionalities can act as anchoring sites for small Pd particles and Lewis base sites to regulate the electronic state of Pd, analogous to N-donor ligands in molecular catalysts. For example, Wang et al. prepared a nitrogen-doped mesoporous carbon (NMC) material possessing four types of nitrogen species including pyridine, pyrrole, nitrile, and quaternary N.⁸⁵ The employment of NMC as support led to smaller Pd particles (2.4 vs 3.1 nm) in comparison to MC-supported Pd catalysts. According to XPS, the binding energy of Pd⁰ in Pd/NMC was 0.4 eV smaller than that in Pd/MC, implying the relatively electron-rich Pd species on NMC due to the electron-donating effects of nitrogen functionalities. Apart from the dominant Pd⁰ species on Pd/NMC, a large fraction of Pd(II) species were also found. Pd/NMC was examined for the catalytic hydrogenation of KHCO₃ into formate, showing higher activity than Pd/MC in terms of KHCO₃ conversion (69.7 vs 45.2%). The enhanced activity by doping nitrogen was attributed to the strong interaction between nitrogen functionalities and Pd nanoparticles, which can facilitate the dispersion of Pd and enrich its electron density, thus facilitating H₂ activation. Yet, the potential contribution of Pd(II) species to the catalytic activity deserves further investigations. Besides, g-C₃N₄ and Schiff base-modified carbon nitride (u-CN₁₀₀) were found to be effective in improving the dispersion and charge density of active Pd atoms.^{71, 86} As shown in Figure 5, three types of N sites (i.e., N, N', N'') existed on carbon nitriles. Based on DFT calculations, Pd atoms were believed to bind to the sp²-hybridized N and N'' sites, which were more negatively charged and offered more diffused orbitals.⁷⁹ With the help of these Lewis basic nitrogen sites, ultra-small electron-enriched Pd particles with average sizes

of 1.57 and 1.9 nm were synthesized on Pd/u-CN₁₀₀ and Pd/g-C₃N₄, respectively, as evidenced by TEM and XPS. The resultant Pd/u-CN₁₀₀ catalyst gave a reasonable TOF of 98.9 h⁻¹ at 110 °C for the hydrogenation of CO₂ to formate in the presence of NEt₃ and ethanol (Table 2, entry 8).⁸⁶ When employing KHCO₃ as the carbon source, a high TON of 5051 was obtained on the Pd/g-C₃N₄ catalyst at 80 °C after 1 h (Table 2, entry 9).⁷¹

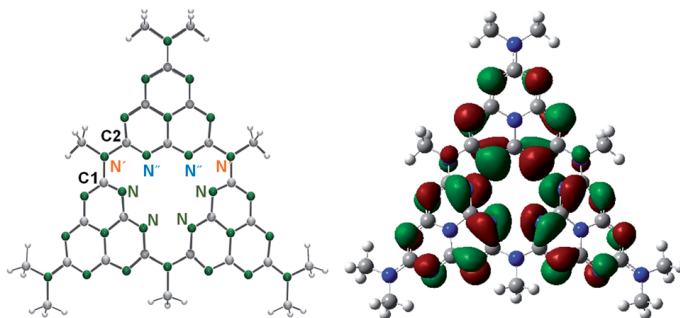


Figure 5. A DFT-optimized C₃N₄ structure containing the calculated molecular orbitals of different N atoms. Reproduced with permission from ref. 79. Copyright 2014, Royal Society of Chemistry.

It has been demonstrated that natural biopolymers such as chitin and chitosan containing N functionalities can function as a new type of N-doped carbon support to stabilize and modify Pd nanoparticles. For example, Wu and co-workers prepared highly-dispersed Pd particles on chitosan-derived carbon materials through the thermal pyrolysis of chitosan.⁸⁷ The resultant Pd/AC catalyst, with a small Pd particle size of 1.7 nm, can catalyze the reduction of CO₂ into free formic acid with a high TON of 594 in 24 h in the presence of 1-butyl-3-methylimidazolium acetate ([Bmim][OAc]) as solvent (Table 2, entry 10). By contrast, the commercial Pd/AC containing large Pd particles (4 nm) gave a much lower TON of 168 under same conditions, confirming the beneficial effects of N functionalities. In addition, it was discovered that [Bmim][OAc] could contribute to the catalytic performance by enhancing the electron density of Pd (electron donation of OAc⁻) and capturing CO₂ as an imidazolium carboxylate intermediate, as evidenced by XPS and NMR. In 2017, Song et al. reported the direct utilization of chitin as support to synthesize Pd/chitin catalyst for the hydrogenation of CO₂ to formate in the presence of Na₂CO₃.⁸⁸ Pd/chitin gave a 2-fold higher TOF (257 h⁻¹, Table 2, entry 11) than commercial Pd/C catalyst owing to the dual functions of acetamide groups in chitin, that is, anchoring small Pd nanoparticles and increasing the electron density of Pd.

The non-functionalized carbon materials with relatively inert surfaces such as AC and the reduced graphite oxide (r-GO) were also explored as support to immobilize Pd nanoparticles for the reduction of bicarbonate into formate,^{76, 89, 90} with medium to high activities achieved. For instance, Bi et al. reported a very high TON of 7088 over a r-GO-supported Pd nanocatalyst at 100 °C after 32 h (Table 2, entry 12). As a result of the lattice mismatch between Pd domains and r-GO, highly strained Pd nanoparticles with distorted electronic structures were formed on r-GO, which were believed to be responsible for the excellent activity of Pd/r-GO.⁹⁰ Su and co-workers performed the hydrogenation of NH₄HCO₃ into formate using a commercial Pd/C catalyst with a TON of 1672 at 20 °C after 2 h (Table 2, entry 13), which was much higher than that achieved using commercial Pd/Al₂O₃, Pd/CaCO₃, and Pd/BaSO₄ catalysts under identical conditions (Table 2, entries 14 to 16).⁷⁶ The superior performance of Pd/AC was attributed to the better dispersion of Pd on AC and the unique capability of AC to adsorb and store H₂ in its hydrophobic channels, thus leading to high local H₂ concentration for NH₄HCO₃ reduction. It is well known that AC is typically

pretreated in acid solutions prior to being employed as support. Accordingly, the generated oxygenated functional groups (e.g., carboxyl, hydroxyl, phenol, carbonyl, anhydride, etc.) along with the remaining acidic moieties (e.g., sulphate and nitrate) on AC might contribute to the stabilization of Pd.^{91, 92}

3.1.2 Metal oxide supports

In contrast to numerous studies on constructing Pd catalysts onto carbon-based materials, there are only few demonstrations of Pd catalysts supported on metal oxides with basic or amphoteric properties (e.g., Al₂O₃, ZrO₂, ZnO, CeO₂, TiO₂) for CO₂ reduction in the literature.^{89, 93, 94} Especially for reducible supports like ZrO₂, CeO₂, and TiO₂, they have rich surface oxygen vacancies capable of capturing and activating CO₂ upon reduction.^{95, 96} Generally, metal oxide-supported Pd catalysts exhibit inferior activity to Pd deposited on carbon-based materials, but most recently superior activity was reported by the group of Yan using Pd/TiO₂ catalysts with tailored basicity and H₂ activation activity.⁹⁴ Taking Pd/CeO₂ and Pd/ZnO as model catalysts, they first systemically studied the reaction kinetics to understand the kinetically relevant step over each catalyst and also monitored the formation of reaction intermediates on catalyst surface by *in situ* diffuse reflectance infrared Fourier transform spectroscopy (DRIFTS) under CO₂/H₂ atmosphere. The spectroscopic results showed that the *in situ* formed bicarbonate species on catalyst surface served as the key intermediate for the synthesis of formate. For Pd/ZnO with negligible basic properties, the relatively slow activation of CO₂ to yield bicarbonate was found to be the rate-determining step (RDS). In contrast, for Pd/CeO₂, H₂ splitting on Pd nanoparticles presented the RDS as the result of the abundant basic sites of CeO₂, thus accelerating the conversion of CO₂ into bicarbonate. By comparing these results, the authors concluded that there are two crucial parameters for highly-active metal oxide-supported Pd catalysts: sufficient density of basic sites and small Pd nanoparticles for CO₂ activation and H₂ dissociation, respectively. Based on these principles, they designed a highly efficient Pd catalyst by depositing small Pd nanoparticles (4.6 ± 0.9 nm) on TiO₂ featuring more basic sites than CeO₂ and ZnO. Indeed, the resultant Pd/TiO₂ catalyst afforded a TOF of up to 909 h⁻¹ for the reduction of NaHCO₃ into formate at 40 °C, far higher than that on Pd/CeO₂ and Pd/ZnO (Table 2, entries 17 to 19). In a follow-up study by the same group, an interesting dependence of catalytic activity on the crystalline phase of ZrO₂ was observed for a series of Pd nanoparticles supported on monoclinic ZrO₂ (ZrO₂-M), tetragonal ZrO₂ (ZrO₂-T), and hybrid ZrO₂ (ZrO₂-M&T).⁹³ Three types of ZrO₂ led to distinct basic properties for these Pd/ZrO₂ catalysts. Among them, Pd/ZrO₂-T displayed the highest activity with a TOF of 2817 h⁻¹ at 100 °C (Table 2, entries 20 to 22). Kinetic studies disclosed that CO₂ activation was the RDS over these Pd/ZrO₂ catalysts. The highest concentration of weak basic sites on ZrO₂-T enabling moderate binding with CO₂ was proposed to be responsible for the excellent activity of Pd/ZrO₂-T. Similarly, morphology-dependent catalytic activities were also reported for Pd/ZnO nanocatalysts using different ZnO supports (commercial, nanorods, nanoplates). The employment of ZnO nanorods gave the highest activity (TOF = 10.1 h⁻¹), which was attributed to the largest amount of weak basic sites on ZnO nanorods resulting from the predominantly exposed nonpolar (100) and (101) facets.⁹⁷

3.1.3 Unsupported Pd nanocatalysts

Unsupported Pd nanoparticles such as the suspended metallic Pd nanoparticles in methanol have been reported to be efficient for CO₂ reduction to formate in the presence of NEt₃, giving a TON of 470 in 3 h (Table 2, entry 23). However, a significant dissolution of Pd species was observed during the reaction.⁹⁸ A silica shell with a thickness of 8 nm was therefore introduced to prevent the dissolution of Pd. The resultant silica-coated Pd catalyst showed greatly improved stability against metal leaching during five

successive recycles with only a slight decrease of TON from 593 to 549. In addition, Lee and co-workers fabricated an interesting Pd-based nanoreactor by the interfacially cross-linked reverse micelles (Pd@ICRM), wherein Pd nanoparticles were encapsulated in the hydrophilic core of the polymerized surfactants (Figure 6A).⁹⁹ The catalytic performance of the nanoreactor was dependent on the head group of the employed surfactant which could bring either CO₂ or bicarbonate to the metallic Pd core. Quaternary ammonium-based catalyst Pd@ICRM(3) preferentially adsorbed bicarbonate (Figure 6B), and Al₂O₃-doped Pd@ICRM(3) gave a TON of 580 at room temperature and 40 bar H₂ after 8 h (Table 2, entry 24). By contrast, CO₂ tended to adsorb on the tertiary amine-based catalyst Pd@ICRM(2) (Figure 6B) affording a TON of 250 in 20 h in the presence of NEt₃ at 40 °C and 80 bar CO₂/H₂ (1/1) (Table 2, entry 25). Accordingly, substrate-recognizable reduction of CO₂/bicarbonate to formate was realized by engineering the microenvironments around Pd.

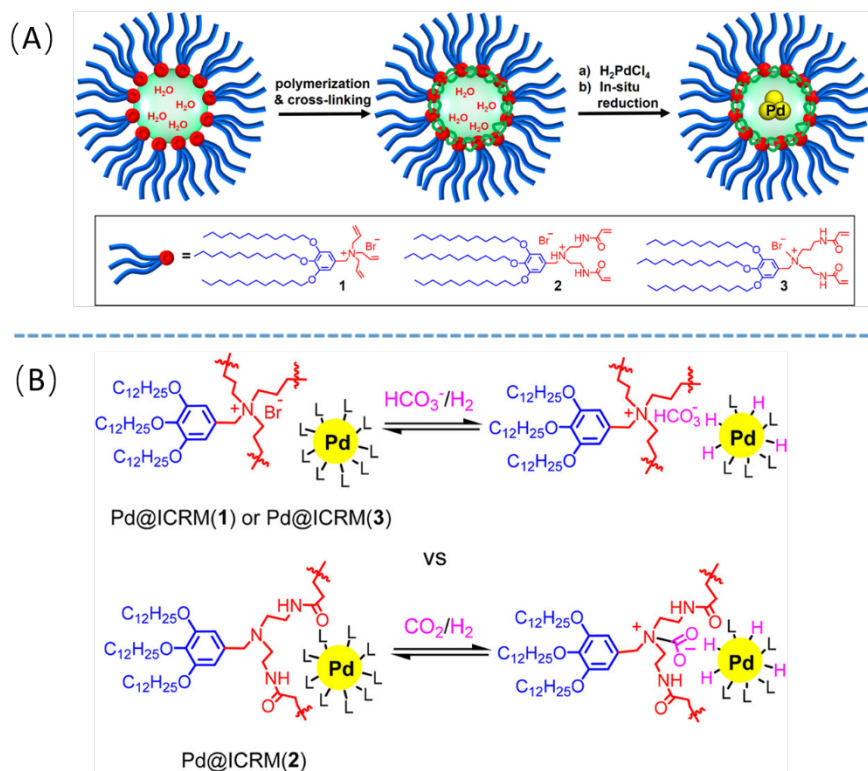


Figure 6. (A) Synthetic procedures for amine-based surfactants-encapsulated Pd nanocatalysts. (B) Substrate-recognizable reduction of CO₂/bicarbonate to formate by microenvironmental engineering of Pd nanoparticles. Reproduced with permission from ref. 99. Copyright 2017, American Chemical Society.

For Pd-catalyzed CO₂ hydrogenation, it is noteworthy that the majority of studies employed bicarbonate as the base and also the carbon source instead of a combination of gaseous CO₂ with NEt₃, as shown in Table 2. This is related to the superior activity of Pd-based catalysts for the catalytic reduction of bicarbonate compared to direct CO₂ reduction. Catalytic activities of Pd nanocatalysts strongly depend on

bicarbonate concentration. For example, Shao et al. compared the catalytic activities of Pd/g-C₃N₄ for CO₂ reduction to formate in the presence of NEt₃ with the direct reduction of bicarbonates to formate under identical conditions (80 °C, 60 bar H₂, 20 mL water).⁷¹ Utilizing KHCO₃ as the carbon source gave a two-fold higher TON than NEt₃-assisted CO₂ reduction (1883 in 1.5 h vs 866 in 12 h). Other types of bicarbonates including NH₄HCO₃ and NaHCO₃ also exhibited superior TONs to NEt₃-assisted CO₂ reduction. Interestingly, alkali hydroxides (KOH and NaOH) gave excellent TONs above 4000, probably owing to the high bicarbonate concentrations resulting from the reaction of alkali hydroxides with CO₂. A similar case also occurred for Pd/TiO₂ catalyst reported by Zhang et al.⁹⁴ In another study of bicarbonate hydrogenation, the dependence of catalytic performance (TOF) on bicarbonate concentration was revealed by comparing the TOFs of bicarbonates with different cations (e.g., Na⁺, K⁺, NH₄⁺).⁷⁶ These bicarbonates displayed the TOF order of NaHCO₃ (527 h⁻¹) < KHCO₃ (567 h⁻¹) < NH₄HCO₃ (782 h⁻¹), well consistent with the ascending trend of their bicarbonate concentrations in water, that is, NaHCO₃ (0.61 M) < KHCO₃ (0.89 M) < NH₄HCO₃ (0.92 M), as determined by ¹³C NMR.

To summarize, most endeavors have been directed to improve CO₂ adsorption and H₂ activation abilities of Pd nanocatalysts, which are associated with the number of basic sites and the dispersion Pd atoms, respectively. Engineering the basic properties of support materials to enhance CO₂ adsorption and stabilize small-sized Pd particles is widely used as an effective approach to fabricate highly-efficient Pd nanocatalysts. The cooperation catalysis of Pd nanoparticles with basic sites presumably on the interface of Pd and support is perceived as the key to achieve excellent performances.

3.2 Ru-based nanocatalysts

Ru-based nanocatalysts are another most examined catalytic metal system for CO₂ hydrogenation to formic acid/formate. The commonly used supporting materials to disperse Ru include Al₂O₃, hydrotalcite, AC, TiO₂, and silica. These supports are characterized by abundant hydroxyl groups on their surface to provide strong interaction with Ru, which has been claimed to be advantageous in enhancing the catalytic activity of Ru. For example, Hao et al. compared the catalytic activities of Ru species supported on γ -Al₂O₃, AC, and MgO.¹⁰⁰ The concentration of hydroxyl group followed the order of γ -Al₂O₃ > AC > MgO (almost no hydroxyl groups on MgO as measured by FTIR). Correspondingly, Ru/ γ -Al₂O₃ showed the highest TON of 91 followed by Ru/AC with a TON of 10, whereas MgO without hydroxyl groups was inactive for the hydrogenation of CO₂ to formate under identical conditions (ca. 80 °C, 50 bar H₂, 83.5 bar CO₂, 1 h, 5 mL NEt₃). Liu et al. reported the same beneficial effect of hydroxyl groups for Ru nanoparticles supported on γ -Al₂O₃ with varied morphologies.¹⁰¹ According to the literature,^{100, 102} the hydroxyl groups on metal oxides primarily play two roles in this reaction: (1) favoring the formation of highly-dispersed amorphous Ru species (hydroxide or metallic) and Ru single atom; (2) acting as hydroxyl ligands to increase the electron density of Ru, as will be discussed in Section 4.2.

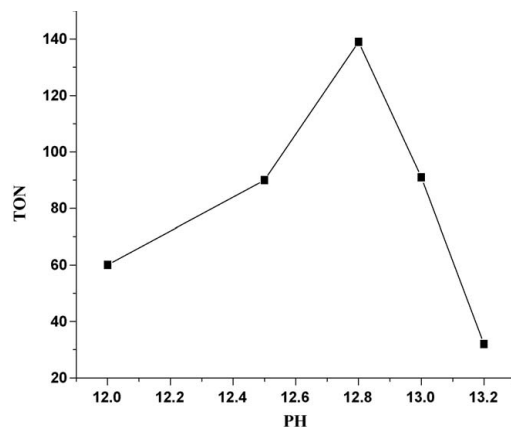


Figure 7. Dependence of formate formation on pH over Ru/ γ -Al₂O₃ catalysts for CO₂ reduction to formate. Reproduced with permission from ref. 100. Copyright 2011, Elsevier.

The catalytic performances of metal oxide-supported Ru catalysts strongly depend on the nature of Ru species. It was observed that highly dispersed amorphous Ru hydroxide species as well as Ru single atoms are more active than crystalline Ru oxide (RuO₂).¹⁰⁰ The structure of Ru species is influenced by Ru loading and the applied pH conditions during synthesis, which in turn affected catalytic activity. In the case of Ru/ γ -Al₂O₃ catalyst prepared under basic conditions,¹⁰⁰ it was found that the TON (in 1 h) of formate first increased to the highest value of 139 (pH = 12.8) and then sharply decreased to 32 (pH = 13.2), with increasing pH from 12 to 13.2, as shown in Figure 7. According to XRD, the formation of amorphous Ru hydroxide species was favorable at pH \leq 12.8, while crystalline RuO₂ phase started to form when pH > 13, thus leading to a huge drop in TON. With respect to the effect of Ru loading, a maximum TON of 90 in 1 h was achieved at a low Ru loading of 2 wt% for Ru/ γ -Al₂O₃, due to the predominant formation of highly-dispersed amorphous Ru hydroxide species, as indicated by XRD and TEM. Further increasing Ru loading to 6 wt%, the amorphous Ru hydroxide species aggregated to form RuO₂ crystallites, which resulted in a reduction of TON by 50. In addition, the synthesis of highly dispersed Ru hydroxide species can be realized by the co-precipitation of Ru³⁺, Mg²⁺, Al³⁺ to afford hydrotalcite-supported Ru catalyst (Ru/HT),¹⁰³ in which amorphous Ru hydroxide species were homogeneously incorporated into the framework of HT. Benefiting from the inherent basicity of HT, the Ru/HT catalyst afforded a TON of up to 11389 at 60 °C within 24 h in methanol/H₂O without base (Table 2, entry 27). Moreover, hydrotalcite could also be used to construct a well-defined single atom Ru catalyst within its matrix, as discussed later in section 4.2.

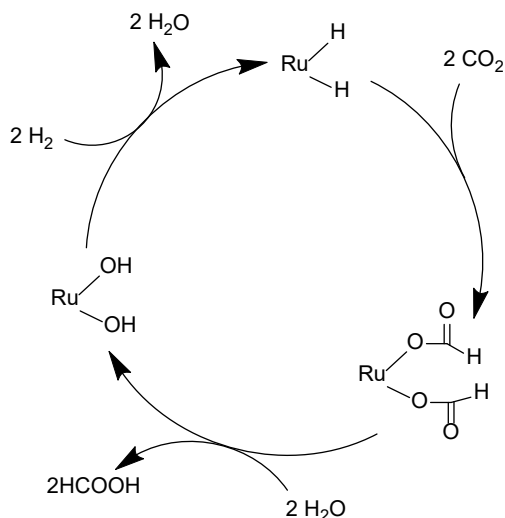


Figure 8. Proposed catalytic cycle for Ru hydroxide-catalyzed CO₂ hydrogenation to formate. Reproduced with permission from ref. 100. Copyright 2011, Elsevier.

Most nanostructured Ru catalysts for CO₂ hydrogenation involved metallic Ru species as the catalytically active component for H₂ dissociation. For example, colloidal Ru nanoparticles suspended in methanol prepared by *in situ* reduction of RuCl₃ was applied as an efficient catalyst for CO₂ reduction to formate.¹⁰⁴ The metallic Ru species afforded a high TON of 6351 at 80 °C after 3 h in methanol/H₂O/NEt₃ (Table 2, entry 28), whereas the unreduced catalyst containing Ru(III) species exhibited an inferior TON of approximately 500 under identical conditions. Kabra et al. described the application of metallic Ru nanoparticles supported on polyurea for the hydrogenation of supercritical CO₂ (144 bar H₂/CO₂),¹⁰⁵ yielding a high TOF of 11900 h⁻¹ at 70 °C in the presence of trihexyl (tetradecyl) phosphonium chloride as solvent (Table 2, entry 29). Such high efficiency was primarily ascribed to the employed supercritical conditions. A binary catalyst system, comprising metallic Ru clusters (Ru₃(CO)₁₂) and 1,2-dimethyl-3-butylimidazolium acetate (BMMI·OAc), was developed by Weilhard and co-workers.¹⁰⁶ A TON of 17000 was obtained at 70 °C and 70 bar CO₂/H₂ (3/4) after 168 h in the absence of base (Table 2, entry 30). The excellent performance was attributed to the multiple roles of BMMI·OAc: (i) a surfactant to stabilize the ultrasmall Ru clusters; (ii) a buffer to shift the equilibrium by neutralizing formic acid; (iii) capturing CO₂ and transforming it to bicarbonate; (iv) shifting equilibrium by reducing entropic difference. Apart from metallic Ru species, heterogeneous Ru(II) species were also found to serve as active as metallic Ru NPs for CO₂ reduction. For example, the amorphous Ru hydroxide species in the aforementioned Ru/HT and Ru/γ-Al₂O₃ catalysts were proved to have an oxidation state of +2 by XPS.^{100, 103} According to the mechanistic insights into homogeneous CO₂ reduction on Ru(II) complexes,¹⁰⁷⁻¹⁰⁹ amorphous Ru(II) hydroxide was proposed as the active site participating in the catalytic cycle. As shown in Figure 8, Ru(II) hydroxide was first transformed to Ru hydride species by H₂ accompanied by the elimination of water. By insertion into Ru-hydride, CO₂ was subsequently reduced to an intermediate of Ru-formate complex, which was finally released to form formate. Meanwhile, the Ru center was regenerated to the initial Ru(II) hydroxide species assisted by water.

In addition to base additives, the catalytic performances of Ru-based catalysts could be greatly promoted by adding proton sources such as H₂O and KH₂PO₄. For example, Zhang et al. synthesized a 1,8-diazabicyclo[5.4.0]undec-7-ene (DBU) modified Ru/Al₂O₃ catalyst (Ru-DBU/Al₂O₃) by a wet impregnation

method.¹¹⁰ The resultant Ru-DBU/Al₂O₃ catalyst showed much higher TOF (66 vs. 15 h⁻¹) than Ru/Al₂O₃. This is attributed to the nucleophilic nature of DBU capable of facilitating the formation of Ru-hydride species. Moreover, a substantial increase of TOF from 66 to 197 h⁻¹ was obtained upon the addition of KH₂PO₄ at 80 °C and 120 bar CO₂/H₂ (1/1) in ethanol/NEt₃ (Table 2, entry 31). Following this work, a well-known electron-donation ligand triphenylphosphine (PPh₃) was employed as the electronic promoter to enhance the H₂ splitting ability of Ru/Al₂O₃.¹¹¹ The modified Ru-PPh₃/Al₂O₃ catalyst exhibited high activity towards the formation of formate with a TOF of 263 h⁻¹ at 80 °C and 120 bar CO₂/H₂ (1/1) in ethanol/H₂O/NEt₃. The addition of an appropriate amount of KH₂PO₄ (ca. 3 mmol) resulted in a 3-fold increase of TOF of up to 751 h⁻¹ (Table 2, entry 32). As mentioned above, water is considered as a favorable solvent for CO₂ reduction as its solvation effect can compensate the unfavorable enthalpy contributions. Additionally, Umegaki et al. disclosed that adding a small amount of water (2 mL) can promote the formation of formate over metallic Ru colloids in methanol/NEt₃ with a TON of 6351 in 3 h, almost 13 times higher than that without water.¹⁰⁴ However, when adding an excess amount of water (ca. 4 mL), the TON was sharply reduced to one-sixth, which was due to the oxidation of metallic Ru species, as indicated by UV-Vis. This finding further emphasized the high activity of metallic Ru species. To sum up, the beneficial effect of adding proton sources could be ascribed to the enhanced electrophilicity of carbon atom in CO₂ by the formation of hydrogen bond between proton and CO₂, thus facilitating CO₂ insertion into Ru-hydride species, as is the case for homogeneous catalysis.^{112, 113}

In summary, the catalytic performance of Ru nanocatalysts is determined by the size and oxidation states of Ru species. By interacting with the hydroxyl groups on metal oxide supports, highly dispersed Ru nanoclusters in the form of Ru(II) hydroxides are formed and show higher activity than RuO₂. Unsupported metallic Ru nanoparticles stabilized by ionic liquid have been also demonstrated to show high activity. The addition of proton source (e.g., H₂O, KH₂PO₄) could exert activation effects on CO₂ probably by hydrogen bond interactions, thus improving the catalytic performance.

3.3 Au-based nanocatalysts

Au had long been perceived as inert for catalytic hydrogenation reactions because of its poor ability in splitting H₂. A turning point appeared in 1973, at which Bond and co-workers declared the outstanding catalytic activities of supported-Au particles when downsizing the particle size of Au to a few nanometers for olefin hydrogenation.¹¹⁴ It has become clear that Au-catalyzed hydrogenation reactions are structure-sensitive and the highly-dispersed Au species function as the real active site.¹¹⁵ However, the construction of ultra-small Au nanoparticles stabilized by a tailored support material remains a great challenge. As a result, the development of heterogeneous Au catalysts for CO₂ reduction to formate/formic acid significantly lags behind that of Pd- and Ru-based nanocatalysis, with only a few successful examples reported to date.

The first example was the application of a commercial Au/TiO₂ catalyst (AUROLite) for the continuous hydrogenation of CO₂ to formate in the presence of NEt₃ as both solvent and base reported by Preti et al.¹¹⁶ Au/TiO₂ was found to be very stable for a long-term test (37 days) and gave a total TON of 18040 (Table 2, entry 33), corresponding to a mass yield of up to 1.326 kg HCOOH/NEt₃ adducts. A tiny amount of CO was also produced as a side product with a selectivity of 0.5 %, possibly stemming from the competitive reverse water gas shift (RWGS) reaction. Following this study, Filonenko and co-workers performed a broad support screening to optimize the activity of Au nanoparticles, including Al₂O₃, TiO₂,

ZnO, CeO₂, MgAl-HT, MgCr-HT, and CuCr₂O₄.¹¹⁷ Catalytic activities of Au catalysts strongly depended on the choice of support. Among these supports, Au/Al₂O₃ displayed the highest activity with a TON of 215 at 70 °C within 20 h (Table 2, entry 34), two times higher than Au/TiO₂. The combined characterizations of XPS, XRD, H₂-TPR, together with cyanide leaching experiments, revealed that metallic Au species served as the real active site for H₂ dissociation. Considering the similar sized Au particles (1.9 vs. 2.6 nm) present on Al₂O₃ and TiO₂, the superior performance of Au/Al₂O₃ was likely related to the capability of Al₂O₃ in assisting the heterolytic dissociation of H₂ as well as adsorbing CO₂ in the form of bicarbonate. A detailed catalytic cycle will be elaborated in Section 5.2. Well-dispersed Au species on ZrO₂ was explored for base-free hydrogenation of CO₂ to methyl formate (MF) in methanol by Wu et al.¹¹⁸ The particle size of Au could be tuned by changing the applied pH conditions to deposit Au ions on ZrO₂. The smaller-sized Au/ZrO₂-9 catalyst (1.9 nm) synthesized at pH = 9 showed a TOF of 102 h⁻¹ (Table 2, entry 36), which was two-fold higher than that of the Au/ZrO₂-10.5 catalyst (2.4 nm) prepared at pH = 10.5.

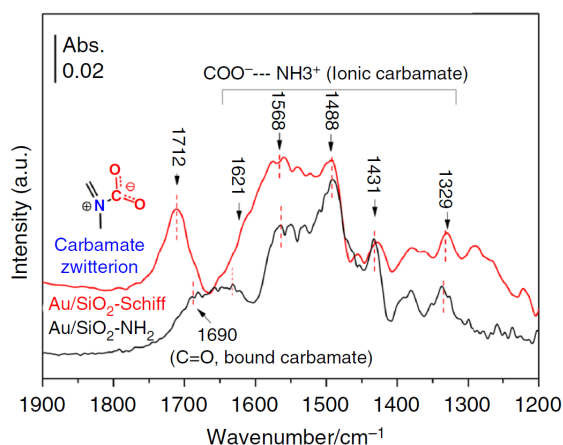


Figure 9. *In situ* FTIR spectra of Au/SiO₂-Schiff and Au/SiO₂-NH₂ under a CO₂/H₂O atmosphere. Reproduced with permission from ref. 72. Copyright 2017, Springer Nature.

Functionalizing support with nitrogen-containing moieties appears as an effective approach to improve the catalytic performance of Au catalysts. In 2017, Liu et al. demonstrated that the Schiff-base modified SiO₂ could serve as an excellent support to disperse ultra-small Au nanoparticles (< 2 nm), which were highly active for the direct reduction of CO₂ to formate.⁷² Under optimized conditions (80 bar H₂/CO₂ (5/3), 90 °C, H₂O/CH₃OH (20:80, v/v)), a high TON of 14470 was reached over Au/SiO₂-Schiff in the presence of NEt₃ in 12 h (Table 2, entry 37). In contrast, primary amine modified Au catalyst (Au/SiO₂-NH₂) afforded a much lower TON of 1026 under identical conditions (Table 2, entry 38). Based on experimental, characterization, and computational results, the excellent performance of Au/SiO₂-Schiff was attributed to the dual functions of Schiff-base moiety. First, CO₂ was weakly bound to Schiff-base group via the formation of a reactive intermediate of zwitterion adduct (Figure 9), while CO₂ was predominately transformed into a relatively stable ionic carbamate by reacting with the primary amine group on Au/SiO₂-NH₂. Second, electron-donating effects render Au negatively charged, favoring the formation of reactive hydride species. In contrast to the superior capability of Pd in reducing bicarbonates, Au/SiO₂-Schiff exhibited a poor activity for NaHCO₃ reduction (without pressurizing CO₂) with a TON as low as 195 in 12 h. It was therefore concluded that the reaction proceeded over Au/SiO₂-Schiff catalyst not via conventional carbonate/bicarbonate intermediates, but rather via the zwitterion adduct formed between the Schiff-base moiety and CO₂ (Figure 9), as proven by *in situ* DRIFTS. Moreover, they synthesized a purely

single-atom Au/SiO₂-Schiff catalyst, which was proved to be inactive for CO₂ reduction. The cationic and electron-deficient nature of singly-dispersed Au sites might account for their inert catalytic behaviors. A follow-up study by the same group disclosed the size-dependent catalytic activities of Au/SiO₂-Schiff.¹¹⁹ By using a solid-state reduction method, they synthesized a series of Au/SiO₂-Schiff catalysts with different sizes ranging from 1 to 7.3 nm. With increasing Au particle size from 1 to 2.8 nm, a notable decline of the TON (in 7 h) of formate from 9278 to 2997 was observed. No product was formed when further increasing Au particle size to 7.3 nm. As revealed by XPS, with decreasing particle size to sub-nanoscale, Au species were gradually becoming electron-rich due to the transition of electronic structures from continuous to discrete energy bands, which was proposed to account for the observed particle size dependence.

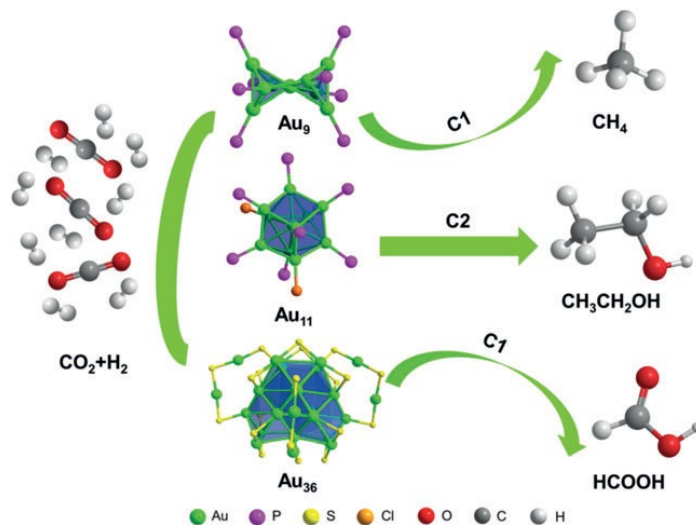


Figure 10. Size-dependent catalytic reduction of CO₂ into different products over ligand-protected Au clusters. Reproduced with permission from ref. 120. Copyright 2020, Wiley-VCH.

Most recently, Yang et al. reported the dependence of product selectivity on the sizes and electronic structures of Au clusters.¹²⁰ They prepared three well-defined Au clusters with different atomicity including [Au₉(PPh₃)₈](NO₃)₃ (Au₉), [Au₁₁(PPh₃)₈Cl₂]Cl (Au₁₁), and Au₃₆(TBBT)₂₄ (Au₃₆) capped by various organic ligands (Figure 10). These Au clusters were further deposited on ZrO₂, CeO₂ and SiO₂ and examined for CO₂ hydrogenation. Regardless of the applied supports, Au₃₆ catalysts always displayed high selectivity towards formic acid (> 80%) at 120 °C after 12 h (Table 1, entry 39), whereas methane (~ 90%) and ethanol (> 80%) were produced as the main products over the Au₉ and Au₁₁ catalysts, respectively. The utilization of different organic ligands led to similar product distributions, suggesting that the distinct product selectivities were related to the different intrinsic activities of Au clusters. According to EXAFS results, all Au species were present as positively charged and average oxidation state increased following the order of Au₃₆ < Au₁₁ < Au₉, indicating their distinct electronic energy levels due to the quantum size effect. As a result, these clusters displayed different binding abilities towards specific reaction intermediates (e.g., HCOO*, COOH*, CO*, CH₂*), thus resulting in varied product selectivities, as confirmed by DFT calculations. For the Au₃₆ catalyst, its weak binding strength towards HCOO*, followed by facile hydrogenation, enabled the kinetically-favored formation of formic acid.

In summary, the size of Au ensembles has been identified as the key parameter governing the activity of Au nanocatalysts. Moderate activities can be obtained on small sized metallic Au nanoparticles (1–2 nm) dispersed on various metal oxides including SiO₂, TiO₂, Al₂O₃, and ZrO₂. The functionalization of SiO₂ with

Schiff-base groups leads to a significant enhancement in the activity, owing to the promotional roles of Schiff-base groups in activating CO₂ and generating electron-rich Au atoms. Product distribution can be regulated by tailoring the number of Au atoms in the unsupported Au clusters stabilized by P-based ligands. The increase of Au atomicity from Au₉ to Au₃₆ results in the main product switching from methane to formic acid as a result of the distinct electronic properties of Au nanoclusters.

3.4 Bimetallic nanocatalysts

Bimetallic nanoparticles often bear distinct electronic and geometric structures compared to their monometallic counterparts, thus giving rise to unique catalytic behaviors in heterogeneous catalytic reactions.¹²¹ In this regard, quite a few bimetallic nanocatalysts have been developed for the hydrogenation of CO₂ to formate/formic acid. With respect to catalyst formulation, Pd was the most commonly used active component, which is typically modified by a second transition metal such as Ag, Au, Co, Cu, Mn, and Ni. The geometric and electronic properties of Pd can be tailored by chemically bonding with the doped metals as well as by architecture engineering (e.g., alloy, isolated, core shell). As a result, an improvement in activity was usually observed on transition metal-modified Pd catalysts.

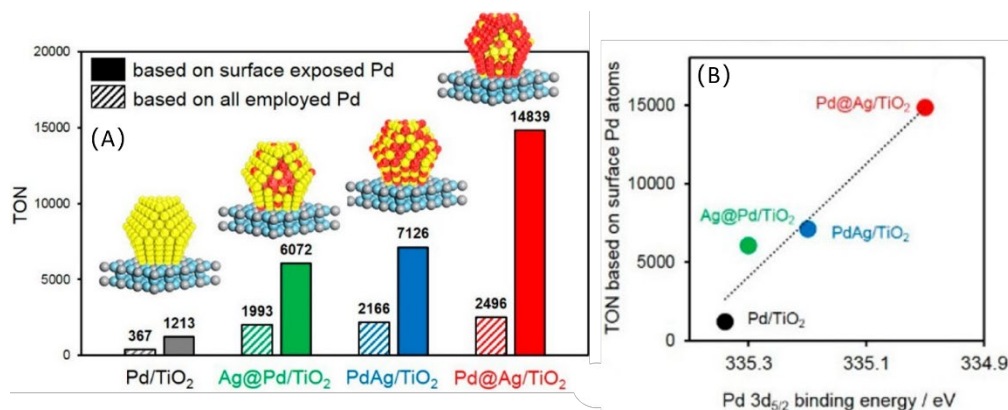


Figure 11. (A) Catalytic performances of bimetallic PdAg catalysts with different nano-architectures for CO₂ reduction to formate. Pd and Ag are denoted by yellow and red colors, respectively. (B) Correlation between Pd 3d_{5/2} binding energy and the TON (in 24 h) for CO₂ hydrogenation to formate over various bimetallic PdAg catalysts. Reproduced with permission from ref. 122. Copyright 2018, American Chemical Society.

Yamashita et al. demonstrated excellent catalytic activities of PdAg nanoparticles arising from the positive alloying effect of Ag with Pd.¹²² They prepared a series of PdAg alloy nanoparticles with tailored architectures including Pd@Ag/TiO₂ (Pd core, Ag shell), Ag@Pd/TiO₂ (Ag core, Pd shell), and PdAg/TiO₂ (random distribution), as shown in Figure 11A. In the case of Pd@Ag/TiO₂, most Pd atoms resided in the core of PdAg alloy nanoparticles with a few Pd atoms being exposed on the surface surrounded by Ag atoms in an isolated configuration, as proven by scanning transmission electron microscope and energy dispersive spectroscopy mapping (STEM-EDS), EXAFS, and CO-FTIR. These PdAg nanoparticles were examined for CO₂ reduction to formate at 100 °C for 24 h under 20 bar H₂/CO₂ (1/1) in the presence of NaHCO₃. The unique architecture of Pd@Ag/TiO₂ enabled the highest TON of 14839 in 24 h (Table 2, entry 40), 12-fold higher than the monometallic Pd/TiO₂ catalyst (Figure 11A), whereas no product was observed over Ag/TiO₂ catalyst. Obviously, the intrinsic activity of Pd atoms can be remarkably improved upon alloying with Ag atoms. XPS and CO-FTIR revealed the electron transfer from Ag to Pd atoms on all

PdAg particles because of the higher electronegativity of Pd than Ag (2.2 vs 1.9). Among others, Pd atoms in Pd@Ag/TiO₂ were the most negatively charged. Notably, a nearly linear correlation could be established between the binding energy of Pd 3d_{5/2} and TON in 24 h (Figure 11B). The TON increased as the Pd 3d_{5/2} binding energy decreased (indicating the electron-enriched Pd). Accordingly, the excellent performance of Pd@Ag/TiO₂ was attributed to the formation of electron-rich and isolated Pd atoms by binding with neighboring Ag atoms. Based on DFT and kinetic investigations, it was concluded that Ag atoms just served as electronic modifiers to enrich the electron density of Pd rather than providing active sites for the catalytic cycle. Furthermore, the underlying reason for the high activity of electron-rich Pd species was revealed by DFT calculations. Pd atoms with high electron density could produce reactive hydride species with enhanced hydricity, thus significantly reducing the kinetic barrier of the nucleophilic attack of hydride at bicarbonate by 130.5 kJ/mol.

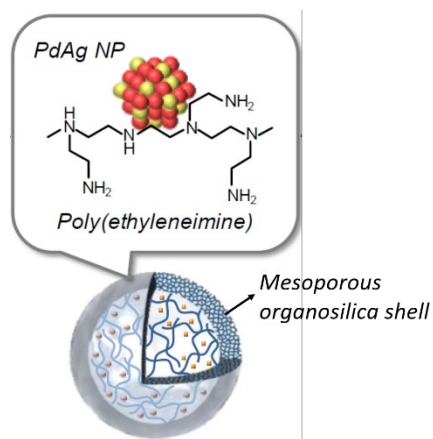


Figure 12. Structural representation of a hollow nanostructured PdAg catalyst by encapsulating PdAg nanoparticles along with PEI into a hollow mesoporous organosilica sphere. Reproduced with permission from ref. 124. Copyright 2020, American Chemical Society.

In an effort to improve the durability of PdAg catalyst, Wen and co-workers encapsulated PdAg nanoparticles into a zeolitic imidazolate framework (ZIF-8) affording a core-shell structure to suppress the aggregation of PdAg nanoparticles (ZIF-8@PdAg@ZIF-8).¹²³ The spatially-confined PdAg alloy nanoparticles showed an improved stability with a nearly unchanged TON of around 1191 in 24 h for three consecutive activity tests (Table 2, entry 41). In another work, the group of Yamashita reported the encapsulation of PdAg nanoparticles along with branched polyethylenimine (PEI) into a hollow mesoporous organosilica sphere (HMOS) as a bifunctional catalyst to activate both CO₂ and H₂.¹²⁴ As shown in Figure 12, the introduced PEI containing abundant amine moieties was in close proximity to PdAg nanoparticles, functioning as CO₂-adsorbing sites to concentrate CO₂ in the vicinity of H₂ activation sites (PdAg). As a result, a wealth of catalytically active interfacial sites were created on the bifunctional PdAg-PEI@HMOS catalyst, as is the case for the aforementioned Pd/g-C₃N₄ catalyst. Benefiting from the cooperative catalysis of PdAg and PEI, a superior TON of 2754 was achieved in aqueous NaOH solution under 20 bar CO₂/H₂ (1/1) within 22 h (Table 2, entry 42). Meanwhile, PdAg-PEI@HMOS exhibited excellent stability without activity decline during five successive tests affording a total TON of 13700 in 110 h. However, a pronounced deactivation occurred in the second test for the non-encapsulated PdAg/PEI catalyst. The enhanced recyclability was ascribed to the confinement effect and alkali-tolerant nature of organosilica shell. Interestingly, kinetic studies showed a negative apparent activation energy of

-11.3 kJ/mol on PdAg-PEI@HMOS, featuring enhanced activity with decreasing reaction temperature. This is likely related to the favorable CO₂ enrichment at low temperatures due to the strongly exothermic nature of CO₂ adsorption on PEI ($\Delta_r H^\theta = -83$ kJ/mol).

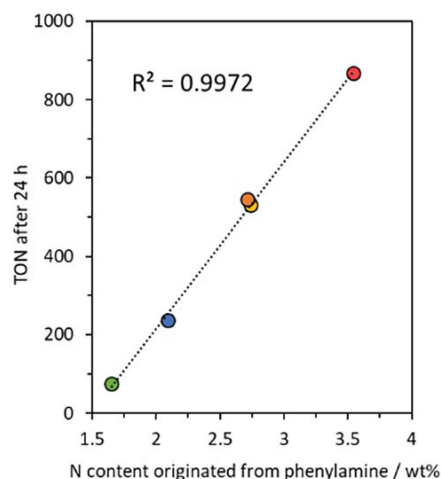
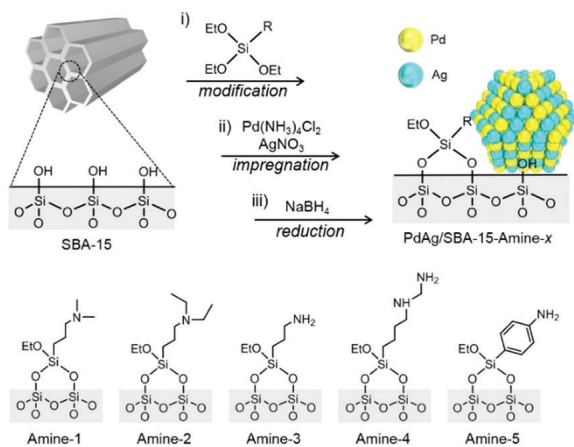


Figure 13. Correlation between the TON of CO₂ reduction to formate and the N content in different PdAg/amine-RF catalysts measured by XPS. Reproduced with permission from ref. 126. Copyright 2019, Royal Society of Chemistry.

Scheme 3. Schematic illustration for the synthesis of PdAg nanoparticles modified by various amines on SBA-15 (PdAg/SBA-15-amine-x). Reproduced with permission from ref. 127. Copyright 2017, Royal Society of Chemistry.



The same group also developed a number of amine-functionalized materials as supports to further improve the catalytic activities of PdAg alloy nanoparticles.¹²⁴⁻¹²⁷ The introduction of amine moieties to disperse PdAg alloy nanoparticles possesses four advantages: (i) promoting the formation of smaller nanoparticles; (ii) donating electrons to Pd; (iii) assisting the reduction of bicarbonate intermediate by forming hydrogen bonds; and (iv) CO₂ adsorption. For example, they prepared PdAg nanoparticles

supported on amine-containing polymers by Mannich reaction of resorcinol and 4,6-diaminesorcinol hydrochloride (PdAg/amine-RF).¹²⁶ The catalytic performances of PdAg/amine-RF catalysts for CO₂ reduction to formate could be linearly correlated to their N contents (Figure 13). A maximum TON of 867 was obtained over PdAg/amine-RF10 with the highest N content (ca. 3.8 wt%) in 24 h (Table 2, entry 43). With the increase in amine content, the particle size of PdAg monotonously decreased from 4.8 to 2.3 nm possibly due to the increased formation of Pd-N bonds, as evidenced by TEM and EXAFS. Meanwhile, XPS indicated that high amine content led to electron-enriched Pd species resulting from the electron transfer from amine groups, in addition to the electron-donation effect of Ag atoms. DFT calculation showed that the activation energy for formate production could be notably lowered to 156.2 kJ/mol over the amine-modified PdAg nanoparticles, in comparison to the unmodified counterpart ($E_a = 300$ kJ/mol). Accordingly, the superior activity of PdAg/amine-RF10 with high amine contents was ascribed to the presence of well-dispersed electron-rich PdAg nanoparticles as well as the assisting role of amine groups in reducing bicarbonate. The influence of various amines modified PdAg nanoparticles on the synthesis of formate was also studied.¹²⁷ Among the examined amines in Scheme 3, the highest activity was obtained over phenylamine-modified PdAg nanoparticles with a TON of 874 in 24 h at 100 °C under 20 bar H₂/CO₂ (1/1) (Table 2, entry 44). The superior performance was speculated to be related to the relatively weak basicity of phenylamine, which can enable moderate interactions with reaction intermediates (e.g., bicarbonate, formate). However, further studies are required to achieve a clear understanding of the underlying reason. A follow-up study from the same group explored phenylamine-modified mesoporous carbon to immobilize PdAg alloy nanoparticles (PdAg/amine-MS).¹²⁵ The PdAg/amine-MS catalyst showed a TON of 839 in 24 h (Table 2, entry 45), which was 2-fold higher than that over monometallic Pd/amine-MS and unmodified PdAg/MS catalysts. The adsorption capacity of MSC towards CO₂ was improved by 1.5 times upon modifying with phenylamine, thus contributing to the high activity of PdAg/amine-MS. Compared with the unmodified PdAg nanoparticles, the introduction of phenylamine led to a notable reduction of PdAg particle size by 2-fold, thus leading to superior activity. As indicated by DFT calculations, the activation energy of formate formation was substantially reduced compared to that without phenylamine (134.3 vs 236.4 kJ/mol), due to the formed hydrogen bonds between phenylamine and bicarbonate intermediate. This was proposed as another reason for activity enhancement, which, however, needs to be verified by experimental evidences.

Scheme 4. Schematic illustration for the one-pot synthesis of PdCoO nanoparticles confined in the mesoporous channels of silica nanospheres. Reproduced with permission from ref. 128. Copyright 2019, Wiley-VCH.

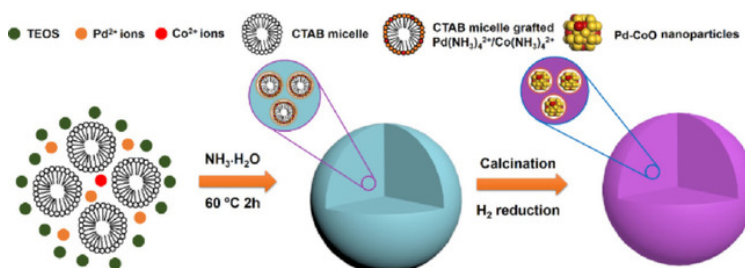




Figure 14. Schematic representation for the synthesis of PdMn_{0.6}@S-1 catalyst. Reproduced with permission from ref. 130. Copyright 2020, Wiley-VCH.

Non-noble metals, including Co, Ni, Mn, and Cu, appear as suitable components to modify Pd affording cost-effective bimetallic nanocatalysts. For instance, Sun et al. reported in 2019 the embedded PdCo nanoparticles into mesoporous silica nanospheres (MSN) by a one-pot ligand-protected method (Scheme 4).¹²⁸ As a result of the spatial confinement of MSN, evenly distributed PdCo nanoparticles with an average size of 1.7–1.9 nm were obtained, whereas the conventional impregnation method gave a larger size of 4.4 nm. It was observed that the metallic Pd 3d peak shifted to lower binding energies in XPS spectra with the addition of Co, indicating an electron transfer from Co to Pd. At the optimal Pd/Co molar ratio of 0.8/0.2, Pd_{0.8}Co_{0.2}@MSN afforded a high TOF of 1824 h⁻¹ at 100 °C in aqueous KHCO₃ solution (Table 2, entry 46), which was four-fold higher than monometallic Pd@MSN. The enhanced performance was attributed to electron-rich Pd centers as well as ultrafine PdCo particles. Besides, the encapsulated PdCo nanoparticles could be reused 5 times without aggregation and loss of activity, indicating their excellent recyclability. Nguyen and co-workers described the use of PdNi alloy nanoparticles supported on carbon nanotube-graphene (CNT-GR) as an efficient catalyst for base-free hydrogenation of CO₂ to formic acid in water.¹²⁹ HRTEM and XRD confirmed the formation of PdNi alloy with randomly distributed Pd and Ni atoms, wherein Pd atoms were slightly negatively charged due to electron transfer from Ni to Pd, as indicated by XPS. In comparison to Pd/CNT-GR, a more than two-fold increase of activity was observed over PdNi/CNT-GR (TON = 6.4) at 40 °C in 15 h under 50 bar H₂/CO₂ (1/1) in water (Table 2, entry 47). DFT calculations indicated that the improved performance was tentatively ascribed to the synergetic catalysis of Pd and Ni active centers, that is, H₂ dissociated to hydride species on electron-rich Pd sites and electron-deficient Ni sites could activate CO₂ by binding to O atom. Sun and co-workers designed a highly active and stable PdMn alloy catalyst (PdMn_{0.6}@S-1) by encapsulating ultra-small PdMn nanoclusters (<0.7 nm) into silicalite-1 zeolites via an *in situ* ligand-stabilized hydrothermal approach (Figure 14).¹³⁰ The resultant PdMn_{0.6}@S-1 catalyst gave a high TOF of 2151 h⁻¹ at 80 °C in aqueous KOH solution (Table 2, entry 49), and could be recycled 5 times with unchanged TOFs thanks to the outstanding confinement effects of silicalite-1 micropores. The superior activity was mainly ascribed to the addition of Mn to form PdMn alloy phases. This unique alloying effect was proved to enhance the electron density of Pd atoms but also promote the conversion of CO₂/carbonates to bicarbonates, a key step for CO₂ reduction to formate. Tsang et al. explored the commercial Cu/ZnO/Al₂O₃ catalyst, well-known for methanol synthesis, for the hydrogenation of CO₂ to MF.¹³¹ Under mild conditions (150 °C, 10 bar CO₂, 50 bar H₂, 25 h), Cu/ZnO/Al₂O₃ gave a TOF of 31 h⁻¹, which was further improved to 38 h⁻¹ by adding Pd atoms (1 wt%) owing to the excellent H₂ spill-over ability of Pd atoms (Table 2, entry 48). In contrast, doping the catalyst with other transition metals (e.g., Ru, Ni, Au,) afforded inferior TOFs to that of Pd-Cu/ZnO/Al₂O₃.

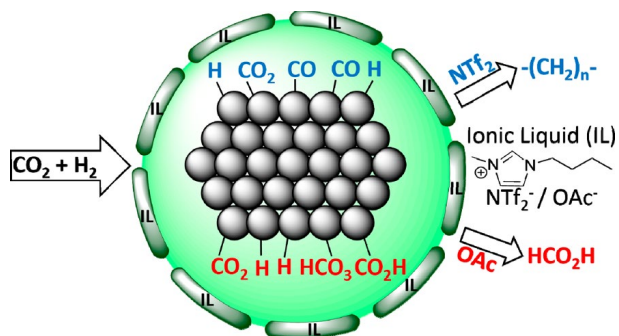


Figure 15. Selectivity-switchable conversion of CO₂ to formic acid or hydrocarbons over RuFe alloy nanocatalysts encapsulated in different ionic liquids. Reproduced with permission from ref. 132. Copyright 2018, American Chemical Society.

Interestingly, Qadir and co-workers designed a colloidal RuFe alloy nanocatalyst capped by an ionic liquid shell, which could realize selectivity-switchable conversion of CO₂ to formic acid or hydrocarbons (Figure 15).¹³² The anion type in ionic liquids was uncovered to regulate the microenvironments around RuFe active sites, thus directing the reaction pathways. A non-basic ionic liquid BMI-NTf₂ together with RuFe alloy nanoparticles gave rise to C₅–C₆ hydrocarbons as main products (78% selectivity). It was reasoned that the hydrophobic and non-basic nature of NTf₂ render the microenvironments around the RuFe active sites favorable to accommodate the required intermediates species such as CO₂, CO, CH₂^{*}, HCO^{*}, HCOH^{*}, CH^{*} for hydrocarbons formation. These species were typically generated from RWGS and the subsequent chain propagation via Fischer–Tropsch synthesis (FTS). In contrast, the combination of hydrophilic BMI-OAc with RuFe alloy nanoparticles could catalyze the hydrogenation of CO₂ to formic acid with a TON of 400 in 17 h at 60 °C in DMSO/H₂O under 30 bar H₂/CO₂ (2/1) (Table 2, entry 50). The sole application of Fe nanoparticles was inactive. A TON as low as 19 was reached over monometallic Ru nanoparticles. These results suggested the beneficial effects of incorporating Fe into Ru. However, the origin of the enhanced activity of Ru by forming alloy with Fe is not clear yet. The basic and hydrophilic nature of BMI-OAc play double roles in promoting the formation of formic acid: as a buffer system to stabilize formic acid and favoring the formation of bicarbonates. Acetate anions (OAc⁻) were proven to dissociate water molecules to hydroxide species, which subsequently reacted with the trapped CO₂ to form bicarbonates, as indicated by the *in situ* high-pressure (HP)-NMR.¹³³ Bicarbonates were therefore proposed as the reactive intermediates being reduced on active RuFe sites to yield formic acid.

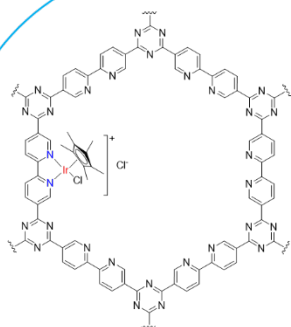
In summary, the reported studies involving bimetallic catalysts are principally oriented to improve the activity of Pd atoms by adding a second metal component. Many transition metals have been applied to form alloy with Pd and donate electrons to Pd atoms. As a result, electron-rich Pd sites and electron-deficient metal sites are generated. The synergistic catalysis arising from these two types of metal sites will facilitate the dissociation of H₂ to form hydride species featuring high reactivity to reduce CO₂. To improve catalyst stability, a series of porous materials including MOF, zeolite, and mesoporous silica have been utilized as supports to encapsulate and confine the small-sized bimetallic nanoclusters in their microporous or mesoporous channels.

4. Single-atom Catalysts

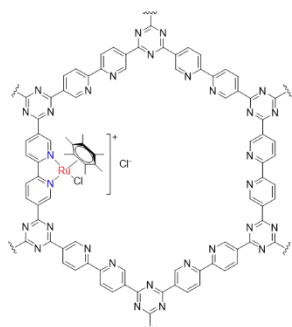
With respect to nanocatalysts, especially for Pd- and Au-based catalysts, the metal–support interface was usually considered as the catalytically active center, wherein both H₂ dissociation on metal sites and CO₂ adsorption/activation on basic supports (e.g., N-doped materials, ZrO₂, CeO₂, TiO₂) could take place in a concerted manner. In a recent work, the perimeter sites of SiO₂-supported Ag nanoparticles have also been identified as the active centers for CO₂ hydrogenation to MF.¹³⁴ Therefore, it can be expected that when the active metal ensembles are downsized to single atom dispersion, the maximized interfacial sites will be achieved on SACs, wherein each metal atom bound to neighboring atoms act as an active center. Obviously, SACs can make full use of metal atoms and possess defined structures, resembling homogeneous metal complexes. However, the reduction of particle size is accompanied by the enhanced tendency of aggregation due to the increased surface free energies of the metal atoms.⁴⁸ Besides, catalytic behaviors of SACs primarily depend on their electronic properties (more likely atomic orbitals), which are strongly affected by surrounding atoms. On these grounds, structure engineering of supporting materials with tailored binding sites to regulate the electronic properties of metal centers is of utmost importance in designing efficient SACs for CO₂ reduction. In this respect, homogeneous catalysis has provided valuable clues for the synthesis of high-performance SACs, namely, well-defined molecular structures of metal complexes with achieved molecular level understandings. In particular, the well-developed immobilization of mononuclear metal complexes onto solid supports (e.g., silica, organic polymers, MOFs) represents a straightforward approach to fabricate heterogeneous SACs.¹³⁵⁻¹³⁷ Although immobilized metal complexes containing mononuclear metal atoms have been applied for CO₂ reduction already before the emergence of the SAC concept, the new SAC concept has triggered more researches in this field and built a bridge between the heterogeneous and homogeneous catalysis.^{49, 138-140} In view of their atomic dispersion feature and excellent performances, representative examples of immobilized mononuclear complexes were included in this review for discussion. In this section, we will describe the recent achievements in the field of SACs for CO₂ reduction to formic acid/formate, which are categorized to three groups in accordance with the employed supporting materials: (i) Porous organic polymers based SACs; (ii) Metal oxides based SACs; and (iii) MOF based SACs. Table 3 provides an overview on the performances of SACs based on transition metals.

Scheme 5. Proposed structures of POP-based SACs for CO₂ hydrogenation to formic acid/formate

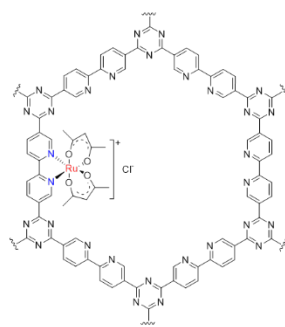
Heterogeneous SACs based on N-containing porous organic polymers



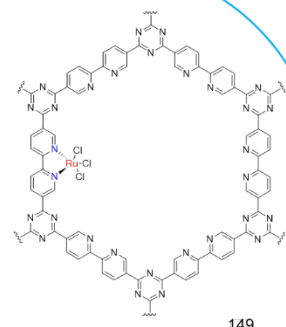
IrCp*@bpy-CTF¹⁴⁷
TOF = 5300 h⁻¹



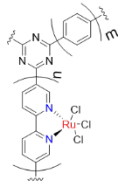
RuC₆Me₆@bpy-CTF¹⁴⁸
TOF = 2640 h⁻¹



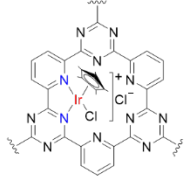
Ruacac@bpy-CTF¹⁴⁸
TOF = 22700 h⁻¹



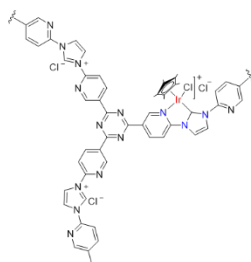
RuCl@bpy-CTF¹⁴⁹
TOF = 38800 h⁻¹



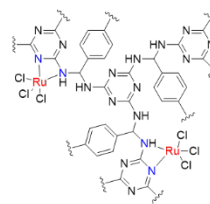
RuCl@TN-bpy-CTF¹⁵⁰
TON = 524000 (720 h)



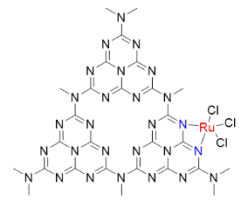
IrCp*@DCP-CTF¹⁵¹
TOF = 3 h⁻¹



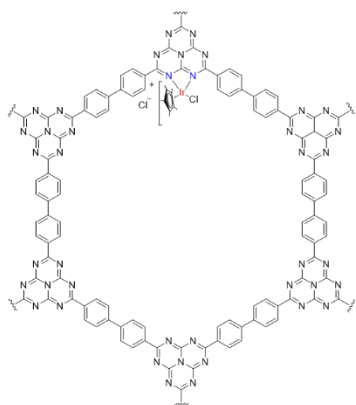
IrCp*@NHC-CTF¹⁵³
TOF = 16000 h⁻¹



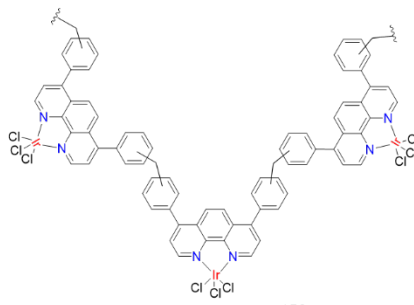
RuCl@MPN¹⁵⁵
TOF = 4964 h⁻¹



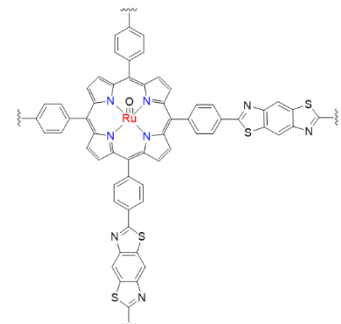
RuCl@g-C₃N₄¹⁵⁵
TOF = 487 h⁻¹



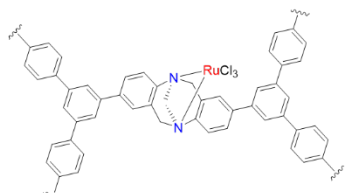
IrCp*@HBF-2¹⁵⁴
TOF = 1500 h⁻¹



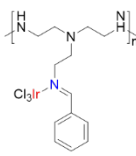
IrCl@phen-POP¹⁵⁶
TOF = 40000 h⁻¹



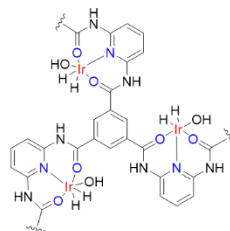
Ru@BBT-POP¹⁵⁸
TOF = 17 h⁻¹



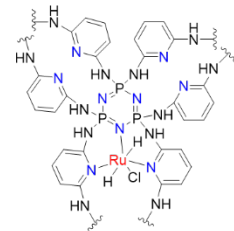
RuCl@TB-MOP¹⁵⁷
TON = 2254 (24 h)



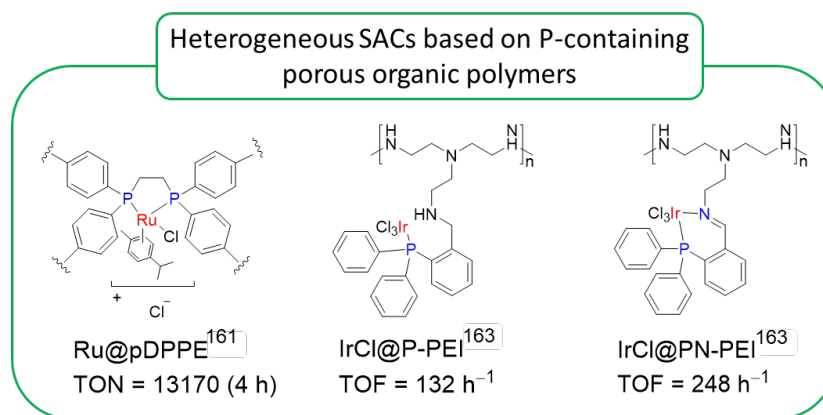
IrCl@N-PEI¹⁶³
TOF = 38 h⁻¹



Ir@AP-POP¹⁵⁹
TON = 25135 (24 h)



Ru@p-dop-POMs¹⁶⁰
TON = 25400 (24 h)



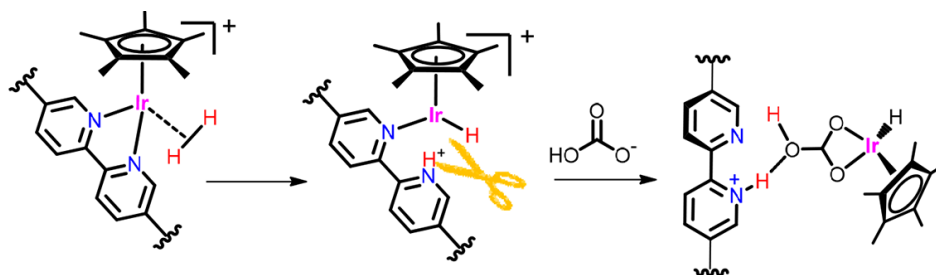
4.1 Porous organic polymer-based SACs

Porous organic polymers (POPs), typically built from diverse organic modules linked by covalent bonds, have emerged as a versatile platform for heterogeneous catalysis. The well-known properties of POPs such as tunable porous structures, large surface areas, good thermal stabilities, and customized functionalities, make them ideal supporting materials for SACs.^{141, 142} Notably, the merits of classical heterogeneous catalysts and molecular metal complexes are merged into POPs, which feature rich binding sites provided by the organic building blocks to hold metal species and easy separation/reuse owing to their insoluble nature.¹⁴³ As a result, well-defined and singly-dispersed active metal sites can be stabilized on POPs, affording POP-based SACs to bridge the material gap between homogeneous and heterogeneous catalysts. Moreover, when employing N-containing organic molecules as building blocks, POPs will be endowed with CO₂-philic properties favoring the adsorption/activation of CO₂,^{144, 145} leading to enhanced performance for CO₂ reduction. Accordingly, N-containing POPs have been intensively explored as supports to synthesize SACs aiming at highly efficient hydrogenation of CO₂ to formate/formic acid.

4.1.1 N-containing POP-supported SACs

As a subclass of POPs, covalent triazine framework (CTF), prepared by the intermolecular trimerization of aromatic nitriles, has attracted much interests in the field of CO₂ adsorption/activation due to its abundant basic functional groups.¹⁴⁶ In addition to triazine moieties, well-known organic ligands like pyridine, bipyridine, and N-heterocyclic carbene (NHC), could be incorporated into CTF by polymerizing the corresponding nitriles. The functionalized CTF has more accessible chelators with enhanced electron-donation abilities, and thus appear as a superior solid ligand to stabilize metal centers (e.g., Ir and Ru) that are catalytically active for CO₂ reduction. In this manner, both basic sites and active metal centers were created on the functionalized CTF, which can potentially enable an integrated process of CO₂ capture and reduction to formate/formic acid.

Scheme 6. Proposed mechanism for the cleavage of Ir–bpy (Ir leaching) induced by the protonation of bipyridine ligands. Reproduced with permission from ref. 148. Copyright 2018, American Chemical Society.



Motivated by the high efficiencies of half-sandwich Ir(Ru)–bipyridine complexes for the homogeneous reduction of CO₂ to formic acid/formate,³³ substantial efforts were devoted to immobilize molecular Ru and Ir species onto bipyridine-based CTF (bpy-CTF) as efficient and recyclable heterogeneous catalysts (Scheme 5). In 2015, Park et al. reported the first immobilization of molecular Ir(III) complex [IrCp*Cl₂]₂ (Cp* = pentamethylcyclopentadienyl) into bpy-CTF by a facile impregnation method (Scheme 5).¹⁴⁷ The synthesized IrCp*@bpy-CTF afforded a high initial TOF of up to 5300 h⁻¹ at 120 °C under 80 bar H₂/CO₂ (1/1) in aqueous NEt₃ solution (Table 3, entry 1), representing the highest activity over heterogeneous catalysts reported at that time. SEM and XPS confirmed the presence of uniformly dispersed Ir(III) species in electron-rich state as a result of the electron-donation nature of bpy ligand, which was proposed as the origin of the excellent performance. Nevertheless, a pronounced deactivation was observed for IrCp*@bpy-CTF with TON decreasing from 5000 to 3000 during five consecutive tests, probably due to the leaching of Ir species into solution, as proven by ICP. In another work, molecular Ru(II) complex ([Ru(C₆Me₆)Cl₂]₂, C₆Me₆ = hexamethylbenzene) was immobilized onto bpy-CTF to generate a heterogeneous Ru catalyst (RuC₆Me₆@bpy-CTF, Scheme 5), which afforded a lower TOF of 2640 h⁻¹ than IrCp*@bpy-CTF under identical reaction conditions.¹⁴⁸ During recycling tests, a gradually decreasing trend in TON was also found on RuC₆Me₆@bpy-CTF (Table 3, entry 2). In a follow-up work by the same group, they conducted a computational study to understand the leaching mechanism of Ir species during the reaction.¹⁴⁸ DFT calculations revealed that the dissociation of Ir–bpy bond was very likely induced by the protonation of bipyridinic moiety resulting from H₂ heterolysis on Ir sites (Scheme 6). Based on these insights, they suggested that the replacement of C₆Me₆ and Cp* by oxyanion ligands like carboxylate and acetylacetonate (acac), capable of capturing the formed proton, can block the proton transfer to the bipyridinic site, and thus improve catalyst recyclability. Following this protocol, an acac-bonded Ru(III) complex immobilized on bpy-CTF (Ruacac@bpy-CTF) was synthesized (Scheme 5).¹⁴⁸ A TOF as high as 22700 h⁻¹ was obtained over Ruacac@bpy-CTF at 120 °C under 80 bar H₂/CO₂ (1/1) in H₂O/NEt₃ (Table 3, entry 3). Compared to the poor stability of RuC₆Me₆@bpy-CTF, Ruacac@bpy-CTF indeed displayed excellent recyclability without loss of activity over four consecutive cycles. These results indicated the key roles of oxygenic ligand like acac in enhancing both the activity and stability of immobilized Ru complex.

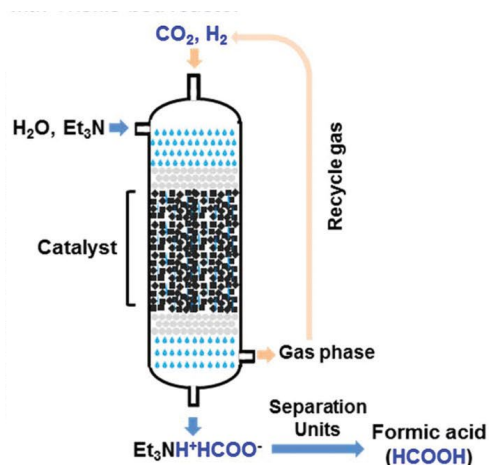


Figure 16. Flow diagram of continuous hydrogenation of CO₂ in a fixed-bed reactor. Reproduced with permission from ref. 150. Copyright 2020, Royal Society of Chemistry.

Several attempts have been made to bring the promising Ru-loaded bpy-CTF catalysts one step close towards industrial applications. Gunasekar and coworkers reported a practically viable heterogeneous Ru SAC by anchoring a simple and air-stable Ru(III) precursor (RuCl₃) into bpy-CTF (Scheme 5).¹⁴⁹ XPS measurements showed that Ru 3d peak was shifted toward lower binding energies by 1.4 eV after immobilization, indicating the successful coordination of RuCl₃ to bpy ligands with the formation of electron-rich Ru centers. The resulted RuCl@bpy-CTF catalyst not only afforded an excellent TOF of 38800 h⁻¹ (Table 3, entry 4), but also maintained its catalytic activities over five consecutive runs. According to XPS, SEM-EDS, and ICP results, the oxidation state and morphologies of Ru centers remained intact and a negligible amount of Ru was leached into the solution after recycling tests, implying the high durability of RuCl@bpy-CTF. Very recently, Park et al. reported the use of terephthalonitrile (TN)-modified bpy-CTF to anchor RuCl₃ as a solid catalyst for the continuous hydrogenation of CO₂ to formate in a fixed-bed reactor (Figure 16).¹⁵⁰ The introduced TN acts as a skeletal linker to improve the porosity and specific surface area of bpy-CTF, making more bpy ligands accessible for anchoring Ru cations (Scheme 5). An isolated Ru configuration by binding to bpy moieties was verified by XPS and EXAFS. The RuCl@TN-bpy-CTF catalyst manifested outstanding stability, giving a total TON of up to 524000 without appreciable deactivation during a long-term (30 days) activity test in a continuous fixed-bed reactor (Table 3, entry 5). Slight Ru leaching and no aggregated Ru particles were detected by ICP and STEM-EDS, respectively. The authors ascribed the superior stability to the generated stable coordination sphere of Ru species with the bipyridinic moieties in TN-bpy-CTF. Such a robust and efficient RuCl@TN-bpy-CTF catalyst demonstrated high feasibility for the practical manufacture of formate from CO₂/H₂. Another study investigated the continuous production of MF with an immobilized Ir(II) complex ([IrCp*Cl₂]₂) on a 2,6-dicyanopyridine-based CTF (IrCp*@DCP-CTF, Scheme 5).¹⁵¹ A promising space time yield of 944.4 mg_{MF} g_{Ir}⁻¹ h⁻¹ (corresponding to a TOF of 3 h⁻¹) was achieved by feeding a mixed gas stream of CO₂/H₂/CH₃OH into a fixed-bed reactor at 180 °C and 300 bar. By means of transient *in situ* DRIFTS at 140 °C and 5 bar CO₂, an intense band at 2334 cm⁻¹ corresponding to the interaction between CO₂ and DCP-CTF was clearly observed, indicating the inherent CO₂ adsorption capability of CTF.

Table 3 Catalytic activities of SACs for the hydrogenation of CO₂ to formic acid/formate

Entry	Catalyst	$p\text{H}_2/p\text{CO}_2$ (bar/bar)	Temp. (°C)	Solvent (v/v)	Additive	Time (h)	TON	TOF (h^{-1}) ^c	Selectivity (%) ^d	ref.
1	IrCp*@bpy-CTF	40/40	120	H ₂ O	NEt ₃	0.25	1300	5300	–	147
2	RuC ₆ Me ₆ @bpy-CTF	40/40	120	H ₂ O	NEt ₃	0.25	–	2640	–	148
3	Ruacac@bpy-CTF	40/40	120	H ₂ O	NEt ₃	0.25	–	22700	–	148
4	RuCl@bpy-CTF	40/40	120	H ₂ O	NEt ₃	0.25	–	38800	100	149
5	RuCl@TN-bpy-CTF	60/60	120	H ₂ O	NEt ₃	720	524000 ^a	–	>99	150
6	IrCp*@NHC-CTF	40/40	120	H ₂ O	NEt ₃	0.25	–	16000	–	153
7	IrCp*@HBF-2	40/40	120	H ₂ O	NEt ₃	0.5	750	1500	–	154
8	RuCl@MPN	40/40	120	H ₂ O	NEt ₃	0.25	1242	4964	100	155
9	RuCl@g-C ₃ N ₄	40/40	120	H ₂ O	NEt ₃	2	975	487	–	155
10	IrCl@phen-POP	40/40	140	H ₂ O	NEt ₃	0.17	–	40000	100	156
11	RuCl@TB-MOP	60/60	40	NEt ₃	PPh ₃	24	2254	–	–	157
12	Ru@BBT-POP	0/1	60	MeCN	Me ₂ PhSiH/KF	4	67	17	–	158
13	Ir@AP-POP	40/40	120	H ₂ O	NEt ₃	24	25135	–	–	159
14	Ru@pDPPE	50/50	120	H ₂ O	K ₂ CO ₃	4	13170	–	–	161
15	IrCl@PN-PEI	20/20	120	H ₂ O	NEt ₃	1	248	248	–	163
16	Ru@NHC-SBA	35/5	85	DMF	DBU	24	18000	–	–	166
17	Ir@PPh ₃ -MSB	25/25	150	DMF	DBU	24	28000	–	–	165
18	IrCl@PN-SBA-15	20/20	120	H ₂ O	NEt ₃	2	2300	1200	–	164
19	IrCl@PN-PEI-TNT-Na	20/20	140	H ₂ O	NaOH	20	1012	–	–	167
20	Ru@LDH	10/10	100	H ₂ O	NaOH	24	698	29	>99	102
21	Ir@bpyOH-UiO-MOF	0.05/0.05	85	H ₂ O	NaHCO ₃	15	6149	410	–	172
22	RuCl@MIL-101 (Cr)-DPPBde	30/30	120	DMSO/H ₂ O (4/1)	NEt ₃ /PPh ₃	2	831	–	–	174
23	RuCp*@NHC-MOF	40/40	120	ethanol	NEt ₃	2	454	–	–	175
24	RuCl@NHC-MOF	40/40	120	ethanol	NEt ₃	2	313	–	–	175
25	RuC ₆ Me ₆ @NHC-MOF	40/40	120	DMF	NEt ₃ /K ₂ CO ₃	2	3803	–	–	175
26	Ru@p-dop-POMs	40/40	120	H ₂ O	NEt ₃	24	25400	–	–	160
27	Pd@bpydc-MOF	40/10	100	ethanol	KOH	24	9816	409	–	176
28	Ru-PNP@UiO-66	12/3	27	DMF	DBU	0.5	320000 ^b	–	–	177

^a a TON obtained for a 30-day continuous operation in a trickle-bed reactor.

b A Rough estimation from the data profile.

c Average TOF within the corresponding reaction time.

d These reported high formate selectivities assumed no detection of other by-products in liquid and gas phase.

For the molecular complexes comprising N-ligands, it is known that their catalytic activities for CO₂ reduction to formate are greatly affected by the electron-donating abilities of N-ligands, that is, a strong electron donor usually leads to high activity.^{33,152} Accordingly, Gunasekar et al. designed the incorporation of a strong electron-donating ligand NHC into CTF (NHC-CTF) as a nitrogen-rich support to immobilize [IrCp*Cl₂]₂.¹⁵³ A bidentate coordination of Ir(III) centers bound to the pyridinic nitrogen and NHC sites was formed (Scheme 5), as confirmed by solid state NMR and XPS. As a result of the electron-donation role of NHC moieties, the immobilized Ir(III) centers possessed much higher electron density than IrCl₃ with a binding energy shift of 0.7 eV, as indicated by XPS. As expected, the IrCp*@NHC-CTF catalyst exhibited an excellent TOF of up to 16000 h⁻¹ (Table 3, entry 6), which was 3-fold higher than that obtained on IrCp*@bpy-CTF under identical conditions. The enhanced catalytic performance resulted from the superior electron-donating ability of NHC to bipyridinic units. However, the leaching of Ir species into solution occurred for IrCp*@NHC-CTF, resulting in unsatisfactory recyclability.

CTF analogues such as melamine- and heptazine-based covalent organic frameworks can also be used to immobilize molecular Ru and Ir complexes. For instance, Hariyanandam and co-workers described the heterogenization of molecular Ir complex ([IrCp*Cl₂]₂) onto heptazine-based framework (HBF-2) synthesized from dicyandiamide and biphenyldicarbonitrile (Scheme 5).¹⁵⁴ The resultant IrCp*@HBF-2 afforded a moderate TOF of 1500 h⁻¹ probably due to the relatively weak electron-donating properties of heptazine moieties (Table 3, entry 7). By comparing the catalytic performances of heterogeneous [IrCp*Cl₂]₂ catalysts containing various solid N-ligands (Table 3, entries 1, 6, and 7), it could be found that their activities increased with the enhanced electron-donating properties of solid N-ligands, that is, IrCp*@HBF-2 < IrCp*@bpy-CTF < IrCp*@NHC-CTF. This is in line with the aforementioned principle in homogeneous catalysis. Jaleel et al. synthesized a melamine-polymer network (MPN) containing secondary amine and triazine groups, which can anchor RuCl₃ as a heterogeneous Ru catalyst (Scheme 5).¹⁵⁵ Ru centers were proposed to exist in bidentate coordination state by binding to the nitrogen atom of the secondary amine and triazine groups on MPN, as indicated by XPS results. A considerably high TOF of 4964 h⁻¹ was obtained on RuCl@MPN at 120 °C under 80 bar H₂/CO₂ (1/1) in H₂O/NEt₃ (Table 3, entry 8). For comparison, an immobilized RuCl₃ catalyst onto g-C₃N₄ (RuCl@g-C₃N₄, Scheme 5) was also examined for CO₂ reduction, giving a much lower TOF of 487 h⁻¹ (Table 3, entry 9). Together with previous results of RuCl@bpy-CTF and RuCl@MPN (Table 3, entries 4 and 8), their activities increased in the order of RuCl@g-C₃N₄ < RuCl@MPN < RuCl@bpy-CTF, consistent with the increasing trend of electron-donating properties of these N-moieties. This finding further confirmed the positive dependence of activity on the electron-donating abilities of solid ligands regardless of ligand type.

Guided by this structure-activity relationship, a number of superior N-containing electron donors such as phenanthroline (phen),¹⁵⁶ Tröger's base (TB),¹⁵⁷ and porphyrin moieties have been incorporated into POPs as promising solid supports to fabricate heterogeneous molecular Ru/Ir catalysts.¹⁵⁸ For example, the group of Yoon prepared a phen-based POP (phen-POP) by Friedel-Crafts cross coupling of phen derivatives with dichloromethane (Scheme 5).¹⁵⁶ The synthesized phen-POP featured high-density bidentate nitrogen ligands (57 wt%) originating from phen, a well-known chelator with excellent coordination ability. As revealed by SEM-EDS and XPS, IrCl₃ was uniformly and singly coordinated to the

nitrogen sites on phen-POP in a bidentate manner. The Ir(III)-loaded phen-POP catalyst (IrCl@phen-POP) showed an impressive TOF of up to 40000 h⁻¹ at 140 °C under 80 bar H₂/CO₂ (1/1) in H₂O/NEt₃ (Table 3, entry 10), outperforming other Ir/Ru-loaded nitrogen-based POP catalysts. In contrast to the severe deactivation usually observed for immobilized Ir catalysts, IrCl@phen-POP displayed satisfactory recyclability with maintained TONs during three successive tests. Once again, the superior activity and stability of IrCl@phen-POP were attributed to the strong electron donating ability of phen moieties leading to robust coordination to Ir species. Yang et al. reported the TB-modified microporous organic polymer-anchored RuCl₃ catalyst (RuCl@TB-MOP, Scheme 5),¹⁵⁷ which possessed additional CO₂ adsorption functions, *viz.* 127 mg g⁻¹ at 1 bar and 0 °C, due to the presence of abundant microporosity and TB moieties. Under mild conditions (40 °C, 60 bar H₂, 60 bar CO₂), RuCl@TB-MOP afforded a high TON of 2254 after 24 h (Table 3, entry 11), but presented inferior stability due to Ru leaching during reaction. Distinct from the widely used post-complexation of metal species onto POPs, a Ru(II) porphyrin-based solid catalyst linked by benzobisthiazole (BBT) was reported by Eder et al., who directly copolymerized the pre-coordinated Ru(II) porphyrin complex with BBT (Scheme 5).¹⁵⁸ The resulting Ru@BBT-POP catalyst showed reasonable activity (TON = 67) towards the catalytic reduction of CO₂ to formate using dimethylphenylsilane as hydride source under 1 bar CO₂ at 60 °C in 4 h (Table 3, entry 12).

4.1.2 Pincer-like POP-supported SACs

Metal centers (Ir, Ru) coordinated by PNP-type pincer ligands represent the highest performance class of molecular complexes for the reduction of CO₂ to formate/formic acid. By mimicking the molecular structure of pincer ligands, the group of Zhang designed a pincer-like POP by the cross coupling of two functional building blocks of diaminopyridine (AP) and benzenetricarbonylchloride (Figure 17A).¹⁵⁹ Active Ir species were incorporated into AP-POP by wet impregnation and subsequent reduction of H₂IrCl₆ in the presence of NaBH₄. The structural properties of Ir-loaded AP-POP catalyst were thoroughly characterized by solid state NMR, XPS, EXAFS, STEM-EDS, which revealed the atomic dispersion of Ir species featuring a tridentate coordination of Ir(III) sites to one pyridinic nitrogen atom and a pair of oxygen atoms of amide groups (Figure 17A), resembling the typical structure of mononuclear Ir–PNP complexes. The Ir@AP-POP catalyst afforded a TON as high as 25135 at 120 °C and 80 bar H₂/CO₂ (1/1) in H₂O/NEt₃ after 24 h (Table 3, entry 13), which was approximately 14 times higher than the supported Ir nanoparticles (ca. 2 nm) on AC (Figure 17B). Evidently, single-atom Ir(III) catalyst was far more intrinsically active than its nanoparticle counterpart. Remarkably, no activity loss occurred during four successive tests (Figure 17C), indicating the robust nature of Ir@AP-POP. Despite surpassing the vast majority of heterogeneous catalysts, the activity of Ir@AP-POP is still far from that of Ir–PNP complexes, probably due to the rather low porosity and surface area of AP-POP (less accessible active sites) as well as the weak electron-donating nature of the amide moieties.

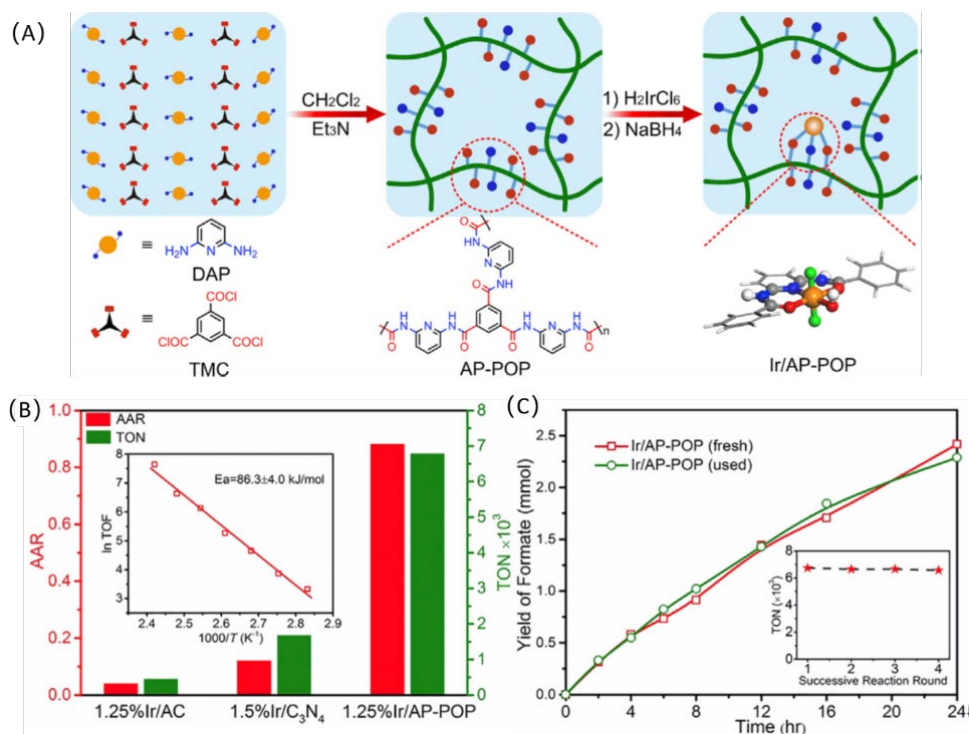


Figure 17. (A) Schematic illustration for the synthesis of single-atom Ir/AP-POP catalyst by copolymerizing 2,6-diaminopyridine (AP) and 1,3,5-benzenetricarbonylchloride. (B) Catalytic performances of different Ir catalysts supported on AC, C₃N₄, and AP-POP. (C) Catalytic performances of Ir/AP-POP for the first two recycling tests and the four successive tests in the Inset. Reproduced with permission from ref. 159. Copyright 2019, Cell Press.

Han and co-workers prepared a pincer-like cyclophosphazene-containing polymer (p-dop-POMs) by the condensation of 2,6-diaminopyridine with phosphonitrilic chloride (Figure 18A).¹⁶⁰ RuCl_3 was subsequently immobilized onto p-dop-POMs by coordinating to triple N sites, i.e., two pyridinic N atoms and one phosphazene N atom, along with two hydride species and one chloride ligand forming an octahedral configuration (Scheme 5), as confirmed by EXAFS (Figure 18B and C). The resultant Ru@p-dop-POMs exhibited a TON up to 25400 at 120 °C and 80 bar H_2/CO_2 (1/1) in $\text{H}_2\text{O}/\text{NEt}_3$ in 24 h (Table 3, entry 26). During three recycling experiments (Figure 18D), the TON was maintained at around 20000 and no change of Ru centers was observed in terms of electronic state and coordinative configuration, indicating the good recyclability of Ru@p-dop-POMs. As a result of the strong electron-donor nature of tridentate N ligands, electron-enriched Ru centers were generated, as evidenced by EXAFS and XPS. According to DFT calculations, the rate-determining step of H_2 heterolysis was facilitated on electron-enriched Ru centers with a low activation barrier of 0.52 eV, which could account for the high activity of Ru@p-dop-POMs.

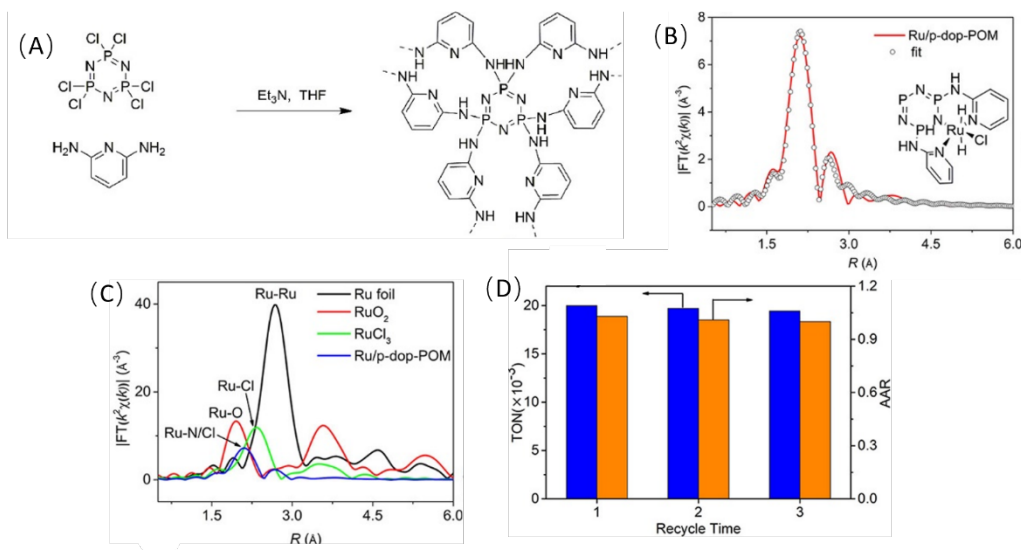


Figure 18. (A) Schematic illustration for the synthesis of a pincer-like polymer by the condensation of 2,6-diaminopyridine with phosphonitrilic chloride. (B) The experimental EXAFS spectra of Ru/p-dop-POM with the fitting results. (C) Fourier transform of k^2 -weighted EXAFS spectra of Ru foil, RuO_2 , RuCl_3 , and Ru@p-dop-POM. (D) Recycling tests of Ru@p-dop-POM for CO_2 reduction to formate at 120°C and 60 bar H_2/CO_2 (1/1) in $\text{H}_2\text{O}/\text{NEt}_3$ for 24 h. Reproduced with permission from ref. 160. Copyright 2020, American Chemical Society.

4.1.3 Phosphine-containing POP-supported SACs

As a well-known *P*-donor ligand, phosphine has been widely employed to construct a large number of metal complexes showing fairly high activities for CO_2 reduction to formate/formic acid.³³ Therefore, there is great interest to build phosphine-based POPs for solid molecular catalysts. For example, the group of Palkovits has designed a polymeric analogue of diphenylphosphine (pDPPE) by the cross coupling of corresponding organic linkers and phosphorus salts.^{161, 162} The obtained phosphine-based pDPPE polymer served as a perfect solid ligand to fabricate heterogeneous molecular Ru(II) catalysts, wherein each Ru(II) center was proposed to coordinate to two *P* donors (Scheme 5). The absence of Ru particles indicated the atomically-dispersed and well-coordinated structures of Ru species on pDPPE. A high TON of up to 13170 was achieved on Ru@pDPPE in 4 h at 120°C and 100 bar CO_2/H_2 (1/1) in aqueous K_2CO_3 solution (Table 3, entry 14). In contrast, AC-supported Ru nanoparticles (Ru/AC) gave quite low activity (TON = 780). Recycling experiments showed a pronounced activity drop in the second run, which was likely due to the ligand exchange of *p*-cymene by CO (a poison for Ru) in the coordination sphere during the reaction, as well as the leaching and sintering of Ru species, as evidenced by solid state NMR, ICP, FTIR and STEM. McNamara et al. investigated the effect of ligand type on the catalytic activity of immobilized Ir(III) catalyst.¹⁶³ Three PEI polymers containing monodentate PPh_3 moieties (P), monodentate imine moieties (N), and bidentate iminophosphine (PN) moieties were synthesized (Scheme 5), respectively. These polymers were metallated with IrCl_3 . Their activities followed an order of $\text{IrCl}@PN\text{-PEI} > \text{IrCl}@P\text{-PEI} > \text{IrCl}@N\text{-PEI}$. The combination of PPh_3 and imine gave the highest TOF (248 h^{-1} , Table 3, entry 15), which was 6-fold higher than that achieved on the sole use of imine moieties ($\text{IrCl}@N\text{-PEI}$, $\text{TOF} = 38\text{ h}^{-1}$). This was believed to result from the superior electron-donation property of PPh_3 over imine groups. In another work of the same group, a similar trend was also observed for various N- and P-moieties immobilized on

mesoporous silica (SBA-15).¹⁶⁴ Once again, these results emphasized the vital role of electron donor groups in facilitating CO₂ reduction to formate.

In summary, POP-based SACs are commonly constructed by the complexation of active Ir/Ru complexes onto the polymerized analogues of organic ligands. Electron-rich metal centers induced by the electron-donating coordination environment is of crucial importance to achieve high catalytic performance. Therefore, typical N- and P-based ligands containing strong electron-donating groups (e.g., bpy, PPh₃, NHC, imine) are frequently utilized as the building units. These ligand-like building units should also comprise reactive groups that allow for cross-coupling reactions such as Friedel–Crafts and organolithium-mediated reactions, or various condensation reactions with the formation of connecting structures like triazine rings, imine bonds, benzothiazole groups, Troger’s base, and amide bonds. By using these polymerization strategies, well-connected porous networks with sufficient surface areas can be built for the immobilization of more accessible active centers.

4.2 Metal oxide-based SACs

Metal oxide-based SACs reported for CO₂ reduction to formate are mostly constructed by a well-developed surface-grafted strategy, that is, the immobilization of metal complexes via a functional linker grafted on the surface of metal oxides.¹³⁶ Conventional silica materials are typically employed as the solid matrixes to graft molecular complexes due to their rich hydroxyl groups and large surface area. By tailoring the organic moieties of the functional linker, it can also serve as chelating sites to anchor active metal species. The application of metal oxide-based SACs in CO₂ reduction to formate/formic acid has been well summarized in a review published by Álvarez in 2017.³⁵ Herein, we will mainly focus on the latest findings on developing novel metal oxide-based SACs.

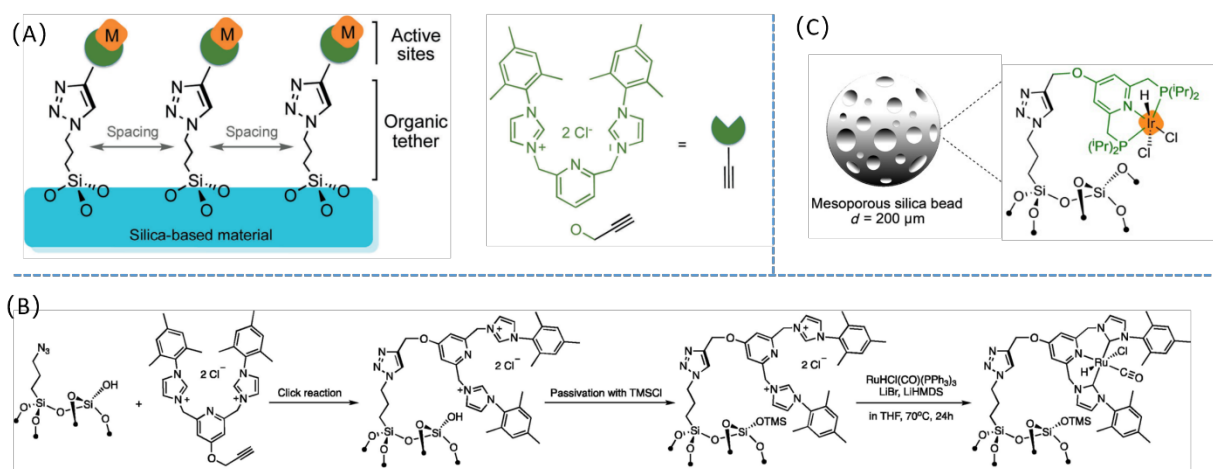


Figure 19. (A) and (B) Synthetic procedures for the immobilized NHC-pincer Ru complex on mesoporous silica by a surface grafting approach. (C) Ir phosphine-pincer molecular catalysts grafted onto the surface of mesoporous silica bead. Reproduced with permission from ref. 165 and 166. Copyright 2019, Wiley-VCH.

Recently, the group of Copéret developed two pincer-type metal complexes grafted on silica with high efficiencies by means of click reaction,^{165, 166} namely, azide-alkyne cycloaddition. As shown in Figure 19A

characterizations revealed that singly dispersed Ru hydroxide species were stabilized on the surface of LDH by anchoring to the triple oxygen atoms from the hydroxyls of LDH as well as one hydroxyl and two water ligands attached to Ru, affording an octahedral coordination sphere (Figure 21C). The resultant Ru@LDH catalyst gave a high TON of 698 within 24 h at 100 °C and 20 bar CO₂/H₂ (1/1) in aqueous NaOH solution (Table 3, entry 20). The catalyst could be recycled three times without significant loss of activity, and neither leaching nor aggregation of Ru species were found. The 3-fold chemical bonding formed between mononuclear Ru species and LDH was claimed to account for the robust nature of Ru@LDH. Meanwhile, such 3-fold hydroxyl ligands could make the Ru centers electron enriched by charge transfer. It was found that the catalytic activities (TONs) of metal oxide-supported Ru catalysts showed liner dependence on their Ru 3p binding energies (Figure 21A), that is, a lower binding energy of Ru (corresponding to electron-rich state) enabled high TON. Accordingly, the electron donor function of hydroxyl ligands on LDH was claimed as the origin of high activity of Ru@LDH, as stated above for many other catalysts. Besides, a positive correlation was achieved between TON and CO₂ adsorption abilities of various types of LDHs (Figure 21B). The highest TON was reached on the optimized LDH with a Mg²⁺/Al³⁺ ratio of 5/1 bearing the maximized basic sites. As a result of the abundant basic sites on LDH, CO₂ could be locally concentrated near Ru centers, thus contributing to the catalytic activity of Ru@LDH. Despite featuring well-defined single-atom Ru sites, Ru@LDH exhibited much lower activity than the immobilized molecular Ru(II) catalysts with PPh₃, bpy and NHC moieties, and also lower than nanostructured Ru catalysts containing amorphous Ru(II) hydroxide or metallic Ru species, as stated above. These results can reasonably suggest that the relatively low activity was very likely due to the high oxidation state of Ru(IV) species on Ru@LDH and the lack of electron-donating function of LDH, as indicated by XANES.

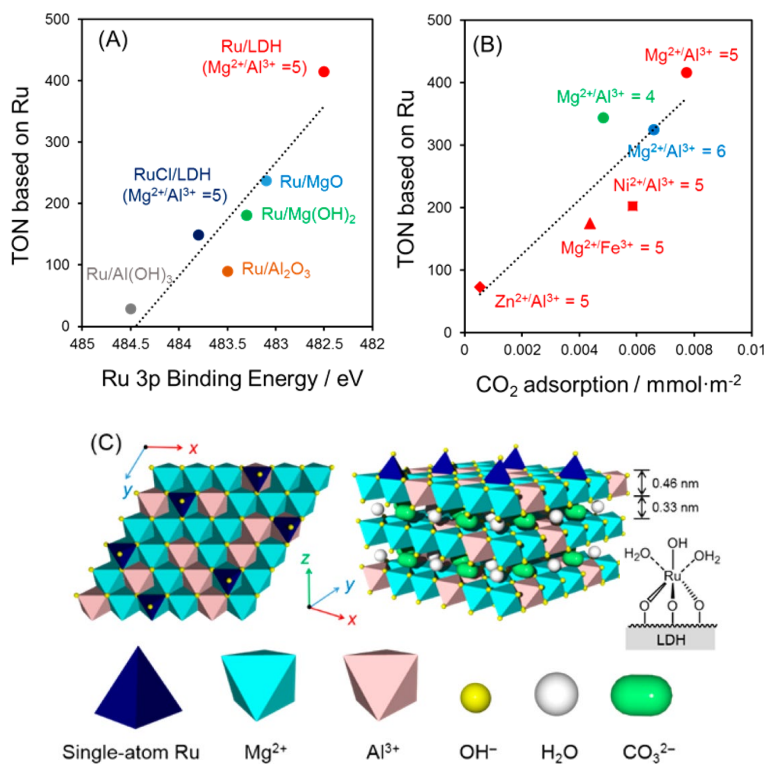


Figure 21. (A) Correlation between the TON and Ru 3p binding energies of different supported Ru catalysts determined by XPS. (B) Correlation between TON and the CO₂ adsorption capacities of different Ru/LDH

catalysts. (C) Structural representation of single-atom Ru hydroxide species anchored on the surface of LDH. Reproduced with permission from ref. 102. Copyright 2017, American Chemical Society.

In summary, almost all metal oxide-supported SACs rely on surface-functionalized silica, which can offer a variety of binding sites with electron-donating function for metal complexation. Therefore, high activities can be achieved with the proper choice of organic groups and corresponding grafting strategies, as well as fine control on the surface functionalization process. Nevertheless, the poor stability is the major issue of SiO₂-supported SACs owing to the intrinsically liable Si–O–Si connectors. There is only one report about the non-functionalized metal oxide-supported SAC prepared by depositing Ru hydroxides onto LDH, a pure inorganic material without organic functionalities. In comparison to SiO₂-supported SACs, Ru@LDH gave better stability but much lower activity. The development of metal oxide-supported SACs is still in its fancy. Future effort should be directed to developing novel synthesis strategies for metal oxide functionalization to break the trade-off between activity and selectivity.

4.3 MOF-based SACs

Metal organic frameworks (MOFs) are a family of organic-inorganic hybrid materials comprising diverse metal clusters and organic linkers, which are combined via coordination bonds in an orderly way. Owing to the abundant and tunable binding sites provided by organic linkers, MOFs have found tremendous applications as supporting materials for building SACs.^{168, 169} In particular, the well-tailored MOFs with a large number of open metal sites and basic moieties (e.g., amine, pyridine, amide) have demonstrated outstanding efficiency for CO₂ adsorption/conversion.^{170, 171} Albeit holding great promise for CO₂-relevant transformations, there have been only a few reports on the application of MOFs for catalytic hydrogenation of CO₂ to formate/formic acid so far. In 2017, the group of Lin et al. designed an efficient Soxhlet-type reflux-condensing process for atmospheric CO₂ reduction catalyzed by a solid molecular Ir(III) catalyst supported on a UiO-type bpy-modified MOF (Figure 22, Scheme 7).¹⁷² The introduced bpy moieties served as anchoring sites to coordinate to mononuclear Ir(III) complexes (IrCl₃). To further enhance the activity of Ir, a hydroxyl moiety was introduced to generate a hydroxyl-substituted bpy ligand (bpyOH). The deprotonated hydroxyl-substituted bpy ligand could function as both an electron donor and a proton reservoir, which has exhibited high efficiency for homogeneous CO₂ reduction to formate.¹⁷³ Indeed, under very mild conditions (85°C, 1 bar H₂/CO₂(1/1), NaHCO₃), the resultant Ir@bpyOH-UiO-MOF catalyst showed an excellent TON of 6149 within 15 h (Table 3, entry 21), which was nearly 15 times higher than its OH-free counterpart. The high TON could be well maintained for three consecutive runs, and no leaching and structural changes was found for the active Ir centers. It was noteworthy that the Ir@bpyOH-UiO-MOF catalyst was transformed to an activated form during the reaction by exchanging chloride ligands in IrCl₃ with H₂O ligands, leading to a significant improvement of the TON by 11-fold. This enhanced activity was attributed to the catalytic role of H₂O ligand in assisting proton transfer to generate formic acid on active Ir centers, as revealed by DFT calculations.

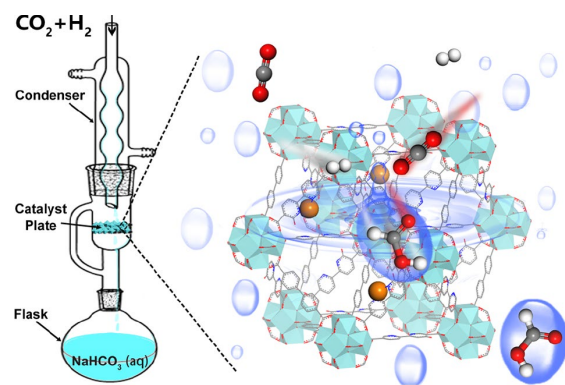
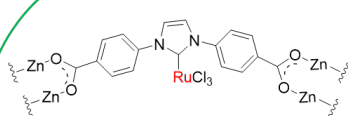


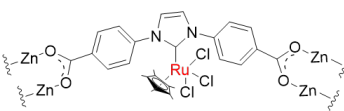
Figure 22. Catalytic reduction of atmospheric CO₂ to formate in a Soxhlet-type reflux-condensing process over a solid molecular Ir(III) catalyst incorporated into a UiO-type bpy-modified MOF (Ir@bpyOH-UiO-MOF). Reproduced with permission from ref. 172. Copyright 2017, American Chemical Society.

Scheme 7. Proposed structures of MOF-based SACs for CO₂ hydrogenation to formic acid/formate.

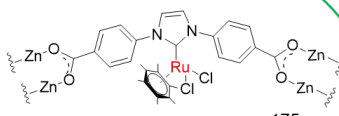
Heterogeneous SACs based on N-containing metal organic frameworks



RuCl@NHC-MOF¹⁷⁵
TON = 313 (2 h)



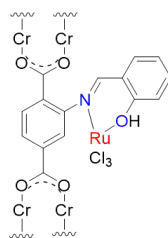
RuCp*@NHC-MOF¹⁷⁵
TON = 454 (2 h)



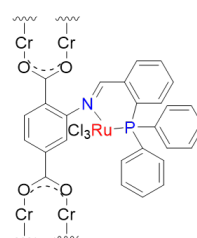
RuC₆Me₆@NHC-MOF¹⁷⁵
TON = 707 (2 h)



RuCl@MIL-101(Cr)-NH₂¹⁷⁴
TON = 198 (2 h)



RuCl@MIL-101(Cr)-Sal¹⁷⁴
TON = 218 (2 h)



RuCl@MIL-101(Cr)-DPPBde¹⁷⁴
TON = 242 (2 h)



Pd@bpydc-MOF¹⁷⁶
TON = 9816 (24 h)



Ir@bpyOH-UiO-MOF¹⁷²
TON = 6149 (15 h)

Most recently, the group of Ma reported the immobilization of Ru complexes onto MIL-101(Cr)-NH₂ as solid molecular Ru catalysts.¹⁷⁴ They incorporated the functional moieties of salicylaldehyde (Sal) and 2-diphenylphosphinobenzaldehyde (DPPBde) into the skeleton of MIL-101(Cr)-NH₂ by condensing with amine groups to generate a Schiff base linkage (Scheme 7). These modified MOFs were metalated with RuCl₃ to give a series of immobilized molecular Ru catalysts: RuCl@MIL-101(Cr)-NH₂, RuCl@MIL-101(Cr)-Sal, and RuCl@MIL-101(Cr)-DPPBde (Scheme 7). Ru(III) species were highly distributed within the matrix of MOFs, as indicated by XRD₂ and TEM. RuCl@MIL-101(Cr)-DPPBde gave the highest activity (TON = 242) at 120 °C within 2 h, followed by RuCl@MIL-101(Cr)-Sal affording a TON of 218, and RuCl@MIL-101(Cr)-NH₂ showed the lowest TON of 198. This activity trend is well consistent with their electron-donating abilities arising from different moieties, that is, monodentate NH₂ < bidentate Sal (hydroxyl, Schiff base) < bidentate DPPBde (PPh₃, Schiff base). Again, these results pointed to the beneficial effects of introducing electron-donating groups. In another work, Wu et al. employed azolium-containing MOFs (NHC-MOFs) as supports to construct immobilized Ru catalysts.¹⁷⁵ Various Ru precursors including RuCl₃, [RuCp*Cl₂]₂, and [Ru(C₆Me₆)Cl₂]₂ were loaded onto NHC-MOF affording RuCl@NHC-MOF, RuCp*@NHC-MOF, and

RuC₆Me₆@NHC-MOF, respectively (Scheme 7). XRD and TEM-EDS characterizations showed an even dispersion of Ru species without the formation of nanoparticles. Among others, RuC₆Me₆@NHC-MOF gave the highest TON of 707, whereas RuCp*⁺@NHC-MOF and RuCl@NHC-MOF exhibited lower activities with TONs of 454 and 313 (Table 3, entries 23 and 24), respectively, under identical conditions (120 °C, 40 bar H₂, 40 bar CO₂, ethanol/NEt₃, 2 h). In contrast to the presence of Ru(III) species in RuCp*⁺@NHC-MOF and RuCl@NHC-MOF, RuC₆Me₆@NHC-MOF possessed lower Ru 3p binding energy corresponding to Ru(II), as revealed by XPS. Accordingly, the superior activity of RuC₆Me₆@NHC-MOF was attributed to the formation of electron-enriched Ru(II) centers resulting from the stronger electron-donation ability of C₆Me₆ than Cp*⁺ and chloride ligands. This is in line with the aforementioned high activities of Ru(II) hydroxide species in nanostructured Ru catalysts. In addition, it was claimed that the utilization of DMF as solvent and adding K₂CO₃ can markedly improve the TON from 707 to 3803 (Table 3, entry 25), yet the underlying reasons are still unclear.

Despite the wide utilization of Pd as the active component for nanocatalysts, only one example of Pd SAC anchored on MOFs has been reported so far. By the solvothermal reaction of 2,2-bipyridine 4,4-dicarboxylic acid (bpydc) with MnCl₂, Tshuma et al. synthesized a MOF containing bpy functional groups, which can coordinate to PdCl₂ to form a Pd@bpydc-MOF SAC (Scheme 7).¹⁷⁶ A high TON of 9816 was obtained over Pd@bpydc-MOF SAC at 100 °C and 50 bar H₂/CO₂ (4/1) in 24 h in the presence of KOH and ethanol (Table 3, entry 27). However, noticeable catalyst deactivation was observed during the stability test of Pd@bpydc-MOF, with the TON decreasing from ~10000 to ~6000 after four recycles. According to TEM and the mercury drop experiment, the aggregation of Pd(II) species to form metallic Pd nanoparticles on the spent catalyst was confirmed. The weak coordinative connection between Pd and bpy groups, as is the case for immobilized Ru/Ir complexes, was proposed as the major reason for the deactivation.

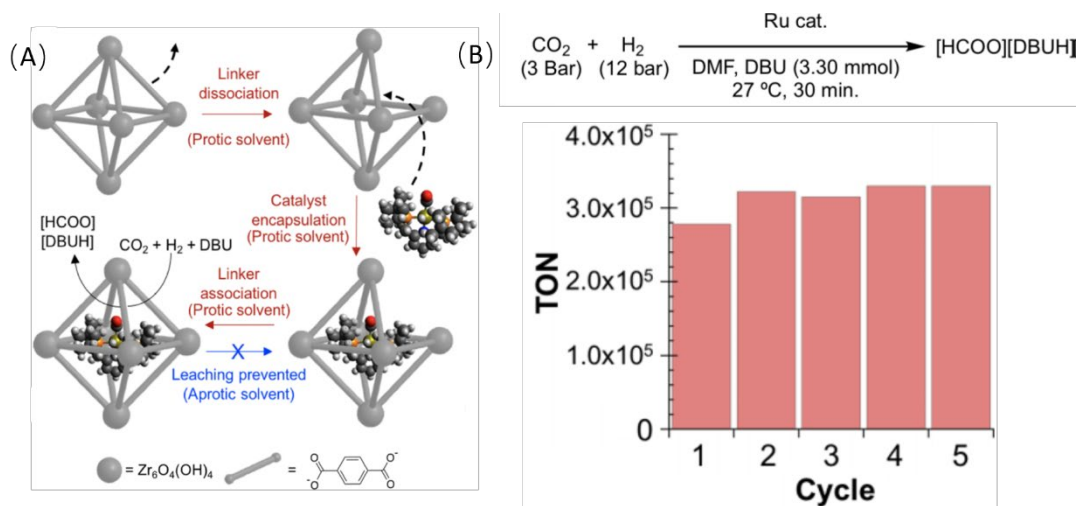


Figure 23. (A) Schematic illustration of the encapsulation of metal complex into the pore space of UiO-66 MOF. (B) Catalytic performance of Ru-PNP@UiO-66 during five recycling tests. Reproduced with permission from ref. 177. Copyright 2018, American Chemical Society.

The direct encapsulation of molecular complexes inside the pore space of MOFs represents another feasible approach to fabricate MOF-based SACs. The key to enable the encapsulation process lies in the use of aperture-opening reaction resulting from the reversible dissociation of linker in the framework of

MOF in protic solvents (Figure 23A). By this novel strategy, the highly-active Ru-PNP pincer complex was successfully encapsulated into the pore space of the UiO-66 MOF.¹⁷⁷ The resultant Ru-PNP@UiO-66 showed an excellent TON up to 320 000 at 27 °C in 30 min in the presence of DBU and DMF (Table 3, entry 28, and Figure 23B), comparable to the Ru-PNP pincer complex. The similar activity indicated that Ru-PNP pincer complex remained intact during the encapsulation process. The prominent advantage of Ru-PNP@UiO-66 is its superior stability and recyclability over the Ru complex, as indicated by the unchanged TONs (around 300000) during five recycling tests and no detectable leaching of Ru complex and UiO-66 (Figure 23B). Thanks to the appropriate size of Ru-PNP complex (smaller than the pore size of UiO-66 but larger than its aperture size), UiO-66 is able to perfectly stabilize and confine each individual Ru-PNP pincer complex in its pore space. Therefore, Ru-PNP@UiO-66 indeed realizes the target of SAC that combines merits of both high activity and good recyclability.

In summary, MOF-based SACs are currently fabricated either by utilizing the functionalized linker to anchor metal complexes or directly encapsulating metal complexes into the cavity of MOF. For the former linker-coordination method, the rational choice of organic linkers comprising functional groups with electron-donating properties is of great importance. For the direct encapsulation method, for a certain topology of MOF, only the molecular complexes with suitable dimensions (as mentioned above) can be successfully encapsulated. When used for catalytic CO₂ reduction, the use of protic solvent and high reaction temperatures should be avoided. These requirements will limit the universality of direct encapsulation method. Both approaches can lead to high activities, but the direct encapsulation method can endow SACs with superior stability to the linker-coordination method, thanks to the pore confinement effects. It should be emphasized that there are still many opportunities for MOF-based SACs, e.g., transforming MOF-anchored metal complex into carbon-supported SAC by pyrolysis as well as encaging single atom alloy nanoclusters inside the pore of MOF. These directions are worthy to be explored in the future design of MOF-based SACs.

5. Mechanistic insights

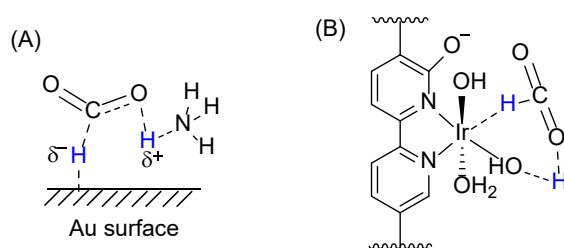
Heterogeneous hydrogenation of CO₂ to formic acid/formate involves a gas-liquid-solid multiphase catalytic system, because of the prevailing employment of gaseous substrates (H₂/CO₂) with a solid catalyst in a liquid medium containing base and solvent. Such a complex reaction network further complicates the catalytic mechanisms associated with H₂ and CO₂ activation/transformation on catalyst surface. As a result, although a variety of heterogeneous catalysts have been developed with satisfactory performances, very few of them have been deeply investigated to achieve a clear, reasonable and complete mechanistic picture. Herein, we will first briefly summarize the relevant insights gained from experimental and theoretical studies with regard to the activation of H₂ and CO₂ on heterogeneous catalysts, and then highlight several well-studied examples of the proposed catalytic cycles.

5.1 H₂/CO₂ activation

Within a typical CO₂ hydrogenation process, H₂ and CO₂ have to diffuse from gas to liquid phase, and finally to the active sites on solid catalysts, wherein H₂ is widely accepted to dissociate into hydride species and proton via a heterolytic process. The role of hydride species is generally believed to fulfil a nucleophilic attack on the electrophilic carbon atom of CO₂ (or adsorbed HCO₃⁻) affording an intermediate of metal-bound formate, as evidenced by theoretical calculations and spectroscopic results.^{106, 126, 178-180} This step is also known as so-called CO₂ insertion into metal-hydride bonds,³³ which is often identified as the rate determining step in the entire catalytic cycle for both homogeneous and heterogeneous catalysts.

Moreover, heterolytic cleavage of H₂ has been proved to be the rate determining step for certain catalyst systems such as Ru@LDH,¹⁰² Ir@PN-PEI-TNT-Na,¹⁶⁷ Ir@AP-POP,¹⁵⁹ and Ruacac@bpy-CTF.¹⁴⁸ Alternatively, H₂ could also undergo a homolytic dissociation on metallic nanoparticles like Ru or Pd with the formation of two hydride species.⁴⁶ However, heterolytic cleavage of H₂ appears to be more feasible for CO₂ reduction to formate due to the favorable kinetics and the presence of bifunctional active sites. In a typical H₂ heterolysis process, hydride species is bonded to Lewis acidic metal center with the proton captured by the Lewis basic moieties,^{46, 181} a mimic of H₂ activation on frustrated Lewis pairs.^{182, 183} As for the reported heterogeneous catalysts, most of them comprised metal centers (e.g., Ru^{δ+}, Ir^{δ+}, Au^{δ+}) with vicinal Lewis basic moieties like amine, pyridine, NHC, Schiff base, and hydroxyl serving as proton acceptor. This bifunctional formulation appears more suitable for the occurrence of H₂ heterolysis rather than homolysis. Moreover, first principle calculations based on Au/NH₃ couples indicated that the attack of hydride and proton species to CO₂ could proceed with low energy barriers through either first hydride then proton transfer (0.4 eV) or concerted hydride and proton transfer (0.24 eV) routes (Scheme 8A).¹⁷⁹ In contrast, the routes involving two hydrides transfers (from H₂ homolysis) possessed much higher energy barriers above 1 eV. Therefore, H₂ dissociation was perceived to proceed preferentially in heterolytic manner. Importantly, the concerted hydride and proton transfer has been recently proved on an immobilized molecular Ir catalyst experimentally.¹⁷² By conducting the reaction with D₂ and/or D₂O, An and co-workers discovered ultra large kinetic isotope effects for Ir@bpyOH-UiO-MOF, which suggested that the RDS of CO₂ reduction to formate involved the concerted hydride and proton transfer (Scheme 8B).

Scheme 8. Concerted hydride and proton transfer on (A) Au/NH₃ couples and (B) Ir@bpyOH-UiO-MOF. (A) Reproduced with permission from ref. 179. Copyright 2017, American Chemical Society. (B) Reproduced with permission from ref. 172. Copyright 2017, American Chemical Society.



As discussed for many catalysts, electron-enriched metal centers were found to be beneficial for catalytic performance. It was suggested that H₂ heterolysis over electron-enriched metal centers can generate metal hydrides bearing more negative charges (described as being more hydridic for transition metal complexes),¹⁸⁴ which can facilitate the nucleophilic reduction of CO₂. This speculation was confirmed by a computational investigation on Au-catalyzed CO₂ hydrogenation.¹⁷⁹ A positive correlation was established between the energy barrier of hydride species attacking the carbon atom in CO₂ and the Bader charge change of hydride species (Figure 24). It could be seen that the adsorbed hydride species (H^{*}) bearing more negative charges showed lower energy barrier indicating higher reactivity towards the nucleophilic attack to CO₂.

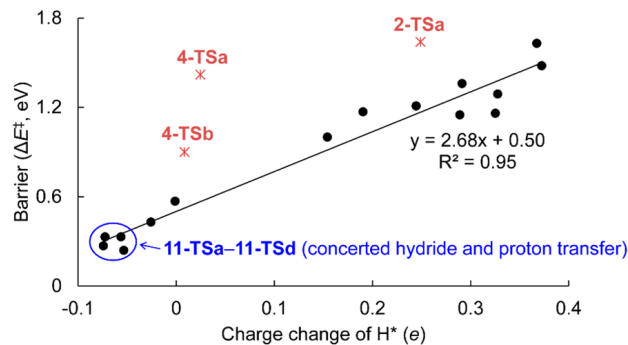


Figure 24. Correlation between the energy barrier of hydride attacking the carbon atom in CO₂ and the charge change of the adsorbed hydride species (H*) on various models of Au surfaces. The charge change refers to the charge difference between the transition state H* and stable state H*. Reproduced with permission from ref. 179. Copyright 2017, American Chemical Society.

In contrast, it is still a debate how CO₂ is transformed on the active site and no consensus has been reached so far. This is mainly due to the diverse CO₂-derived species such as bicarbonate, carbonate, carbamate, and CO₂-tertiary amine adduct involved in the complex reaction system. All of these carboneous species could be involved in the catalytic cycle and thus contribute to the production of formate. To be specific, there exists a common equilibrium of CO₃²⁻/HCO₃⁻/H₂O in aqueous alkaline solution, wherein HCO₃⁻ is widely accepted as the true substrate for CO₂ hydrogenation especially on Pd catalysts.⁴⁴ Opposed to the facile reduction of HCO₃⁻, the direct reduction of CO₃²⁻ to formate appears to be kinetically sluggish due to its high thermodynamic stability.^{185, 186} For instance, when employing NaHCO₃ and KHCO₃ as the carbon source, a commercial Pd/AC catalyst afforded TONs up to 527 and 567 at room temperature in 1 h, respectively, whereas negligible TONs (< 1) were obtained in the presence of Na₂CO₃ and K₂CO₃ as the carbon source.⁷⁶ The similar poor reactivity of CO₃²⁻ was also found for bimetallic PdCo catalysts.¹²⁸ In the case of amine-modified catalysts such as Au/SiO₂-NH₂,⁷² Pd/ECN,⁷⁸ and PdAg-PEI@HMOS,¹²⁴ it has been demonstrated that during the reaction CO₂ can be transformed into carbamate by reacting with primary or secondary amines as revealed by *in situ* DRIFT. Yet, it is unknown whether carbamate could be reduced to formate heterogeneously. So far, there has been no experimental or computational evidence reported to support the proposal of directly hydrogenating carbamate into formate, which is unlikely to occur due to the less electrophilic carbon atom in CO₂ upon the formation of C-N bond. In fact, the inactive nature of methyl carbamate, a simple molecule in carbamate family, has been experimentally proved by Su et al.¹⁸⁶ No formate was produced from the hydrogenation of methyl carbamate at 20 °C and 27.5 bar H₂ over Pd/AC. Most likely, carbamate might indirectly participate in the catalytic cycle via re-decomposition into free CO₂ following a typical CO₂ reduction pathway.¹⁸⁷ When tertiary amines are present as the catalyst promoter (e.g., Schiff base) or as the base additive (e.g., NEt₃, DBU), a weakly bonded CO₂-tertiary amine adduct, also called zwitterion adduct, can be formed.⁷² It should be noted that CO₂ and tertiary amines are not linked by chemical bonds but rather dipole-dipole forces, essentially different from the aforementioned carbamates. Thanks to the weak interactions, CO₂ can be readily released from such labile adducts to undergo hydrogenation. Therefore, despite the formation of CO₂-tertiary amine adduct, the actual substrate involved in the catalytic cycle concerns CO₂ still. In addition, the utilization of tertiary amines as the base could enable higher catalytic activities than primary and secondary amines. For example, in the presence of NEt₃ and 20 bar CO₂, the Au/SiO₂-Schiff catalyst exhibited nearly 4 times higher TONs than that obtained with propylamine and dimethylamine.⁷² In contrast to the stable ionic

carbamate generated between CO₂ and primary/secondary amines, the liable interaction within CO₂-tertiary amine adduct allowed the facile storage/release of CO₂, which could partly account for the enhanced activity with tertiary amines.

Taken together, according to the real form of CO₂ that participates in the catalytic cycle, there are two main reaction mechanisms widely accepted for the heterogeneous hydrogenation of CO₂ to formic acid/formate, namely, bicarbonate and CO₂ reduction pathways. It should be mentioned that in most cases both pathways could simultaneously proceed to different degrees. The predominant reaction pathway for a certain system comes on a case-by-case basis dependent on the employed catalyst, solvent, basic additive, and the basic functionality on catalyst. For example, PEI modified PdAg bimetallic catalyst (PdAg-PEI@HMOS) showed an inferior TOF of 24 h⁻¹ when using NaHCO₃ as the carbon source, whereas the TOF was drastically improved to 153 h⁻¹ with the addition of CO₂ to the same reaction.¹²⁴ As stated above, the activities of Pd-based catalysts are known to be dependent on bicarbonate concentration. Nevertheless, it was found that the TONs of PdAg-PEI@HMOS were independent on bicarbonate concentration. In contrast, the PEI-free PdAg@HMOS catalyst showed the expected TON enhancement with increasing bicarbonate concentration. These results implied that the introduction of PEI (containing amine moieties) to PdAg catalyst shifted the dominating reaction mechanism from bicarbonate pathway to CO₂ reduction pathway via intermediates of carbamate or zwitterion adduct.

5.2 Proposed catalytic cycles

To illustrate the catalytic cycles associated with the two main reaction pathways, several studies manifesting reasonable mechanistic proposals have been chosen as examples here. Notably, the proposed mechanistic cycles for immobilized molecular SACs are essentially similar to their homogeneous counterparts. For a detailed mechanistic discussion of the homogeneous CO₂ reduction to formate, readers are guided to several reviews.^{33, 67, 188, 189}

Filonenko et al. suggested a catalytic cycle for the reduction of CO₂ to formate over Au/Al₂O₃ (Figure 25).¹¹⁷ Within this cycle, CO₂ and its adduct are considered as the real substrates since the reaction was conducted in non-aqueous media containing NEt₃ and DMF. Both DMF and NEt₃ were found to exist on the spent Au/Al₂O₃ catalyst, as evidenced by FTIR. Therefore, the desorption of solvent/base was proposed as the initial step to afford vacant site for H₂ activation. The heterolysis of H₂ on the interface of metallic Au nanoparticles and Al₂O₃ produces Au-hydride species with the concurrent generation of hydroxyl group on Al₂O₃. The formed hydroxyl group was speculated to react with CO₂ giving bicarbonate intermediate according to FTIR results. The formation of bicarbonate intermediate was also detected on metal oxide-supported Pd catalysts.⁹⁴ Subsequently, the nucleophilic attack of hydride to the adjacent bicarbonate species affords an intermediate of Au-bound formate, which is finally desorbed from the Au nanoparticles giving formic acid-NEt₃ adduct.

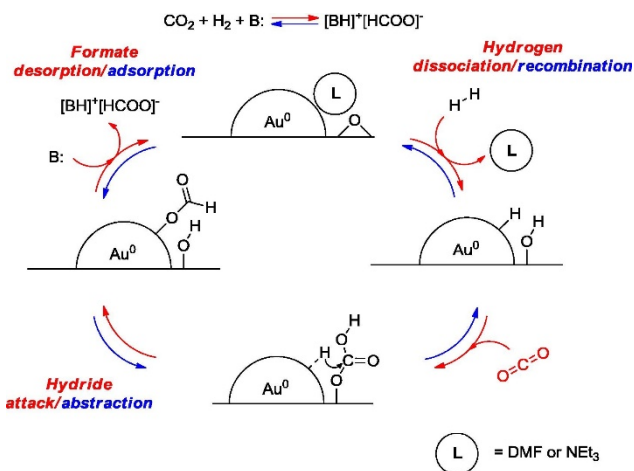


Figure 25. Proposed catalytic cycle for CO_2 hydrogenation to formate in the presence of DMF and NEt_3 over $\text{Au}/\text{Al}_2\text{O}_3$. Reproduced with permission from ref. 117. Copyright 2016, Elsevier.

Mori et al. proposed a bicarbonate pathway for CO_2 hydrogenation to formate in aqueous NaOH solution over bimetallic PdAg/TiO_2 catalyst.¹²² FTIR results showed the characteristic band of bicarbonate (at 1454 cm^{-1}) on PdAg/TiO_2 upon treated with CO_2 and basic aqueous solution. These formate and bicarbonate species were proven to originate from CO_2 by an isotopic experiment using $^{13}\text{CO}_2$ in aqueous NaOH solution (Figure 26). Kinetic investigations revealed the independence of the catalytic performance of PdAg/TiO_2 on CO_2 pressure. These results indicated that bicarbonate was produced as the true substrate in aqueous NaOH solution. The catalytic cycle starts with the dissociative adsorption of H_2 on PdAg nanoparticles to provide Pd -hydride species (step 1 in Figure 26), followed by the adsorption of bicarbonate on PdAg nanoparticles in a bridge manner (step 2 in Figure 26). The subsequent reduction of bicarbonate by hydride likely proceeds via the nucleophilic attack at the carbon atom in bicarbonate (step 3 in Figure 26), which was verified to be energetically favourable by DFT calculations. Finally, formate is formed by a dehydration step, which simultaneously recovers the active Pd sites (step 4 in Figure 26). Within this cycle, the nucleophilic attack to bicarbonate was identified as the RDS based on the kinetic results. Note that the whole catalytic cycle on PdAg/TiO_2 catalyst was suggested to proceed merely on metal nanoparticles without the participation of TiO_2 support. This is distinct from the aforementioned reaction mechanism on $\text{Au}/\text{Al}_2\text{O}_3$ catalyst, which was believed to take place principally on the interface of the Au domains and Al_2O_3 .

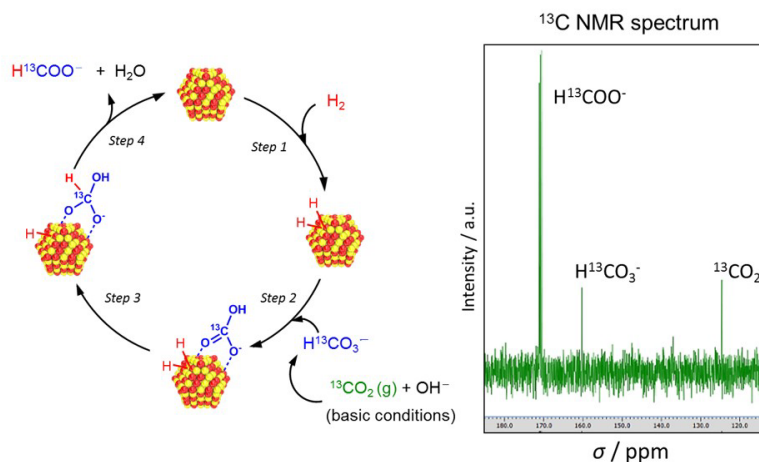


Figure 26. Proposed catalytic cycle and ^{13}C NMR spectrum for $^{13}\text{CO}_2$ hydrogenation to formate in aqueous NaOH solution (D_2O) over bimetallic PdAg/TiO₂ catalyst. Reproduced with permission from ref. 122. Copyright 2018, American Chemical Society.

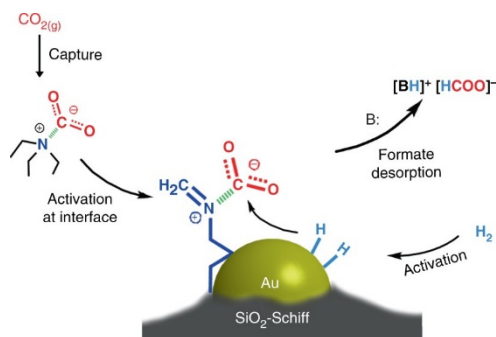


Figure 27. Proposed reaction mechanism for CO_2 hydrogenation to formate over Au/SiO₂-Schiff in the presence of NEt_3 . Reproduced with permission from Ref. 72. Copyright 2017, Springer Nature.

As discussed previously, the hydrogenation of CO_2 over Au/SiO₂-Schiff mainly proceeds through CO_2 route rather than bicarbonate route via the intermediate of CO_2 -tertiary amine adduct. Based on this discovery, Liu and co-workers proposed a catalytic process for CO_2 hydrogenation to formate catalyzed by Au/SiO₂-Schiff catalyst.⁷² As shown in Figure 27, gaseous CO_2 is captured by NEt_3 as zwitterion adducts in methanol/water and then diffuses to the interface of Au nanoparticles and Schiff base moieties, generating new zwitterion adducts with Schiff base moieties. Meanwhile, the dissociative adsorption of H_2 occurs on the low-coordination Au atoms of Au nanoparticles, resulting in Au-hydride species. The CO_2 -Schiff base adduct is then reduced to Au-bound formate species by the adjacent hydride species via the nucleophilic attack to the carbon atom in CO_2 , which serves as the RDS because of the highest theoretical energy barrier of 1 eV. By a proton transfer process, the formic acid is finally formed and desorbed from Au surface.

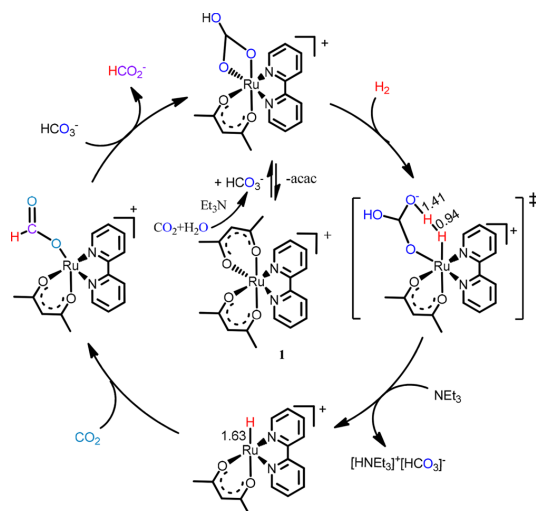


Figure 28. Proposed catalytic cycle for CO₂ hydrogenation to formate over heterogeneous Ruacac@bpy-CTF catalyst in aqueous NEt₃ solution. Reproduced with permission from Ref. 148. Copyright 2018, American Chemical Society.

A bicarbonate-assisted reaction mechanism of CO₂ reduction to formate over heterogeneous Ruacac@bpy-CTF catalyst was proposed by Gunasekar et al.¹⁴⁸ By comparing the XPS spectra of fresh and spent catalysts, it was found that the coordination environment of Ru(III) was changed by the partial substitution of acac ligand by bicarbonate species. Accordingly, the Ruacac@bpy-CTF catalyst was speculated to firstly undergo an activation process to form bicarbonate-ligated Ru complex as the true active center. DFT calculations suggested that the catalytic cycle is initiated by the formation of a vacant site on Ru for H₂ adsorption by cleaving one Ru–O bond between Ru and bicarbonate (Figure 28). A Ru–hydride species is then produced by bicarbonate-assisted H₂ heterolysis along with the capture of proton by bicarbonate via a six-membered ring transition state. This is followed by the desorption of bicarbonate ligand with the help of NEt₃. Subsequently, the insertion of CO₂ into Ru–hydride produces an intermediate of Ru-bound formate, which is extracted as the final product accompanied by the re-adsorption of bicarbonate to regenerate the active Ru center.

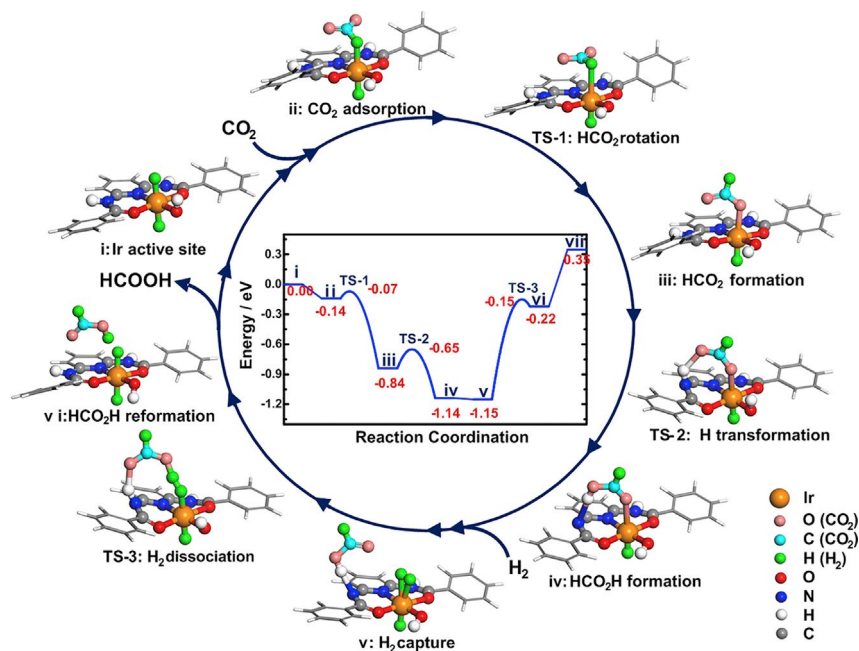


Figure 29. Proposed catalytic cycle for CO₂ hydrogenation to formate over Ir@AP-POP catalyst. Reproduced with permission from ref. 159. Copyright 2019, Cell Press.

Based on DFT calculations, Shao et al. mapped out a possible catalytic cycle for CO₂ hydrogenation to formate over heterogeneous Ir@AP-POP catalyst.¹⁵⁹ As described previously, the freshly synthesized pincer-like Ir@AP-POP catalyst contains chloride-ligated Ir(III) complex, wherein chloride ligands are replaced by hydride species during reaction as evidenced by XPS and EXAFS. Thus, the actual configuration of Ir@AP-POP taking part in the catalytic process comprises two hydride species and one hydroxyl ligand bonded to Ir center. As such, the *in situ* substitution of chloride ligand by other species (mostly hydride) is a common phenomenon for immobilized molecular catalysts, also occurring for Ru@pDPPE,¹⁶² RuCl@bpy-CTF,¹⁴⁹ and IrCl@PN-PEI-TNT-Na.¹⁶⁷ The catalytic cycle starts with CO₂ adsorption onto Ir–hydride to trigger the nucleophilic attack of hydride to the carbon atom in CO₂ (see i to ii in Figure 29). The adsorbed CO₂ is then readily transformed into the Ir-bound formate intermediate via a rotation step with a low energy barrier of 0.07 eV (ii to iii in Figure 29). Interestingly, by bonding to the neighboring acidic H from amide moiety, the formate intermediate is readily reduced into formic acid, which remain bonded to the Ir center and amide moiety (iii to iv in Figure 29). Assisted by the adsorbed formic acid, the subsequent heterolysis of H₂ regenerates the Ir–hydride species along with a proton transfer to enable the liberation of formic acid (v to vi in Figure 29). Meanwhile, the cleavage of O–H bond between the adsorbed formic acid and amide moiety recovers the acidic H in the amide moiety. Within this mechanistic cycle, the heterolytic dissociation of H₂ with the highest energy barrier of 1 eV constitutes the RDS. It should be noticed that amine moieties adjacent to Ir on the solid ligand also play catalytic roles in the catalytic cycle. Although nominally known as single atom Ir catalyst, the essential active center on Ir@AP-POP is comprised of a group of active atoms, analogous to the aforementioned interfacial atom centers on nanocatalysts.

The aforementioned catalytic cycles clearly indicate the essential role of H₂ activation/dissociation to form active metal–hydride species for all catalyst systems, whereas CO₂ can either first undergo an activation step on adjacent basic sites or a direct insertion into metal–hydride species without pre-activation. In

comparison, the electrochemical reduction of CO₂ to formate is believed to proceed primarily by the initial adsorption of CO₂ bound to active sites, followed by protonation and two-electron transfer steps.^{56, 190, 191} By a concerted or step-wise proton/electron transfer, CO₂ could be transformed either to an oxygen-bound intermediate OCHO*, a precursor to formate, or to a carboxyl intermediate (COOH⁻) leading to the formation of CO as a side product.¹⁹²⁻¹⁹⁴ The applied external electricity and electrolyte (e.g., aqueous bicarbonate solution) act as the electron and proton sources, respectively, thus circumventing the utilization of high H₂ pressure. Obviously, the electrochemical CO₂ reduction to formate is mechanistically distinct from CO₂ thermocatalytic reduction, since electrochemical CO₂ reduction is principally fulfilled by protons and electrons rather than by metal-hydride species from H₂ activation. Note that tailored active centers with appropriate adsorption strength for the intermediates of thermocatalytic reduction (e.g., formate, bicarbonate), thus ensuring smooth activation/desorption of formates to avoid the occurrence of resting state, is the key factor for successful thermocatalytic cycles. Similarly, in order to inhibit the severe side-reactions of hydrogen evolution reaction and CO formation via the carboxyl route, tailored electrodes (e.g., Sn) featuring favorable adsorption towards formate (HCOO*) intermediates over carboxyl species (COOH⁻) are indispensable.^{190, 195}

6. Comparison of SACs with nanostructured catalysts

According to the numerous examples in Tables 2 and 3, one can see that both singly dispersed and nanostructured metal species can catalyze the reduction of CO₂ to formic acid/formate with medium to high activities (TONs/TOFs), dependent on the employed metal components, supporting matrixes, and reaction conditions. The optimization of these three parameters constitutes the main subject of most researches in the literature. Very few researches have rigorously studied the catalytic behaviors of SACs and their nanoparticle counterparts under similar experimental conditions, thus making the comparison of SACs with nanostructured catalysts inherently difficult. Here, we will try to showcase the distinct performances of SACs and their nanoparticle counterparts in terms of activity, selectivity, and stability.

As a result of the merits of higher atom utilization efficiency and finely-tuned microenvironments related to active sites, SACs are anticipated to possess higher activities than their nanostructured counterparts. Indeed, this holds true for some SACs in the hydrogenation of CO₂ to formate. For example, Ir@AP-POP,¹⁵⁹ Ru/pDPPE,¹⁶¹ and Ru@p-dop-POMs¹⁶⁰ SACs were reported to show far superior TONs (more than 7 times) than the reference Ir/AC and Ru/AC nano-catalysts under identical reaction conditions. Nevertheless, it should be noted that the different properties of supports, i.e., the basicity of AP-POP, p-dop-POMs, and pDPPE vs. the relatively inert nature of AC, may also contribute to the observed activity enhancements. Accordingly, for a fair comparison of SAC with its nanostructured counterpart, it is highly demanded to fabricate a series of catalysts ranging from nanoscale to single atom on the same support. As such, a rigorous assessment of metal size effect can be realized. Unfortunately, the underlying reason of the activity discrepancy was not studied in these studies. Considering that metal species in different sizes could exist in either oxidized or reduced states, one possible explanation is the distinct H₂ dissociation mechanism, which can determine the overall reaction rate. That is, H₂ usually follows a homolytic cleavage on metallic nanoparticles, whereas the heterolysis of H₂ could occur on SACs involving cationic metal centers, as stressed above.

Table 4 Overview of the size-dependent activity observed for CO₂ reduction to formate over Pd and Au catalysts.

Catalysts ^a	TONs/TOFs at different sizes of Pd/Au		
	single atom	cluster & nanoparticle	large nanoparticle
Au/SiO ₂ -Schiff (TON)	no activity	9278 (1 nm)	2997 (2.8 nm)
Pd/BCN (TOF/h ⁻¹)	~0.6	~1.2 (1.9 nm)	-
Pd/g-C ₃ N ₄ (TOF/h ⁻¹)	-	1.5 (3.4 nm)	0.4 (7.2 nm)

a These data were selected from ref. 119 (Au/SiO₂-Schiff), ref. 78 (Pd/BCN), and ref. 80 (Pd/g-C₃N₄).

For Pd- and Au-based catalysts, an opposite finding was reported that both singly-dispersed Pd and Au species are inferior to their nanostructured counterparts. For instance, a high TON of 9278 (within 7 h) was reached over Au nanoclusters (1 nm) dispersed on SiO₂-Schiff, whereas no product was formed over SiO₂-Schiff-supported single Au atoms, as shown in Table 4.¹¹⁹ This is probably related to the size-dependent electronic properties of Au. To be specific, the electron-donation function of Schiff base favors the formation of electron-rich Au species at the nanoscale, thus facilitating the dissociation of H₂ to form highly-reactive hydride species. By contrast, single Au atoms are speculated to exist in positively-charged states, which is unfavorable for the generation of hydride species. As stressed above, the intrinsic capability of active metal sites to form high-reactivity hydride species, the so-called hydricity,¹⁸⁴ was identified as a crucial indicator of catalyst performance. Over the electron-rich Au nanoclusters, hydride species are readily formed and characterized by being more hydridic, thus leading to high catalytic performance. In the case of Pd/BCN, Pd nanoparticles (1.9 nm) afforded two-fold higher activity than the singly-dispersed Pd atoms (Table 4).⁷⁸ The reduced activity when downsizing to the single atom scale was attributed to the formation of less interfacial sites between single Pd atoms and edge defects (CO₂ activation sites). Nevertheless, Zhang et al. recently reported that the Pd/ZrO₂ SAC were inferior to the nano-sized Pd/ZrO₂ featuring only metallic Pd species.⁹³ The positively charged nature of single Pd atoms on ZrO₂, as indicated by CO-DRIFTS, was believed to account for the low activity of Pd SAC. Further investigations are necessary to unravel the key factor relevant for the size-dependent activity of Pd.

Another advantage of SACs lies in the excellent selectivity towards formate, which was discovered for Ru@pDPPE SAC.¹⁶¹ Interestingly, no CO (side product) was formed on Ru@pDPPE containing only singly-dispersed Ru species, whereas an appreciable concentration of CO (267 ppm) was detected on nanostructured Ru/AC. The formation of CO probably originates from the further dehydration of accumulated formate. It was found that Ru/AC could promote the dehydration of formate to form CO and H₂O, while the dehydration reaction was significantly suppressed over Ru@pDPPE SAC.¹⁹⁶ This is probably related to the distinct geometric and electronic properties of single Ru atoms, thus disfavoring the adsorption of the intermediates for formate dehydration. Yet, the structure-activity relationship behind the inhibited formation of CO on Ru SACs remains to be clarified.

Benefiting from metal-support interactions, nanostructured catalysts containing Pd and Ru nanoparticles are superior to their single-atom counterparts in terms of stability. It has been demonstrated that a range of Pd- and Ru-based nanocatalysts such as Pd/r-GO,⁹⁰ Pd/AC,⁷⁵ Pd/g-C₃N₄,⁸⁰ Pd/ZnO,⁹⁴ PdAg-PEI@HMOS,¹²⁴ PdMn_{0.6}@S-1,¹³⁰ Ru/HT,¹⁰³ and Ru/TiO₂¹⁹⁷ can be isolated and recycled for a couple of times in a batch reactor with nearly unchanged TONs/TOFs. In contrast, fast deactivation is frequently

encountered for the reported Ru and Ir SACs immobilized onto bpy-CTF,^{147, 148} as well as Pd SACs stabilized in bpy-containing MOF.¹⁷⁶ Such poor stability is primarily caused by the labile connection of metal center with the N-containing solid ligands. Under H₂ atmosphere, the formed proton can promote the cleavage of metal–N coordination bonds, thus leading to the leaching and aggregation of metal species. Likewise, single Ru atoms evolution to nanoparticles during recycling tests was observed for Ru@pDPPE featuring Ru–P coordination bonds.¹⁶¹ Yet, the dissociation mechanism of Ru–P bonds remains unclear. Effective solutions have been proposed to address the deactivation issue of SACs. For example, the recyclability of Ru and Ir SACs on bpy-CTF can be enhanced by selecting appropriate Ru/Ir precursors containing acac or chloride ligands instead of Cp* and C₆Me₆ ligands.¹⁴⁸ Besides, the employment of polymerized multidentate ligands, such as AP-POP involving triple chelating sites enabling robust coordination into metal center, can endow Ir@AP-POP SAC with superior stability.¹⁵⁹

7. Conclusion and outlook

High-performance heterogeneous catalysts are key to the catalytic valorization of CO₂ towards the efficient synthesis of valuable formate/formic acid, which can serve as both chemicals and fuels. Driven by the advancements in the field of nanocatalysis and single-atom catalysis, the past few years have witnessed strongly growing efforts devoted to heterogeneous reduction of CO₂ to formate/formic acid. In this context, we summarized recent developments on designing heterogeneous catalysts ranging from nanoscale to atomic scale in this review. Typically, nanostructured metal catalysts involve noble metals such as Pd, Ru and Au as H₂ activation sites along with basic supporting materials offering CO₂ adsorption/activation sites. The interface between metal and basic sites was proposed as the true catalytically active centers, wherein activated H₂ and CO₂ combine to ultimately generate formate/formic acid. Tailoring the basic properties of supports to realize high dispersion of metal species along with maximal interfacial sites has been the main subject of research today on nanocatalysts. Among others, Pd catalysts show superior activity, specifically towards the reduction of bicarbonate to formate even at room temperature without gaseous CO₂. Excellent performances with TONs up to tens of thousands can be obtained on Au and Ru nanocatalysts for the reaction implemented with gaseous CO₂ and NEt₃.

While a rich body of SACs have been reported for various CO₂-related catalytic transformations, the design of SACs with tailored active sites for CO₂ reduction to formate/formic acid is still in its primary stage. Inspired by the high efficiency of homogeneous metal complexes, SACs are often designed by the immobilization and heterogenization of molecular Ir and Ru complexes onto polymeric analogues of organic ligands as well as MOFs. Electron-donating functional groups comprising N, O, and P moieties have been intensively used as building units to construct solid ligands aimed at enhanced electron density at metal centers. The immobilized electron-rich single metal sites usually deliver high TONs/TOFs, but most of them suffer from unsatisfactory recyclability. A potential approach to fabricate stable SACs is the structural engineering of POPs and MOFs, whereby a large amount of organic groups with diverse functionalities can be incorporated. Accordingly, the resultant POPs and MOFs are endowed with various stabilizing effects such as covalent bonds, hydrogen bonds, and electrostatic interactions. By such multiple interactions, single metal atoms are expected to be firmly captured. On the other hand, currently reported SACs are mainly limited to N-coordinated metal complexes. Only few studies are focused on the immobilization of P-coordinated metal complexes. Nevertheless, P-containing molecular catalysts, e.g., PNP pincer complexes possessing state-of-the-art performances among homogeneous catalysts, are far

more active than N-coordinated SACs. Therefore, the design of novel PNP-ligand-based polymers as superior SACs represents a promising direction to be explored. Given the extremely reactive/sensitive nature of PNP ligands, conceiving an applicable synthetic protocol to realize the polymeric network of PNP is of vital importance.

We also stressed the fundamental insights associated with these nanostructured and SACs, which can provide useful guidance for rational catalyst design. Based on the available structure-activity relationships as well as mechanistic understandings, following points are suggested for successful design and construction of heterogeneous catalysts for CO₂ reduction to formate/formic acid: (1) tailoring support materials with appropriate basic properties to promote CO₂ enrichment/activation and enhance the electron density at metal center; (2) downsizing the metal nanoparticles with more active atoms exposed to substrates; (3) ensuring close proximity between metal and basic sites for an efficient synergic catalysis; (4) well-connected porous structures with big pore sizes for better accessibility of metal and basic sites, considering that CO₂ could be transported to active sites in the form of bulky CO₂-amine adduct; and (5) appropriate reduction pretreatment to activate immobilized SACs. It is worthwhile to notice that a highly efficient catalytic process is not only related to the proper catalyst design, but it is also determined by the applied reaction parameters (e.g., temperature, pressure, stirring speed, and reactor type) and mass transfer across gas-liquid and liquid-solid interphases, which need to be verified and well optimized for a given catalytic system.

Despite the significant achievements in formulating and structuring heterogeneous catalysts, further research efforts are required to address the following issues associated with fundamental research and future applications. First, most research overlooked the possible formation of side products like CO, CH₄, methanol, which always need to be strictly controlled when applying heterogeneous CO₂ hydrogenation systems for H₂ fuel purpose. Especially for CO, it could poison the active center even at the low ppm level. Thus, a highly selective catalyst with the exclusive production of formate/formic acid is required in terms of practical viability. SACs hold great promise to meet such selectivity requirement. Especially for SACs utilizing POPs and MOFs as scaffolds, their unique molecular designability can enable high homogeneity and uniformity of the active centers in terms of both coordination environments and electronic properties. Ideally, only target reactions can happen over such specifically designed one-type active sites, thus suppressing side reactions like CO formation. Towards this goal, advanced synthetic methods which can realize the precise construction of single-atom active sites by atomically manipulating each building unit are highly desired. Second, the synergetic catalysis of basic sites and metal sites on catalysts as well as the transformations of CO₂ in amine-containing reaction system need to be understood in detail in order to further optimize catalytic performance. The available mechanistic results are usually obtained by *in situ* FTIR or DRIFT in gas phase without considering solvent environment. Such measurements may be different from the realistic catalytic cycles, in which solvent is involved. In this regard, *in situ* liquid-phase techniques such as *in situ* ATR-IR with solvent under pressure and temperature would be a powerful tool for studying reaction mechanism realistically. Third, as stated above, size-dependent performances were observed for many SACs and nanocatalysts. However, there is a lack of fundamental insights into the general structure-property-activity relationships on different types of metal species with their sizes ranging from nanoscale to single atom. A deep understanding of such structure-property-activity relationships will drive the catalyst development transition from empirical approaches by enormous trial-and-error tests to really knowledge-guided rational design. Therefore, it is imperative to conduct unambiguous structural and electronic determinations of catalytically active centers by *in situ/operando*

characterizations along with accurate theoretical calculations. Fourth, noble metals are currently intensively used as active components for both SACs and nanostructured catalysts. Developing cost-effective non-noble metal catalysts with comparable catalytic performance are highly desirable in terms of economic viability. However, the inherently weak H₂ adsorption/activation abilities of non-noble metals pose a major challenge for efficient CO₂ reduction. More research efforts should be directed to understanding the factors that affect H₂ adsorption/activation on non-noble metal sites, and developing effective synthetic methods applicable to tuning the microenvironments of the non-noble metal sites for enhanced H₂ dissociation abilities. Also the complexity and cost of the catalyst itself, to ultimately foresee large scale workable material, is a concern. In this regard, SACs appear more promising than nanoparticles, as the inherent high metal utilization efficiency would further reduce the catalyst cost. Last but not least, an efficient and also durable heterogeneous catalyst is urgently needed from the viewpoint of practical implementation. Therefore, it is essential to understand and resolve the fast activation of highly-active metal components with ultra-small size during the recyclability test, which is particularly pronounced for Au nanoclusters and immobilized molecular catalysts. Of great relevance is the real-time monitoring of the dynamic evolutions of molecular catalysts under reaction conditions, which can provide valuable information regarding the reaction progress and deactivation mechanism. With continuously increasing interests from academia and industry, we are convinced that adequate solutions will be finally worked out for these problems by the interdisciplinary collaborations across catalysis, material synthesis, computational modeling, and advanced characterization.

Glossary

Carbon capture and utilization	CCU
Single atom catalysts	SACs
Turnover frequency	TOF
Turnover number	TON
Activated carbon	AC
Bulk carbon nitride	BCN
Thermal exfoliation of BCN	ECN
Graphitic carbon nitride	g-C ₃ N ₄
Metal organic frameworks	MOFs
Porous organic polymers	POPs
Covalent triazine framework	CTF
Nitrogen-doped mesoporous carbon	NMC
Mesoporous carbon	MC

Reduced graphite oxide	r-GO
Triphenylphosphine	PPh ₃
1,8-diazabicyclo[5.4.0]undec-7-ene	DBU
Methyl formate	MF
Carbon nanotube-graphene	CNT-GR
Carbon nanotube	CNT
Monoclinic ZrO ₂	ZrO ₂ -M
Tetragonal ZrO ₂	ZrO ₂ -T
Hybrid ZrO ₂	ZrO ₂ -M&T
Interfacially cross-linked reverse micelles	ICRM
Hydrotalcite	HT
4-tert-butylbenzenethiol	TBBT
Hollow mesoporous organosilica sphere	HMOS
Polyethyleneimine	PEI
Mesoporous silica nanosphere	MSN
Zeolitic imidazolate framework	ZIF-8
Reverse water gas shift	RWGS
Hexamethylbenzene	C ₆ Me ₆
Pentamethylcyclopentadienyl	Cp*
Acetylacetonate	acac
Bipyridine	bpy
Terephthalonitrile	TN
N heterocyclic carbene	NHC
Heptazine-based framework	HBF
Melamine-polymer network	MPN
Phenanthroline	phen
Tröger's base	TB
Benzobisthiazole	BBT

Microporous organic polymer	MOP
Diaminopyridine	AP
Polymeric analogue of diphenylphosphine	pDPPE
Mesoporous silica beads	MSB
Titanate nanotubes	TNTs
Iminophosphine	PN
Layered double hydroxides	LDHs
Hydroxyl-substituted bpy moiety	bpyOH
2,6-dicyanopyridine-based CTF	DCP-CTF
Salicylaldehyde	Sal
2-diphenylphosphinobenzaldehyde	DPPBde
Density-functional theory	DFT
X-ray photoelectron spectroscopy	XPS
Diffuse reflectance infrared fourier transform spectroscopy	DRIFTS
Fourier-transform infrared spectroscopy	FTIR
Scanning transmission electron microscopy and energy dispersive spectroscopy mapping	STEM-EDS
Scanning electron microscopy	SEM
Transmission electron microscopy	TEM
X-ray diffraction	XRD
Temperature programmed reduction	TPR
Temperature programmed desorption	TPD
Extended X-ray absorption fine structure	EXAFS
X-ray absorption fine structure	XAFS
Time-of-flight secondary ion mass spectrometry	ToF-SIMS
Nuclear magnetic resonance	NMR
Attenuated total reflection	ATR
Ultraviolet–visible spectroscopy	UV-Vis
Rate-determining step	RDS

Life-cycle assessment	LCA
2,2'-bipyridine 4,4'-dicarboxylic acid	bpydc

Acknowledgements

Financial support of KU Leuven through the C2 research program and Biorefineries Featuring Carbon Dioxide Capturing and Utilization Project, the National Key Projects for Fundamental Research and Development of China (2016YFA0202801), and National Natural Science Foundation of China (21690081) are acknowledged.

Conflict of Interest

The authors declare no conflict of interest.

References

1. Real-time and historical CO₂ levels were obtained from the website: <https://www.co2levels.org/#sources>).
2. *Earth's CO₂ Home Page*, <https://www.co2.earth/>.
3. IEA (2019), *SDG7: Data and Projections*, IEA, Paris <https://www.iea.org/reports/sdg7-data-and-projections>, 2019.
4. *World Energy Outlook; International Energy Agency: Paris, France, 2018*.
5. A. Kätelhön, R. Meys, S. Deutz, S. Suh and A. Bardow, *Proc. Natl. Acad. Sci. U.S.A.*, 2019, **116**, 11187-11194.
6. P. Markewitz, W. Kuckshinrichs, W. Leitner, J. Linssen, P. Zapp, R. Bongartz, A. Schreiber and T. E. Müller, *Energy Environ. Sci.*, 2012, **5**, 7281-7305.
7. S. Wang, S. Yan, X. Ma and J. Gong, *Energy Environ. Sci.*, 2011, **4**, 3805-3819.
8. A. Al-Mamoori, A. Krishnamurthy, A. A. Rownaghi and F. Rezaei, *Energy Technol.*, 2017, **5**, 834-849.
9. G. Centi, E. A. Quadrelli and S. Perathoner, *Energy Environ. Sci.*, 2013, **6**, 1711-1731.
10. S. Perathoner and G. Centi, *ChemSusChem*, 2014, **7**, 1274-1282.
11. M. D. Burkart, N. Hazari, C. L. Tway and E. L. Zeitler, *ACS Catal.*, 2019, **9**, 7937-7956.
12. R.-P. Ye, J. Ding, W. Gong, M. D. Argyle, Q. Zhong, Y. Wang, C. K. Russell, Z. Xu, A. G. Russell, Q. Li, M. Fan and Y.-G. Yao, *Nat. Commun.*, 2019, **10**, 5698.
13. M. Aresta, A. Dibenedetto and A. Angelini, *Chem. Rev.*, 2014, **114**, 1709-1742.
14. B. Hu, C. Guild and S. L. Suib, *J. CO₂ Util.*, 2013, **1**, 18-27.
15. X. Jiang, X. Nie, X. Guo, C. Song and J. G. Chen, *Chem. Rev.*, 2020, **120**, 7984-8034.
16. Q. Liu, L. Wu, R. Jackstell and M. Beller, *Nat. Commun.*, 2015, **6**, 5933.
17. S. Enthaler, J. von Langermann and T. Schmidt, *Energy Environ. Sci.*, 2010, **3**, 1207-1217.
18. W. Supronowicz, I. A. Ignatyev, G. Lolli, A. Wolf, L. Zhao and L. Mleczko, *Green Chem.*, 2015, **17**, 2904-2911.

19. J. Eppinger and K.-W. Huang, *ACS Energy Lett.*, 2017, **2**, 188-195.
20. T. Lin, X. Qi, X. Wang, L. Xia, C. Wang, F. Yu, H. Wang, S. Li, L. Zhong and Y. Sun, *Angew. Chem., Int. Ed.*, 2019, **58**, 4627-4631.
21. D. Xu, Y. Wang, M. Ding, X. Hong, G. Liu and S. C. E. Tsang, *Chem*, 2020, DOI: <https://doi.org/10.1016/j.chempr.2020.10.019>.
22. K. Sun, Y. Wu, M. Tan, L. Wang, G. Yang, M. Zhang, W. Zhang and Y. Tan, *ChemCatChem*, 2019, **11**, 2695-2706.
23. M. Iguchi, Y. Himeda, Y. Manaka and H. Kawanami, *ChemSusChem*, 2016, **9**, 2749-2753.
24. H. Zhong, M. Iguchi, F.-Z. Song, M. Chatterjee, T. Ishizaka, I. Nagao, Q. Xu and H. Kawanami, *Sustain. Energy Fuels*, 2017, **1**, 1049-1055.
25. Z. Li and Q. Xu, *Acc. Chem. Res.*, 2017, **50**, 1449-1458.
26. K. Sordakis, C. Tang, L. K. Vogt, H. Junge, P. J. Dyson, M. Beller and G. Laurenczy, *Chem. Rev.*, 2018, **118**, 372-433.
27. X. Wang, Q. Meng, L. Gao, Z. Jin, J. Ge, C. Liu and W. Xing, *Int. J. Hydrog. Energy*, 2018, **43**, 7055-7071.
28. R. Kanega, M. Z. Ertem, N. Onishi, D. J. Szalda, E. Fujita and Y. Himeda, *Organometallics*, 2020, **39**, 1519-1531.
29. Y. Ahn, J. Byun, D. Kim, B.-S. Kim, C.-S. Lee and J. Han, *Green Chem.*, 2019, **21**, 3442-3455.
30. N. von der Assen, J. Jung and A. Bardow, *Energy Environ. Sci.*, 2013, **6**, 2721-2734.
31. J. Artz, T. E. Müller, K. Thenert, J. Kleinekorte, R. Meys, A. Sternberg, A. Bardow and W. Leitner, *Chem. Rev.*, 2018, **118**, 434-504.
32. N. Z. Muradov and T. N. Veziroğlu, *Int. J. Hydrog. Energy*, 2008, **33**, 6804-6839.
33. W.-H. Wang, Y. Himeda, J. T. Muckerman, G. F. Manbeck and E. Fujita, *Chem. Rev.*, 2015, **115**, 12936-12973.
34. J. Klankermayer, S. Wesselbaum, K. Beydoun and W. Leitner, *Angew. Chem., Int. Ed.*, 2016, **55**, 7296-7343.
35. A. Álvarez, A. Bansode, A. Urakawa, A. V. Bavykina, T. A. Wezendonk, M. Makkee, J. Gascon and F. Kapteijn, *Chem. Rev.*, 2017, **117**, 9804-9838.
36. D. Mellmann, P. Sponholz, H. Junge and M. Beller, *Chem. Soc. Rev.*, 2016, **45**, 3954-3988.
37. K. Dong, R. Razaq, Y. Hu and K. Ding, *Top. Curr. Chem.*, 2017, **375**, 23.
38. C. Ziebart, C. Federsel, P. Anbarasan, R. Jackstell, W. Baumann, A. Spannenberg and M. Beller, *J. Am. Chem. Soc.*, 2012, **134**, 20701-20704.
39. C. Federsel, C. Ziebart, R. Jackstell, W. Baumann and M. Beller, *Chem. Eur. J.*, 2012, **18**, 72-75.
40. G. A. Filonenko, R. van Putten, E. N. Schulpen, E. J. M. Hensen and E. A. Pidko, *ChemCatChem*, 2014, **6**, 1526-1530.
41. R. Tanaka, M. Yamashita and K. Nozaki, *J. Am. Chem. Soc.*, 2009, **131**, 14168-14169.
42. R. Tanaka, M. Yamashita, L. W. Chung, K. Morokuma and K. Nozaki, *Organometallics*, 2011, **30**, 6742-6750.
43. N. Yan and K. Philippot, *Curr. Opin. Chem. Eng.*, 2018, **20**, 86-92.
44. D. A. Bulushev and J. R. H. Ross, *Catal. Rev.*, 2018, **60**, 566-593.
45. K. Zhou and Y. Li, *Angew. Chem., Int. Ed.*, 2012, **51**, 602-613.
46. L. Zhang, M. Zhou, A. Wang and T. Zhang, *Chem. Rev.*, 2020, **120**, 683-733.
47. B. Qiao, A. Wang, X. Yang, L. F. Allard, Z. Jiang, Y. Cui, J. Liu, J. Li and T. Zhang, *Nat. Chem.*, 2011, **3**, 634-641.
48. X.-F. Yang, A. Wang, B. Qiao, J. Li, J. Liu and T. Zhang, *Acc. Chem. Res.*, 2013, **46**, 1740-1748.
49. L. Zhang, Y. Ren, W. Liu, A. Wang and T. Zhang, *Natl. Sci. Rev.*, 2018, **5**, 653-672.
50. X. Su, X.-F. Yang, Y. Huang, B. Liu and T. Zhang, *Acc. Chem. Res.*, 2019, **52**, 656-664.
51. C. Ling, Q. Li, A. Du and J. Wang, *ACS Appl. Mater. Interfaces*, 2018, **10**, 36866-36872.

52. Y. Guo, S. Mei, K. Yuan, D.-J. Wang, H.-C. Liu, C.-H. Yan and Y.-W. Zhang, *ACS Catal.*, 2018, **8**, 6203-6215.
53. M.-M. Millet, G. Algara-Siller, S. Wrabetz, A. Mazheika, F. Girgsdies, D. Teschner, F. Seitz, A. Tarasov, S. V. Levchenko, R. Schlögl and E. Frei, *J. Am. Chem. Soc.*, 2019, **141**, 2451-2461.
54. Y. Cheng, S. Yang, S. P. Jiang and S. Wang, *Small Methods*, 2019, **3**, 1800440.
55. O. S. Bushuyev, P. De Luna, C. T. Dinh, L. Tao, G. Saur, J. van de Lagemaat, S. O. Kelley and E. H. Sargent, *Joule*, 2018, **2**, 825-832.
56. Z. Sun, T. Ma, H. Tao, Q. Fan and B. Han, *Chem*, 2017, **3**, 560-587.
57. L. Wang, W. Chen, D. Zhang, Y. Du, R. Amal, S. Qiao, J. Wu and Z. Yin, *Chem. Soc. Rev.*, 2019, **48**, 5310-5349.
58. Y. Zhao, G. I. N. Waterhouse, G. Chen, X. Xiong, L.-Z. Wu, C.-H. Tung and T. Zhang, *Chem. Soc. Rev.*, 2019, **48**, 1972-2010.
59. Y. Chen, S. Ji, C. Chen, Q. Peng, D. Wang and Y. Li, *Joule*, 2018, **2**, 1242-1264.
60. N. Han, P. Ding, L. He, Y. Li and Y. Li, *Adv. Energy Mater.*, 2020, **10**, 1902338.
61. T. Kong, Y. Jiang and Y. Xiong, *Chem. Soc. Rev.*, 2020, **49**, 6579-6591.
62. M. Li, H. Wang, W. Luo, P. C. Sherrell, J. Chen and J. Yang, *Adv. Mater.*, 2020, **32**, 2001848.
63. G. H. Gunasekar, K. Park, K.-D. Jung and S. Yoon, *Inorg. Chem. Front.*, 2016, **3**, 882-895.
64. T. Asefa, K. Koh and C. W. Yoon, *Adv. Energy Mater.*, 2019, **9**, 1901158.
65. A. Behr and K. Nowakowski, in *Adv. Inorg. Chem.*, eds. M. Aresta and R. van Eldik, Academic Press, 2014, vol. 66, pp. 223-258.
66. M. Pérez-Fortes, J. C. Schöneberger, A. Boulamanti, G. Harrison and E. Tzimas, *Int. J. Hydrog. Energy*, 2016, **41**, 16444-16462.
67. P. G. Jessop, T. Ikariya and R. Noyori, *Chem. Rev.*, 1995, **95**, 259-272.
68. P. G. Jessop, F. Joó and C.-C. Tai, *Coord. Chem. Rev.*, 2004, **248**, 2425-2442.
69. G. T. Rochelle, *Science*, 2009, **325**, 1652-1654.
70. X. E. Hu, Q. Yu, F. Barzagli, C. e. Li, M. Fan, K. A. M. Gasem, X. Zhang, E. Shiko, M. Tian, X. Luo, Z. Zeng, Y. Liu and R. Zhang, *ACS Sustain. Chem. Eng.*, 2020, **8**, 6173-6193.
71. X. Shao, J. Xu, Y. Huang, X. Su, H. Duan, X. Wang and T. Zhang, *AIChE J.*, 2016, **62**, 2410-2418.
72. Q. Liu, X. Yang, L. Li, S. Miao, Y. Li, Y. Li, X. Wang, Y. Huang and T. Zhang, *Nat. Commun.*, 2017, **8**, 1407.
73. G. Bredig and S. R. Carter, *Berichte der deutschen chemischen Gesellschaft*, 1914, **47**, 541-545.
74. M. W. Farlow and H. Adkins, *J. Am. Chem. Soc.*, 1935, **57**, 2222-2223.
75. E. González, C. Marchant, C. Sepúlveda, R. García, I. T. Ghampson, N. Escalona and J. L. García-Fierro, *Appl. Catal., B*, 2018, **224**, 368-375.
76. J. Su, L. Yang, M. Lu and H. Lin, *ChemSusChem*, 2015, **8**, 813-816.
77. C. E. Mitchell, U. Terranova, I. Alshibane, D. J. Morgan, T. E. Davies, Q. He, J. S. J. Hargreaves, M. Sankar and N. H. de Leeuw, *New J. Chem.*, 2019, **43**, 13985-13997.
78. C. Mondelli, B. Puértolas, M. Ackermann, Z. Chen and J. Pérez-Ramírez, *ChemSusChem*, 2018, **11**, 2859-2869.
79. J. H. Lee, J. Ryu, J. Y. Kim, S.-W. Nam, J. H. Han, T.-H. Lim, S. Gautam, K. H. Chae and C. W. Yoon, *J. Mater. Chem. A*, 2014, **2**, 9490-9495.
80. H. Park, J. H. Lee, E. H. Kim, K. Y. Kim, Y. H. Choi, D. H. Youn and J. S. Lee, *Chem. Commun.*, 2016, **52**, 14302-14305.
81. F. Goettmann, A. Thomas and M. Antonietti, *Angew. Chem., Int. Ed.*, 2007, **46**, 2717-2720.
82. Z. Huang, F. Li, B. Chen, T. Lu, Y. Yuan and G. Yuan, *Appl. Catal., B*, 2013, **136-137**, 269-277.
83. S. Samanta and R. Srivastava, *Sustain. Energy Fuels*, 2017, **1**, 1390-1404.
84. G. Vilé, D. Albani, M. Nachttegaal, Z. Chen, D. Dontsova, M. Antonietti, N. López and J. Pérez-Ramírez, *Angew. Chem., Int. Ed.*, 2015, **54**, 11265-11269.

85. F. Wang, J. Xu, X. Shao, X. Su, Y. Huang and T. Zhang, *ChemSusChem*, 2016, **9**, 246-251.
86. Y. Zhou, Y. Huang, B. Jin, X. Luo and Z. Liang, *Ind. Eng. Chem. Res.*, 2019, **58**, 44-52.
87. Y. Wu, Y. Zhao, H. Wang, B. Yu, X. Yu, H. Zhang and Z. Liu, *Ind. Eng. Chem. Res.*, 2019, **58**, 6333-6339.
88. H. Song, N. Zhang, C. Zhong, Z. Liu, M. Xiao and H. Gai, *New J. Chem.*, 2017, **41**, 9170-9177.
89. C. J. Stalder, S. Chao, D. P. Summers and M. S. Wrighton, *J. Am. Chem. Soc.*, 1983, **105**, 6318-6320.
90. Q.-Y. Bi, J.-D. Lin, Y.-M. Liu, X.-L. Du, J.-Q. Wang, H.-Y. He and Y. Cao, *Angew. Chem., Int. Ed.*, 2014, **53**, 13583-13587.
91. M. S. Shafeeyan, W. M. A. W. Daud, A. Houshmand and A. Shamiri, *J. Anal. Appl. Pyrolysis*, 2010, **89**, 143-151.
92. A. Cabiac, G. Delahay, R. Durand, P. Trens, B. Coq and D. Plée, *Carbon*, 2007, **45**, 3-10.
93. Z. Zhang, L. Zhang, M. J. Hülsey and N. Yan, *Mol. Catal.*, 2019, **475**, 110461.
94. Z. Zhang, L. Zhang, S. Yao, X. Song, W. Huang, M. J. Hülsey and N. Yan, *J. Catal.*, 2019, **376**, 57-67.
95. J. A. H. Dreyer, P. Li, L. Zhang, G. K. Beh, R. Zhang, P. H. L. Sit and W. Y. Teoh, *Appl. Catal., B*, 2017, **219**, 715-726.
96. S. Kattel, W. Yu, X. Yang, B. Yan, Y. Huang, W. Wan, P. Liu and J. G. Chen, *Angew. Chem., Int. Ed.*, 2016, **55**, 7968-7973.
97. J. Zhang, L. Fan, F. Zhao, Y. Fu, J.-Q. Lu, Z. Zhang, B. Teng and W. Huang, *ChemCatChem*, 2020, **12**, 5540-5547.
98. T. Umegaki, Y. Satomi and Y. Kojima, *J. Japan Pet. Inst. Energy*, 2017, **96**, 487-492.
99. L.-C. Lee, X. Xing and Y. Zhao, *ACS Appl. Mater. Interfaces*, 2017, **9**, 38436-38444.
100. C. Hao, S. Wang, M. Li, L. Kang and X. Ma, *Catal. Today*, 2011, **160**, 184-190.
101. N. Liu, R. J. Du and W. Li, *Adv. Mater. Res.*, 2013, **821-822**, 1330-1335.
102. K. Mori, T. Taga and H. Yamashita, *ACS Catal.*, 2017, **7**, 3147-3151.
103. M. S. Maru, S. Ram, R. S. Shukla and N.-u. H. Khan, *Mol. Catal.*, 2018, **446**, 23-30.
104. T. Umegaki, Y. Enomoto and Y. Kojima, *Catal. Sci. Technol.*, 2016, **6**, 409-412.
105. S. K. Kabra, E. Turpeinen, M. Huuhtanen, R. L. Keiski and G. D. Yadav, *Chem. Eng. J.*, 2016, **285**, 625-634.
106. A. Weilhard, M. I. Qadir, V. Sans and J. Dupont, *ACS Catal.*, 2018, **8**, 1628-1634.
107. J. Elek, L. Nádasdi, G. Papp, G. Laurenczy and F. Joó, *Appl. Catal., A*, 2003, **255**, 59-67.
108. G. A. Filonenko, E. J. M. Hensen and E. A. Pidko, *Catal. Sci. Technol.*, 2014, **4**, 3474-3485.
109. F. J. Fernández-Alvarez, M. Iglesias, L. A. Oro and V. Polo, *ChemCatChem*, 2013, **5**, 3481-3494.
110. W. Zhang, S. Wang, Y. Zhao and X. Ma, *Chem. Lett.*, 2016, **45**, 555-557.
111. W. Zhang, S. Wang, Y. Zhao and X. Ma, *Fuel Process. Technol.*, 2018, **178**, 98-103.
112. P. Munshi, A. D. Main, J. C. Linehan, C.-C. Tai and P. G. Jessop, *J. Am. Chem. Soc.*, 2002, **124**, 7963-7971.
113. J. C. Tsai and K. M. Nicholas, *J. Am. Chem. Soc.*, 1992, **114**, 5117-5124.
114. G. C. Bond, P. A. Sermon, G. Webb, D. A. Buchanan and P. B. Wells, *J. Chem. Soc., Chem. Commun.*, 1973, DOI: 10.1039/C3973000444B, 444b-445.
115. M. Sankar, Q. He, R. V. Engel, M. A. Sainna, A. J. Logsdail, A. Roldan, D. J. Willock, N. Agarwal, C. J. Kiely and G. J. Hutchings, *Chem. Rev.*, 2020, **120**, 3890-3938.
116. D. Preti, C. Resta, S. Squarcialupi and G. Fachinetti, *Angew. Chem., Int. Ed.*, 2011, **50**, 12551-12554.
117. G. A. Filonenko, W. L. Vrijburg, E. J. M. Hensen and E. A. Pidko, *J. Catal.*, 2016, **343**, 97-105.
118. C. Wu, Z. Zhang, Q. Zhu, H. Han, Y. Yang and B. Han, *Green Chem.*, 2015, **17**, 1467-1472.
119. Q. Liu, X. Wang, Y. Ren, X. Yang, Z. Wu, X. Liu, L. Li, S. Miao, Y. Su, Y. Li, C. Liang and Y. Huang, *Chin. J. Chem.*, 2018, **36**, 329-332.
120. D. Yang, W. Pei, S. Zhou, J. Zhao, W. Ding and Y. Zhu, *Angew. Chem., Int. Ed.*, 2020, **59**, 1919-1924.

121. M. Sankar, N. Dimitratos, P. J. Miedziak, P. P. Wells, C. J. Kiely and G. J. Hutchings, *Chem. Soc. Rev.*, 2012, **41**, 8099-8139.
122. K. Mori, T. Sano, H. Kobayashi and H. Yamashita, *J. Am. Chem. Soc.*, 2018, **140**, 8902-8909.
123. M. Wen, K. Mori, Y. Futamura, Y. Kuwahara, M. Navlani-García, T. An and H. Yamashita, *Sci. Rep.*, 2019, **9**, 15675.
124. Y. Kuwahara, Y. Fujie, T. Mihogi and H. Yamashita, *ACS Catal.*, 2020, **10**, 6356-6366.
125. S. Masuda, K. Mori, Y. Futamura and H. Yamashita, *ACS Catal.*, 2018, **8**, 2277-2285.
126. S. Masuda, K. Mori, Y. Kuwahara and H. Yamashita, *J. Mater. Chem. A*, 2019, **7**, 16356-16363.
127. K. Mori, S. Masuda, H. Tanaka, K. Yoshizawa, M. Che and H. Yamashita, *Chem. Commun.*, 2017, **53**, 4677-4680.
128. Q. Sun, X. Fu, R. Si, C.-H. Wang and N. Yan, *ChemCatChem*, 2019, **11**, 5093-5097.
129. L. T. M. Nguyen, H. Park, M. Banu, J. Y. Kim, D. H. Youn, G. Magesh, W. Y. Kim and J. S. Lee, *RSC Adv.*, 2015, **5**, 105560-105566.
130. Q. Sun, B. W. J. Chen, N. Wang, Q. He, A. Chang, C.-M. Yang, H. Asakura, T. Tanaka, M. J. Hülsey, C.-H. Wang, J. Yu and N. Yan, *Angew. Chem., Int. Ed.*, 2020, **59**, 20183-20191.
131. K. M. K. Yu, C. M. Y. Yeung and S. C. Tsang, *J. Am. Chem. Soc.*, 2007, **129**, 6360-6361.
132. M. I. Qadir, A. Weilhard, J. A. Fernandes, I. de Pedro, B. J. C. Vieira, J. C. Waerenborgh and J. Dupont, *ACS Catal.*, 2018, **8**, 1621-1627.
133. N. M. Simon, M. Zanatta, F. P. dos Santos, M. C. Corvo, E. J. Cabrita and J. Dupont, *ChemSusChem*, 2017, **10**, 4927-4933.
134. J. J. Corral-Pérez, A. Bansode, C. S. Praveen, A. Kokalj, H. Reymond, A. Comas-Vives, J. VandeVondele, C. Copéret, P. R. von Rohr and A. Urakawa, *J. Am. Chem. Soc.*, 2018, **140**, 13884-13891.
135. F. Cozzi, *Adv. Synth. Catal.*, 2006, **348**, 1367-1390.
136. C. Copéret, M. Chabanas, R. Petroff Saint-Arroman and J.-M. Basset, *Angew. Chem., Int. Ed.*, 2003, **42**, 156-181.
137. C. Copéret, A. Comas-Vives, M. P. Conley, D. P. Estes, A. Fedorov, V. Mougel, H. Nagae, F. Núñez-Zarur and P. A. Zhizhko, *Chem. Rev.*, 2016, **116**, 323-421.
138. A. Wang, J. Li and T. Zhang, *Nat. Rev. Chem.*, 2018, **2**, 65-81.
139. S. Ding, M. J. Hülsey, J. Pérez-Ramírez and N. Yan, *Joule*, 2019, **3**, 2897-2929.
140. M. Monai, M. Melchionna and P. Fornasiero, in *Adv. Catal.*, ed. C. Song, Academic Press, 2018, vol. 63, pp. 1-73.
141. M. Rose, *ChemCatChem*, 2014, **6**, 1166-1182.
142. Q. Sun, Z. Dai, X. Meng, L. Wang and F.-S. Xiao, *ACS Catal.*, 2015, **5**, 4556-4567.
143. S. Kramer, N. R. Bennedsen and S. Kegnaes, *ACS Catal.*, 2018, **8**, 6961-6982.
144. P. Bhanja, A. Modak and A. Bhaumik, *ChemCatChem*, 2019, **11**, 244-257.
145. K. Huang, J.-Y. Zhang, F. Liu and S. Dai, *ACS Catal.*, 2018, **8**, 9079-9102.
146. A. Jens, *ChemCatChem*, 2018, **10**, 1753-1771.
147. K. Park, G. H. Gunasekar, N. Prakash, K.-D. Jung and S. Yoon, *ChemSusChem*, 2015, **8**, 3410-3413.
148. G. H. Gunasekar, J. Shin, K.-D. Jung, K. Park and S. Yoon, *ACS Catal.*, 2018, **8**, 4346-4353.
149. G. H. Gunasekar, K.-D. Jung and S. Yoon, *Inorg. Chem.*, 2019, **58**, 3717-3723.
150. K. Park, G. H. Gunasekar, S.-H. Kim, H. Park, S. Kim, K. Park, K.-D. Jung and S. Yoon, *Green Chem.*, 2020, **22**, 1639-1649.
151. J. J. Corral-Pérez, A. Billings, D. Stoian and A. Urakawa, *ChemCatChem*, 2019, **11**, 4725-4730.
152. N. Onishi, R. Kanega, E. Fujita and Y. Himeda, *Adv. Synth. Catal.*, 2019, **361**, 289-296.
153. G. H. Gunasekar, K. Park, V. Ganesan, K. Lee, N.-K. Kim, K.-D. Jung and S. Yoon, *Chem. Mater.*, 2017, **29**, 6740-6748.

154. G. Gunniya Hariyanandam, D. Hyun, P. Natarajan, K.-D. Jung and S. Yoon, *Catal. Today*, 2016, **265**, 52-55.
155. A. Jaleel, S.-H. Kim, P. Natarajan, G. H. Gunasekar, K. Park, S. Yoon and K.-D. Jung, *J. CO2 Util.*, 2020, **35**, 245-255.
156. G. H. Gunasekar and S. Yoon, *J. Mater. Chem. A*, 2019, **7**, 14019-14026.
157. Z.-Z. Yang, H. Zhang, B. Yu, Y. Zhao, G. Ji and Z. Liu, *Chem. Commun.*, 2015, **51**, 1271-1274.
158. G. M. Eder, D. A. Pyles, E. R. Wolfson and P. L. McGrier, *Chem. Commun.*, 2019, **55**, 7195-7198.
159. X. Shao, X. Yang, J. Xu, S. Liu, S. Miao, X. Liu, X. Su, H. Duan, Y. Huang and T. Zhang, *Chem*, 2019, **5**, 693-705.
160. B. Chen, M. Dong, S. Liu, Z. Xie, J. Yang, S. Li, Y. Wang, J. Du, H. Liu and B. Han, *ACS Catal.*, 2020, **10**, 8557-8566.
161. A. Kann, H. Hartmann, A. Besmehn, P. J. C. Hausoul and R. Palkovits, *ChemSusChem*, 2018, **11**, 1857-1865.
162. R. Sun, A. Kann, H. Hartmann, A. Besmehn, P. J. C. Hausoul and R. Palkovits, *ChemSusChem*, 2019, **12**, 3278-3285.
163. N. D. McNamara and J. C. Hicks, *ChemSusChem*, 2014, **7**, 1114-1124.
164. Z. Xu, N. D. McNamara, G. T. Neumann, W. F. Schneider and J. C. Hicks, *ChemCatChem*, 2013, **5**, 1769-1771.
165. H.-K. Lo, I. Thiel and C. Copéret, *Chem. Eur. J.*, 2019, **25**, 9443-9446.
166. H.-K. Lo and C. Copéret, *ChemCatChem*, 2019, **11**, 430-434.
167. Y. Kuwahara, Y. Fujie and H. Yamashita, *ChemCatChem*, 2017, **9**, 1906-1914.
168. Z. Lei, Y. Xue, W. Chen, W. Qiu, Y. Zhang, S. Horike and L. Tang, *Adv. Energy Mater.*, 2018, **8**, 1801587.
169. L. Jiao and H.-L. Jiang, *Chem*, 2019, **5**, 786-804.
170. Y. Shi, S. Hou, X. Qiu and B. Zhao, *Top. Curr. Chem.*, 2020, **378**, 11.
171. J. W. Maina, C. Pozo-Gonzalo, L. Kong, J. Schütz, M. Hill and L. F. Dumée, *Mater. Horiz.*, 2017, **4**, 345-361.
172. B. An, L. Zeng, M. Jia, Z. Li, Z. Lin, Y. Song, Y. Zhou, J. Cheng, C. Wang and W. Lin, *J. Am. Chem. Soc.*, 2017, **139**, 17747-17750.
173. Y. Himeda, N. Onozawa-Komatsuzaki, H. Sugihara and K. Kasuga, *Organometallics*, 2007, **26**, 702-712.
174. S. Wang, S. Hou, C. Wu, Y. Zhao and X. Ma, *Chin. Chem. Lett.*, 2019, **30**, 398-402.
175. C. Wu, F. Irshad, M. Luo, Y. Zhao, X. Ma and S. Wang, *ChemCatChem*, 2019, **11**, 1256-1263.
176. P. Tshuma, B. C. E. Makhubela, N. Bingwa and G. Mehlana, *Inorg. Chem.*, 2020, **59**, 6717-6728.
177. Z. Li, T. M. Rayder, L. Luo, J. A. Byers and C.-K. Tsung, *J. Am. Chem. Soc.*, 2018, **140**, 8082-8085.
178. A. Urakawa, F. Jutz, G. Laurenczy and A. Baiker, *Chem. Eur. J.*, 2007, **13**, 3886-3899.
179. X. Lv, G. Lu, Z.-Q. Wang, Z.-N. Xu and G.-C. Guo, *ACS Catal.*, 2017, **7**, 4519-4526.
180. N. Yodsin, C. Rungnim, S. Tungkamani, V. Promarak, S. Namuangruk and S. Jungsuttiwong, *J. Phys. Chem. C*, 2020, **124**, 1941-1949.
181. O. Eisenstein and R. H. Crabtree, *New J. Chem.*, 2013, **37**, 21-27.
182. D. W. Stephan and G. Erker, *Angew. Chem., Int. Ed.*, 2010, **49**, 46-76.
183. D. W. Stephan, *Chem*, 2020, **6**, 1520-1526.
184. E. S. Wiedner, M. B. Chambers, C. L. Pitman, R. M. Bullock, A. J. M. Miller and A. M. Appel, *Chem. Rev.*, 2016, **116**, 8655-8692.
185. F. Joó, F. Joó, L. Nádásdi, J. Elek, G. Laurenczy and L. Nádásdi, *Chem. Commun.*, 1999, DOI: 10.1039/A902368B, 971-972.
186. J. Su, M. Lu and H. Lin, *Green Chem.*, 2015, **17**, 2769-2773.
187. S. Kar, A. Goepfert and G. K. S. Prakash, *Acc. Chem. Res.*, 2019, **52**, 2892-2903.

188. M. Cokoja, C. Bruckmeier, B. Rieger, W. A. Herrmann and F. E. Kühn, *Angew. Chem., Int. Ed.*, 2011, **50**, 8510-8537.
189. W. Wang, S. Wang, X. Ma and J. Gong, *Chem. Soc. Rev.*, 2011, **40**, 3703-3727.
190. Q. Lu and F. Jiao, *Nano Energy*, 2016, **29**, 439-456.
191. H. Shang, T. Wang, J. Pei, Z. Jiang, D. Zhou, Y. Wang, H. Li, J. Dong, Z. Zhuang, W. Chen, D. Wang, J. Zhang and Y. Li, *Angew. Chem., Int. Ed.*, 2020, **59**, 22465-22469.
192. Z. Jiang, T. Wang, J. Pei, H. Shang, D. Zhou, H. Li, J. Dong, Y. Wang, R. Cao, Z. Zhuang, W. Chen, D. Wang, J. Zhang and Y. Li, *Energy Environ. Sci.*, 2020, **13**, 2856-2863.
193. J. T. Feaster, C. Shi, E. R. Cave, T. Hatsukade, D. N. Abram, K. P. Kuhl, C. Hahn, J. K. Nørskov and T. F. Jaramillo, *ACS Catal.*, 2017, **7**, 4822-4827.
194. K. Liu, J. Wang, M. Shi, J. Yan and Q. Jiang, *Adv. Energy Mater.*, 2019, **9**, 1900276.
195. S. Zhang, P. Kang and T. J. Meyer, *J. Am. Chem. Soc.*, 2014, **136**, 1734-1737.
196. P. J. C. Hausoul, C. Broicher, R. Vegliante, C. Göb and R. Palkovits, *Angew. Chem., Int. Ed.*, 2016, **55**, 5597-5601.
197. P. R. Upadhyay and V. Srivastava, *RSC Adv.*, 2016, **6**, 42297-42306.



Ruiyan Sun

Sun Ruiyan, received his PhD in chemical engineering under the supervision of Prof. Tao Zhang from Dalian Institute of Chemical Physics, Chinese Academy of Sciences (CAS) in 2016 in the field of catalytic valorization of cellulose to polyols. From 2016 to 2019, he performed the postdoctoral research at RWTH Aachen with Prof. Regina Palkovits on the development of bifunctional catalysts for the catalytic upgrading of methanol to clean synthetic-fuels. Since November 2019, he moved to the group of Prof. Bert Sels as a postdoctoral researcher at KU Leuven engaging in developing new materials and routes for heterogeneous reduction of CO₂.



Yuhe Liao

Yuhe Liao currently is a professor at Guangzhou Institute of Energy Conversion (GIEC), Chinese Academy of Sciences. He received his PhD in Bioscience Engineering at KU Leuven in 2018 under the guidance of Prof. Bert F. Sels and Dr. Danny Verboekend in the field of heterogeneous catalysis for biomass conversion. Afterwards, he did post-doctoral work (2018–2020) at the same university on the topic of CO₂ capture and utilization. His current research focuses on heterogeneous catalysis and sustainable chemistry, including biomass conversion, CO₂ and solid waste valorisation.



Shao-Tao Bai

Shao-Tao Bai obtained his BSc in pharmacy and MSc in chemical biology in 2013 and 2015 at Peking University. Afterwards, he pursued PhD study at University of Amsterdam with prof. Joost Reek in supramolecular transition metal catalysis. After obtaining PhD in 2019, he moved to heterogeneous catalysis as a postdoctoral researcher with prof. Bert Sels at KU Leuven. His research interests across multidisciplinary fields of materials science, (bio-inspired) homo- & heterogeneous catalysis, supramolecular chemistry, spectroscopy, bio-renewable chemicals, computational catalysis, CO₂ capture and utilization, CH functionalization, kinetics, and electro- and photo-chemistry



Mingyuan Zheng

Mingyuan Zheng currently is a full professor at Dalian Institute of Chemical Physics, Chinese Academy of Sciences, where he got his PhD in physical chemistry in 2006 under the supervision of Prof. Tao Zhang. His research interests include catalytic conversion of biomass to high value chemicals, renewable chemistry and the industrial applications.



Cheng Zhou

Cheng Zhou received his BSc degree from the South China University of technology in 2016. He made his master thesis on hydrogenation of CO and CO₂ in Prof. Ye Wang's group at Xiamen University in 2019. Now he is pursuing his PhD in KU Leuven under the guidance of Prof. Bert Sels focusing on CO₂ capture and utilization.



Tao Zhang

Tao Zhang, currently the vice president of CAS, received his PhD in physical chemistry from DICP in 1989 under the supervision of Prof. Liwu Lin. After graduation, he worked as a postdoc with Prof. Frank Berry at Birmingham University for one year. He founded his own group at DICP in 1995. He was appointed an associate professor in 1993 and then promoted to a full professor in 1995. He was the director of DICP from 2007 to 2017 and was selected as an Academician by the CAS in 2013. His main research interests include single atom catalysis and biomass conversion.



Bert F. Sels

Bert F. Sels, currently Full Professor at KU Leuven (Belgium), obtained his PhD in 2000 in the field of heterogeneous oxidation catalysis. He was awarded the DSM Chemistry Award in 2000, the Incentive Award by the Belgian Chemical Society in 2005, and the Green Chemistry Award in 2015. He is currently director of the Centre for Surface Chemistry and Catalysis, designing heterogeneous solid catalysts for future challenges in industrial organic and environmental catalysis. His expertise includes heterogeneous catalysis in bio-refineries, design of hierarchical zeolites and carbons and the spectroscopic and kinetic study of active sites for small-molecule activation.